Spin pumping and inverse spin Hall effect in π-conjugated polymers

Dissertation

zur Erlangung des Doktorgrades der Naturwissenschaften
(Dr. rer. nat.)

der

Naturwissenschaftlichen Fakultät II
Chemie, Physik und Mathematik

der Martin-Luther-Universität
Halle-Wittenberg

vorgelegt von

Herrn Mohammad M. Qaid Mohammad

geb. am 30.05.1982 in Taiz, Jemen

Tag der Verteidigung
02.06.2020

Gutachter:
1. Prof. Dr. Georg Schmidt (Betreuer)
Martin-Luther-Universität - Halle
2. Prof. Dr. Georg Woltersdorf
Martin-Luther-Universität - Halle
3. Prof. Dr. Axel Hoffmann
Materials Science and Engineering - Illinois

*To my family and in
memory of my father*

Abstract

This thesis is devoted to studying the spin pumping and inverse spin Hall effect (ISHE) in π-conjugated polymers, PEDOT:PSS and PBTTT. Firstly, we investigate the damping in the ferromagnetic resonance (FMR) of Yttrium Iron Garnet (YIG) caused by spin pumping into adjacent conducting materials namely Pt and the conducting polymer PEDOT:PSS. By a systematic study which also includes multilayers in which the conducting layer is separated from the YIG by an insulator, we can show that a considerable part of the damping can be attributed to the so-called radiation damping which originates from the interaction of the magnetic fields caused by the precessing magnetization with the conducting layer. Especially when PEDOT:PSS is used as a spin sink, the observed damping must be completely attributed to radiation damping and no contribution from spin pumping can be identified. These results obtained in this part of the thesis demonstrate that Gilbert damping as a measure of spin pumping can only be used when careful control experiments accompany the investigation.

In the second part of the thesis, we present a systematic investigation for quantifying ISHE in the π-conjugated polymer PEDOT:PSS. Using several reference experiments, we can identify and isolate side effects which obscure the small but finite inverse spin-Hall effect in the polymer. We employ a sample geometry in which the contact areas and the area of spin current injection are laterally separated, which allows us to distinguish the ISHE from thermovoltages induced by nonreciprocal magnetostatic spin waves (MSSW) and from the ISHE induced by spin pumping through the polymer into the contacts. With an additional control experiment, we can even quantify the Nernst effect which also needs to be taken into account. With these results, we can unambiguously show that the ISHE is present in this material, albeit, at a level which requires a dedicated sample design and careful consideration of various artifacts.

By employing the protocols and procedures applied for investigating ISHE in PEDOT:PSS, we extend our study to include one of the most important polymers in organic electronics, the semiconducting polymer PBTTT. In a systematic study performed on several YIG/PBTTT bilayers, we present the first ever intensive study addressing the detection of ISHE in this polymer.

Furthermore, we expand the scope of our study to include a wide temperature range between RT 295 K and 5 K. We conduct an intensive study for the ISHE at different polymers thicknesses and different doping regimes.

On the other hand, at low-temperature, an ISHE-thickness dependence study is performed which gives us an insight into the spin relaxation mechanisms in PBTTT. Moreover, this study enables us to estimate some of the key parameters of the spin relaxation in this polymer namely spin diffusion length and spin relaxation time.

Contents

Contents

List of Abbreviations and Symbols

FMR	Ferromagnetic resonance
SOC	Spin-orbit coupling
πCP	$\pi-$conjugated polymer
GMR	Giant magnetoresistance
NM	Normal Metal
FM	Ferri/Ferromagnet
SHE	Spin-Hall effect
ISHE	Inverse spin-Hall effect
YIG	Yttrium-Iron-Garnet
MW	Microwave
rf	Radio frequency
h_{rf}	Rf field
LLG	Landau-Lifshitz-Gilbert
H_{ex}	External magnetic field
H_{eff}	Effective magnetic field
HWHM ΔH	Halfwidth at half maximum
ΔH_{p-p}	peak-to-peak linewidth
$4\pi M_{eff}$	Effective magnetization
$4\pi M_s$	Saturation magnetization
UM	Uniform mode
MPC	Magnon-phonon coupling
TMS	Two magnon scattering
DOS	Density of states
E_{exc}	Exchange energy
E_F	Fermi level
J_s	Spin current density
J_c	Charge current density
μ_m	Magnon chemical potential
μ_e	Electrochemical potential
δM	Magnetization decay
α	Magnetic damping
α_{in}	Intrinsic damping
λ_s -SDL	Spin diffusion length
τ_s	Spin-flip time , Spin relaxation time
τ_e	Relaxation time of electron momentum
AHE	Anomalous Hall effect
AC	ac current
DC	dc current
RMS	Root-mean-square
DMSO	Dimethyl sulphoxide
HOMO	Highest occupied molecular orbital
LUMO	Lowest unoccupied molecular orbital

MSSW	Magnetostatic surface spin waves
DEM	Damon-Eshbach modes
IP	In-plane
OOP	Out-of-plane
OC	Organic conductor
ΔH_0	Inhomogeneous broadening
Pt	Platinum
Ru	Ruthenium
WF	Work function
GGG	Gadolinium gallium garnet
σ_{IP}	In-plane conductivity
σ_{OOP}	Out-of-plane conductivity
LPE	Liquid phase epitaxy
D	Diffusion coefficient
Θ	Cone angle
IPA	Isopropyl alcohol
MIBK	Methyl isobutyl ketone
NEP	N-Ethylpyrrolidone
χ	Magnetic susceptibility
SS	Skew scattering
SJ	Side-jump scattering
IS	Intrinsic scattering
SHA θ_{SH}	Spin-Hall angle
$\boldsymbol{k}$	Wave vector
γ	Gyromagnetic ratio
EY	Elliott-Yafet
DP	D'yakonov–Perel
OFET	Organic Field-effect Transistors
α_{rad}	Radiation damping
α_{eddy}	Eddy current damping
α_{sh}	EM shielding damping
R_s	Spin resistance
P_{ab}	Absorbed power
$g^{\uparrow\downarrow}$	Intrinsic spin-mixing conductance
$g_{eff}^{\uparrow\downarrow}$	Effective spin-mixing conductance
n	Spin/Charge Carrier concentration
ISHV	Inverse spin-Hall voltage
ISHI	Inverse spin-Hall current
L_{hop}	Hopping length
ξ	Localization length

List of Figures

List of Tables

Chapter 1

1. Introduction

1.1. Motivation

Spintronics or spin electronics is a new branch of electronics based on purely quantum effects employing not only carrier charge transfer as conventional electronics, but also evoking carrier's spin transfer. Spintronics has triggered an enormous revolution in the recent technology especially in information storage since the revolutionary discovery of the Giant magnetoresistance (GMR) in 1988 [1, 2] which considerably changed our understanding of spin-dependent transport processes. For a few years, organics were ignored in spintronics until recently the spin valves using organic semiconductor were successfully made [3, 4].
Since then and attributing to many promising advantages of being flexible, cheap, easy to fabricate, and more importantly large spin lifetime, organics including small molecules and π-conjugated polymers - πCPs, have attracted much attention as spin transport materials. The considerable interest in these materials from the spintronics community had resulted in an emergence of the organic spintronics.

One of the main advantages that initially attracted much of the attention to organic materials is their expected longer spin diffusion length (SDL) due to the weak spin-orbit coupling (SOC). Because of that, organic materials are found to be promising for some spintronics devices, like spin valves where spin information can be potentially transferred over long distances.

However, these advantages of the large spin coherence and weak SOC have become drawbacks and challenges when using organics in other processes in spintronics especially those related to the generating and detecting spin currents namely, spin pumping, spin hall effect, and its inverse.

Spin pumping describes the flow of a spin current from a ferromagnet into an adjacent material (spin sink) due to spin precession [5–14] or due to thermal gradients in the ferromagnet [15–17].
In this process, the precession of magnetization in the ferromagnetic layer in ferromagnetic resonance (FMR) results in a non-equilibrium in the spin chemical potential (spin accumulation) which can diffuse into the nonmagnet. This spin accumulation has a time-independent component which is collinear to the external bias field of the FMR and a time-dependent precessing component which is perpendicular. If the spin accumulation created in the nonmagnet experiences sufficient spin flip, it does not flow back into the ferromagnetic material, and the out diffusion of the spin current reduces the spin accumulation and its time independence which is collinear to the external bias field of the FMR, can diffuse into the non-magnet. As a result, the FM is closer to equilibrium, a fact which becomes visible as an enhanced damping and an increased linewidth in FMR [5–14].

As a consequence of the spin pumping, the magnetic damping is enhanced due to the transfer of the angular momentum from the localized spins in the FM to the

conduction electrons or polarons in NM or πCP spin-sink, respectively. The increase of the damping is usually extracted from the FMR measurements performed at wide radio frequency (RF) range [12, 18, 19].

Investigating spin pumping into normal metals (NM) which have strong SOC has been done for years using plenty of NMs which are considered as perfect spin sinks with high spin pumping efficiency [5, 6, 9–14, 20, 21]. However, very limited studies on spin pumping into polymers were made due to the poor spin pumping efficiency comparing to the NMs [22, 23].

The most popular modus operandi of studying spin pumping in an FM/NM bilayer system is that the broadening of FMR linewidth measured for the FM/NM structure with respect to the bare FM, and hence the damping enhancement is an indication of the spin pumping from FM into NM. However, it was found that, the damping enhance in the bilayer systems has many origins depending on the type of the material (FM and NM), sample-waveguide coupling, sample geometry and measurement configurations. This means when studying the magnetic damping via FMR linewidth and damping enhance, all damping origins should be considered. This situation becomes very important for polymers because of the small spin pumping efficiency where in this case the damping enhance due to spin pumping becomes comparable to the damping emanating from the other damping origins rather than spin pumping.

The spin current flowing into spin sink material is detected as charge current in a process called inverse spin Hall effect (ISHE). The efficiency of the spin-charge conversion is governed by the SOC of the spin-sink material.

Several studies have been done for ISHE in NMs which is easily detected because of large SOC which results in large detected dc voltage which could amount to mV range [12, 20, 24–26]. On the other side, the weak SOC in polymers is the reason behind the very limited ISHE studies made there [22, 23, 27]. This weak SOC which results in a weak spin-flip rate and also the large thermoelectric response for many polymers (like PEDOT:PSS) bring many significant unforeseeable artifacts which interfere with the measured ISHE. For these reasons, measuring ISHE in polymers can only be done via systematic studies including many control experiments and careful measurements.

It is worth mentioning that, despite the many challenges emanating here, investigating spin pumping and ISHE in polymers is still very important in order to integrate these polymers in future spintronics devices especially for some πCPs which are widely used in many recent microelectronic devices, namely PEDOT:PSS and PBTTT.

Recently, PEDOT:PSS has made its entry in spintronics by showing indications of spin-charge conversion which was studied by measuring ISHE. However, only few studies shed light on that with contradicting results [23, 27, 28]. This contradiction comes from the inconsistency between considering the detected voltage either pure ISHE or pure thermovoltage. On the other side, all studies done on PBTTT observed no ISHE [23, 29, 30], despite observing spin pumping into it indicated by the FMR linewidth broadening [23].

The aim of this work is to establish a new platform for studying spin pumping and inverse spin Hall effect in π-conjugated polymers. In the spin pumping part, we

introduce a new origin of the magnetic damping enhance in FM/Spin-sink bilayers which has a significant contribution to the net magnetic damping during the spin pumping especially in FM/πCP bilayers. This is investigated using systematic studies within series of control experiments. Such systematic studies also are performed for investigating and detecting the pure ISHE in highly doped πCPs, PEDOT:PSS and for the first time the highly doped semiconducting polymer PBTTT. These studies are carried out following many strategies and careful measurements applied to quantify the ISHE and to isolate side effects which obscure the ISHE detected in the polymers.

1.2. The State of the Art

The most recent studies performed on the ISHE detection in PEDOT:PSS were done by Sun *et al.* [23, 31]. These studies were carried out by generating a very high spin current density employing pulsed-FMR (p-FMR) technique. A pulsed microwave power of 1kW, which is more than 4 orders of magnitude larger than the power used in our experiments, is used to induce a spin pumping from a conducting FM (Py) into heavily doped PEDOT:PSS. From these experiments, high ISHE-V and ISHE-I are detected which are amount to 17 μV and 69 nA, respectively. On the other hand, despite using such ultrahigh power, no ISHE was detected from the spin pumping into PBTTT.

An earlier study was done by Ando *et al.*, on YIG-PEDOT:PSS bilayer structure employing 40 mW continuous-wave microwave to induce spin pumping from thick YIG into the polymer [27]. Using a highly doped PEDOT:PSS similar to that used in our study, an ISHE signal of a half μV is measured.

Using the same YIG/PEDOT:PSS bilayer structure, and also the same power regime, Wang *et al.*, studied the SIHE in the highly doped PEDOT:PSS based on thick YIG [28]. In contrast to the previous studies, they showed that the measured dc voltage in the polymer during the FMR is completely governed by Seebeck effect in the polymer where the temperature gradient is created by the nonreciprocal magnetostatic surface spin wave (MSSW) propagation in YIG.

1.3. Thesis Outline

This thesis is organized as follows. Chapter 2 starts with the fundamentals necessary for understanding the results included in this work. To acquire a full recognition about the spin pumping and ISHE we start with the theoretical basics of the magnetization dynamics and ferromagnetic resonance and then end up with the theory of spin pumping and magnetic damping phenomenology. Besides that, this chapter explores in brief the spins and polarons in πCPs digging into the polarons origins and their main relaxation mechanisms. One of the main issues which is frequently mentioned throughout this work is the thermoelectric response in polymers and their influence on the ISHE measurements. To cover that, two major effects namely Seebeck effect and Nernst effect are presented in brief in this chapter. At the end of this chapter, we present a brief overview of the main materials under investigation

demonstrating their key properties and features relevant to the objectives of this work.

Chapter 3 contains a detailed description of the fabrication and characterization methods of the materials and devices used in this work. Besides that, it contains an overview of the setups and instruments employed in the FMR and ISHE measurements.

Chapter 4 is devoted to investigating the radiation damping in the FMR of YIG caused by spin pumping into the adjacent materials, Pt and the conducting polymer PEDOT:PSS. Throughout this chapter, the spin pumping and the so-called radiation damping are investigated in detail by performing many control experiments using plenty of samples structures.

Chapter 5 contains a systematic study for quantifying the pure ISHE in highly doped PEDOT:PSS. To achieve that, we present a systematic study employing several control experiments investigating many voltage origins associated with ISHE detection in YIG/PEDOT:PSS.

Chapter 6 is devoted to the spin-to-charge conversion study in semiconducting πCP PBTTT. This study was done applying the same systematic protocols established in chapter 5. However, investigating the spin-charge conversion in PBTTT is done in a much broader way not only detecting a pure ISHE but also investigating the ISHE and the spin relaxation mechanism in different doping regimes and a wide temperature range.

Finally in chapter 7, a summary of the thesis highlighting the important results and outcome of this work. It also includes some remarks or questions that can be considered for future work.

Chapter 2

2. Fundamentals and Theory

Virtually no area of spintronics today - especially when it comes to generating and detecting the spin current - is free from employing the spin pumping and inverse spin-Hall effect (ISHE). Usually, spin pumping and ISHE are concurrent with each other. The spin current injected into spin sink material is detected as a charge current via the ISHE mechanism. The purpose of this chapter is to present a theoretical background for the spin pumping and ISHE. This includes the basics and phenomenology of the general concepts in magnetism and spintronics which will be the ground for interpreting and understanding the results presented within this thesis. In addition to that, spins and polarons in π-conjugated polymers (πCPs) are discussed reviewing their main transport and relaxation mechanisms.

2.1. Magnetization Dynamics

2.1.1. Magnetic Moments and the Equation of Motion

For electrons orbiting an atom's nucleus, the relation between the magnetic moment $\boldsymbol{m}$ and the electronic angular momentum $\boldsymbol{\ell}$ is defined by [21, 32]

$$\boldsymbol{m} = \gamma \boldsymbol{\ell} \tag{2.1}$$

In this definition the parameter γ is called the gyromagnetic ratio and it has unis of $s^{-1}T^{-1}$, or $s^{-1}Oe^{-1}$. γ is defined in terms of Bohr magneton μ_B, Lande-factor (spectroscopic splitting g-factor) and the reduced Plank constant $\hbar$ as

$$\gamma = \frac{g\mu_B}{\hbar} \tag{2.2}$$

Here $\mu_B = e\hbar/2mc$ (in cgs units). e , m and , c are the elementary charge, electron rest mass, and the speed of light respectively. The electron's spin which is of pure quantum mechanical nature can be treated analogously to angular momentum. In this case, we will have spin angular momentum $\boldsymbol{\ell_s} = m_s\hbar\boldsymbol{e_z}$. m_s is the magnetic quantum number and it is related to the quantum number of electron spin s which has magnitude $s = 1/2$. $\boldsymbol{e_z}$ is the unit vector and its direction is parallel to the spin angular momentum.

The eigenvalues of the magnetic quantum number of the electron spin are $m_s = \pm\frac{1}{2}$. So in this situation we get

$$\boldsymbol{m} = \gamma \boldsymbol{\ell} = -\gamma m_s\hbar\boldsymbol{e_z} \tag{2.3}$$

The negative sign comes from the negative electron charge. Applying steady magnetic field H_0 on an atom results in an energy splitting known as Zeeman effect which is given by the Hamiltonian

$$\mathcal{H}_z = -\boldsymbol{m} \cdot \boldsymbol{H_0} = \gamma \hbar m_s H_0 \tag{2.4}$$

The corresponding energy eigenvalues ε_i are represented by a set of equally space energy levels $\Delta \varepsilon_i$ with the only transitions allowed $\Delta m_s = \pm 1$.

Accordingly, the energy level spacing is

$$\Delta \varepsilon_i = \gamma \hbar H_0 \tag{2.5}$$

The transitions of the magnetic dipole between the adjacent energy levels are expected for radiation of angular frequency ω_0 proportional to the energy $\Delta \varepsilon$ between these adjacent levels

$$\Delta \varepsilon = \hbar \omega_0 \tag{2.6}$$

Irradiating this system with microwave (MW) radio frequency field $\boldsymbol{H}_{rf} \perp \boldsymbol{H_0}$, a maximum rf absorption can be achieved at frequency $\omega_{rf} = \gamma H_0$. This latter is the resonance condition and it also is the principle behind electron paramagnetic resonance (EPR) and ferromagnetic resonance (FMR). These details of the Zeeman energy splitting and also MW power absorption inducing the resonance are shown in figure 2.1.
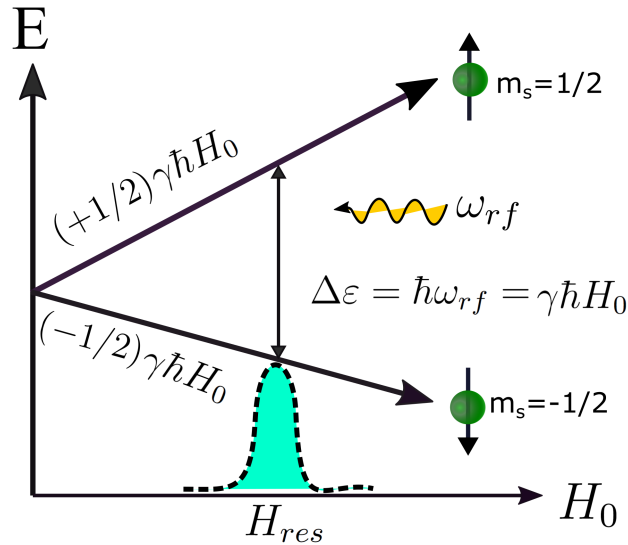
Figure 2.1 – Representation of Zeeman splitting energy which also illustrates the principle of FMR where the maximum power absorption occurs at $\Delta \varepsilon = \hbar \omega_{rf} = \gamma \hbar H_0$.

The effect of the steady magnetic field $\boldsymbol{H_0}$ on magnetic moment $\boldsymbol{m}$ results in a torque $\boldsymbol{T} = \boldsymbol{m} \times \boldsymbol{H_0}$. Since the torque itself is defined by the change of the angular momentum $\dfrac{d\boldsymbol{\ell}}{dt}$, then the equation of motion for the magnetic moment change under the influence of magnetic field in cgs units is

$$\frac{1}{\gamma} \frac{d\boldsymbol{m}}{dt} = -\boldsymbol{m} \times \boldsymbol{H_0} \tag{2.7}$$

2.1.2. Magnetization Precession

The magnetic field in Eq.2.4 represents the external Zeeman field. In principle, the total magnetic field acting on magnetic moments $\boldsymbol{m}$ is the effective magnetic field $\boldsymbol{H}_{eff}$ which summarizes all possible field origins interacting with $\boldsymbol{m}$ inside the magnetic material. $\boldsymbol{H}_{eff}$ can be written as [21]

$$\boldsymbol{H}_{eff} = \boldsymbol{H}_{xc} + \boldsymbol{H}_{ani} + \boldsymbol{H}_{stress} + \boldsymbol{H}_{dem} + \boldsymbol{H}_{ext} \tag{2.8}$$

where $\boldsymbol{H}_{xc}, \boldsymbol{H}_{ani}, \boldsymbol{H}_{stress}, \boldsymbol{H}_{dem}$ and $\boldsymbol{H}_{ext}$ are magnetic fields accounting for exchange interaction, magnetic and crystal field anisotropy, ferromagnet deformation, demagnetization effect, and external DC magnetic field, respectively.

In FM, the magnetization M can be defined as the magnetic moments m_i per unit cell volume [33],

$$M = \frac{\sum_{i=1}^{N} m_i}{dV} \tag{2.9}$$

This equation clarifies that the magnetization in the unit cell volume can be treated within a macroscopic spin. This assumption of magnetic moments per unit cell volume and magnetization is valid when we consider all magnetic moments m_i per unit cell are uniform adopting the finite element model [34]. Using Eq.2.8 and Eq.2.9 the equation of motion (Eq.2.7) in cgs units can be reformulated

$$\frac{1}{\gamma} \frac{d\boldsymbol{M}}{dt} = -\boldsymbol{M} \times \boldsymbol{H}_{eff} \tag{2.10}$$

According to this equation, with the torque $\boldsymbol{T}$ acting on $\boldsymbol{m}$ which corresponds to the rate of change of the angular momentum, the static magnetic field $\boldsymbol{H}_{eff}$ acting on the magnetization $\boldsymbol{M}$ results in precession of $\boldsymbol{M}$ around $\boldsymbol{H}_{eff}$ at constant cone angle Θ as shown in figure 2.2a. As shown by this equation, $\boldsymbol{M}$ precesses around $\boldsymbol{H}_{eff}$ without reaching the equilibrium position. The precession motion of the magnetization $\boldsymbol{M}$ that exposed to an effective magnetic field was first introduced by Landau and Lifshitz in 1935 [35]. However, in reality the magnetization in FM reaches equilibrium in a relaxation rate defined by the material properties. This situation is expressed by the magnetic damping and it is illustrated in figure 2.2b. This dissipation of precession motion occurring in real material systems and presented as magnetic *damping* was inserted as an extra term in the equation of motion, Eq.2.10 [36]. The new equation is usually referred to Landau-Lifshitz-Gilbert (LLG) equation which is given by (in cgs units):

$$\frac{d\boldsymbol{M}}{dt} = -\gamma \boldsymbol{M} \times \boldsymbol{H}_{eff} + \frac{\alpha}{M_s} \boldsymbol{M} \times \frac{d\boldsymbol{M}}{dt} \tag{2.11}$$

α is a dimensionless parameter referring to the relaxation process of the precession motion and known as Gilbert damping constant. M_s is the saturation magnetization of the magnetic material. The first term in RHS of Eq.2.11 refers to the precession motion part, while the second term refers to the damping part. Both cases, the undamped and the damped precession motion are clarified in Fig. 2.2 a and 2.2b
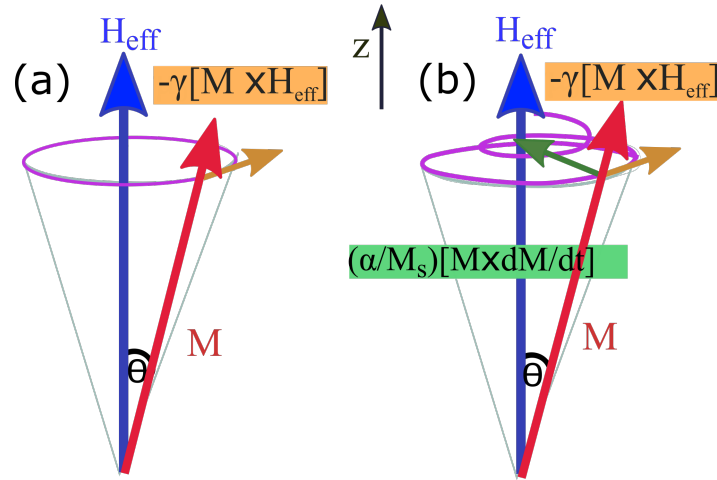
Figure 2.2 – Representation of magnetization precession under the effective magnetic field $\boldsymbol{H}_{eff}$. (a) The precession of the magnetization $\boldsymbol{M}$ driven by the torque acting on the magnetic moment indicated in Eq.2.10. (b) The effect of the damping on the magnetization precession motion which causes a spiral trajectory for the magnetization pushing it back to its equilibrium, Eq.2.11.

2.2. Magnetic Susceptibility and Ferromagnetic Resonance

2.2.1. Magnetic Susceptibility

Equation 2.11 describes the magnetization dynamics $\boldsymbol{M}$ and its response to the total effective magnetic field $\boldsymbol{H}_{eff}$. The total external magnetic field acting on the magnetic ultrathin films along thickness d in z-direction is given by [37, 38]:

$$\boldsymbol{H}^i_{eff} = -\frac{\partial}{\partial \boldsymbol{M}_i}\mathcal{F} \qquad (2.12)$$

where $i = x, y, z$ and $\mathcal{F}$ is magnetic free energy density. In FMR experiments, M is driven to the resonance by an external rf field h_{rf}. In this case $\boldsymbol{H}_{ext}$ in Eq.2.8 includes both the DC magnetic field $\boldsymbol{H}_{dc}$ and also the $\boldsymbol{h}_{rf}$ applied field.

$$\boldsymbol{H}_{ext} = \boldsymbol{H}_{dc} + \boldsymbol{h}_{rf} \qquad (2.13)$$

Consequently, in this case the magnetization M can be written as:

$$\boldsymbol{M} = \boldsymbol{M}_s + \boldsymbol{m}(t) \qquad (2.14)$$

where M_s is the static magnetization, and $m(t)$ is the dynamic magnetization which represents the rf component of M.

Using the time variation $exp(-i\omega t)$ suggested for the linearized Landau-Lifshitz equation for the magnetization $\boldsymbol{m}$ introduced by B. Henrich and co-workers [39, 40], the average of the rf magnetization components per unit area in the film ($\mathcal{M}_x$ and $\mathcal{M}_y$) [1], to an average rf driving field h_y represented by h_0 is simply given by the two following equations of motion [37],

---

[1]Here, FM surface is in x-y plane. $\mathcal{M}_x$ is defined by $\mathcal{M}_y$ and $\mathcal{M}_z$ because of the effective

$$-i\frac{\omega}{\gamma}\mathcal{M}_y + [\mathcal{B} - \frac{i\alpha\omega}{\gamma}]\mathcal{M}_z = 0 \tag{2.15}$$

$$[\mathcal{H} - \frac{i\alpha\omega}{\gamma}]\mathcal{M}_y + \frac{i\omega}{\gamma}\mathcal{M}_z = M_s dh_0 \tag{2.16}$$

where $\mathcal{B}$ is the effective magnetic flux density and it is expressed as

$$\mathcal{B} = H + 4\pi M_{eff} + \frac{K_1^{eff}}{2M_s}(3 + cos4\Theta) \tag{2.17}$$

$$\mathcal{H} = H + \frac{K_1^{eff}}{2M_s}cos4\Theta \tag{2.18}$$

$$4\pi M_{eff} = 4\pi D_z Ms - \frac{K_u^{eff}}{2M_s} \tag{2.19}$$

The factors K_1^{eff} and K_u^{eff} are related to the surface in-plane four-fold and uniaxial anisotropy of the film, respectively. D_z is the demagnetization factor and Θ defines the magnetization direction with respect to the applied magnetic field. The rf response signal during the FMR experiments is represented by the rf magnetic susceptibility χ, where

$$\chi = \chi' + i\chi'' \tag{2.20}$$

χ can be obtained by solving the equations 2.15 and 2.16 which yields:

$$\chi = \frac{\mathcal{M}_y}{h_0}\frac{M_s d[\mathcal{B} - \frac{i\alpha\omega}{\gamma}]}{[\mathcal{B} - \frac{i\alpha\omega}{\gamma}][\mathcal{H} - \frac{i\alpha\omega}{\gamma}] - (\frac{\omega}{\gamma})^2} \tag{2.21}$$

This equation contains two χ components, $Re(\chi)$ and $Im(\chi)$. These two components can be extracted as [38]

$$\chi' = \mathcal{A}[1 + \frac{H - H_{FMR}}{\Delta H^2 + (H - H_{FMR})^2}] \tag{2.22}$$

$$\chi'' = \mathcal{A}[\frac{\Delta H}{\Delta H^2 + (H - H_{FMR})^2}] \tag{2.23}$$

where $\mathcal{A} = f(\mathcal{B},\mathcal{H})$, Eq.2.17, and Eq.2.17. H in these equations represents the DC external magnetic field ($= H_{ext}$), H_{FMR} is the resonance field, and ΔH is the Halfwidth at half maximum (HWHM) of the Lorentzian absorption represented by χ''. ΔH is linked to the rf frequency by the magnetic damping α as

$$\Delta H = \alpha\frac{\omega}{\gamma} \tag{2.24}$$

---

components of the applied rf field. rf is applied along z-axis and its magnetic field component is directed along y-axis. Also, the rf component of M is m(z,t) [37] .

The spectrum of the susceptibility components χ' and χ'' are shown in Fig. 2.3a. This figure also shows the FMR parameters which can be extracted from χ'' spectrum namely, HWHM ΔH, H_{FMR} and also the power absorption P_{ab} which is represented by the resonance amplitude.

2.2.2. Ferromagnetic Resonance and Resonance Condition

Ferromagnetic Resonance (FMR) is the most popular technique used for studying rf absorption by the ferromagnet. This was first observed in 1946 by Griffiths [41] and also independently by Zavoisky [42]. It is clear from the previous section that, several FM parameters (e.g FMR amplitude, ΔH, α, etc), can be extracted from the susceptibility spectrum. In FMR spectrum, the FMR amplitude extracted from the χ'' curve represents the rf power absorbed by the magnetic film P_{ab} and it is expressed as [37, 43]

$$P_a = \frac{1}{2}Im(\chi)|h_0|^2 \qquad (2.25)$$

Where h_0 is the rf magnetic field components driving the magnetization which is perpendicular to the DC magnetic field H. As shown in this equation, $Im(\chi)$ reaches its maximum value when the absorbed power P_a is at its maximum which is exactly at the resonance H_{FMR}.

The FMR condition for the fully saturated sample can be obtained from Eq. 2.21 where the absorption $Im(\chi)$ maximizes and by setting the damping α to zero, then we get

$$(\frac{\omega}{\gamma})^2 = \mathcal{H}\mathcal{B} \qquad (2.26)$$

$$(\frac{\omega}{\gamma})^2 = [H_{FMR} + 4\pi M_{eff} + \frac{K_1^{eff}}{2M_s}(3 + cos4\Theta)] \times [H_{FMR} + \frac{K_1^{eff}}{2M_s}cos4\Theta] \qquad (2.27)$$

Studying shape effect in FMR in a specimen of a cubic ferromagnetic insulator in x-z plane (Fig. 2.3b) with demagnetization factors N_x, N_y, N_z, at small precession cone angle the frequency of the uniform mode is given by [44]

$$(\frac{\omega}{\gamma})^2 = [H_z + (N_y - N_z)M_z] \times [H_z + (N_x - N_z)M_z] \qquad (2.28)$$

N_x, N_y, N_z are the demagnetization factors along x,y,z directions. In $x - z$ plane, $N_x = N_z = 0$ and $N_y = 4\pi$. Considering $H_z \equiv H_{FMR}$, Eq. 2.28 becomes,

$$(\frac{\omega}{\gamma})^2 = H_{FMR}[H_{FMR} + 4\pi M_{eff}] \qquad (2.29)$$

Which is the Kittel formula for the resonance condition in the in-plane geometry. This equation is similar to the equation 2.27 when K_1^{eff} is very small [45]. In the case of out-of-plane geometry where H is perpendicular to the x-z plane, $N_x = N_y = 0$ and $N_z = 4\pi$, and hence we get

$$(\frac{\omega}{\gamma}) = [H_{FMR} - 4\pi M_s] \qquad (2.30)$$

Which is the Kittel formula for the resonance condition in the out-of-plane ge-

ometry. These two cases represent the frequency of the uniform mode (UM) where the wave vector ($\boldsymbol{k} = 0$), in distinction to the magnons and the other nonuniform precession modes [44].
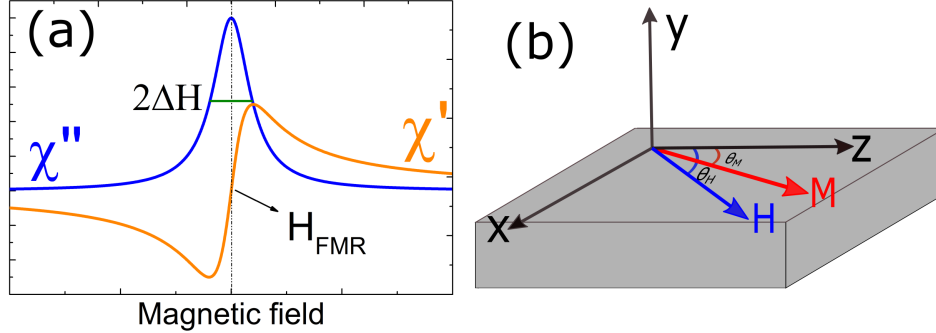
Figure 2.3 – (a) The spectrum of the two susceptibility components χ' , χ'' illustrating both ΔH and H_{FMR}. It shows the amplitude of χ'' curve which is used to calculate the P_{ab} as depicted in Eq. 2.25. (b) Representation of the in-plane geometry indicating the orientation of H and M vectors along the $x - z$ plane of the sample. The angles Θ_H and Θ_m are also shown here which define the directions of H and M, with respect to z direction, respectively.

In FMR experiments, driving magnetic film to the resonance is achieved by applying H_{ext}, Eq.2.13. In this case, the maximum absorption associated to the resonance is obtained using one of the two following methods. One method is by fixing the applied H_{dc} and sweeping the f_{rf} until it coincides with the magnetization eigenfrequency f_0 and at this point the MW absorption has its maximum value. The second possibility is to change the magnetization eigenfrequency f_0 which is done by sweeping H_{dc} at fixed rf frequency and the resonance occurs at $H_{ext} = H_{FMR}$ where $f_{rf} = f_0$ [21]. At the maximum absorption one can extract the linewidth ΔH and the rf absorption amplitude P_a as mentioned in the previous section.

2.3. Phenomenology and Origins of Magnetic Damping

The relaxation of magnetization in ferri/ferromagnetic materials manifests itself in the form of damping which often is measured from the FMR absorption linewidth ΔH as discussed in the previous section (Eq.2.24). FM system can be well described by its magnetization behavior in terms of the magnetization precession and the spins coupling by exchange or dipolar interactions [46]. The damping parameter which appears in the LLG equation, Eq. 2.11, describes the spiral motion of the magnetization M and can be considered as characteristic parameter for FM material. Magnetization relaxation, characterized by the magnetic damping constant α, has two origins, intrinsic α_{in} and extrinsic α_{ex}. The intrinsic spin damping involves three major mechanisms: magnon-phonon coupling (MPC), eddy current, and itinerant electron relaxation. The latter originates from the interaction of s-p like electrons in ultrathin film FM materials. Because this study will focus on ferrimagnetic insulator YIG, this type of damping is not relevant here.

Eddy current damping α_{eddy} is a result of the magnetic precession inducing current in FM conductors [47–49]. This case is illustrated in figure 2.4.
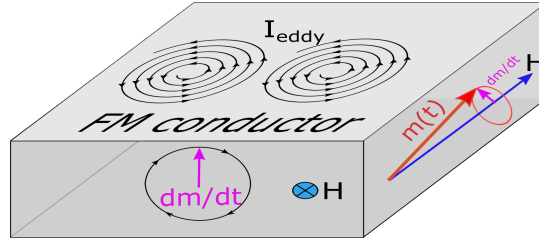
Figure 2.4 – A schematic of FM thinfilm showing the eddy current damping α_{eddy} generated by the eddy current I_{eddy} flowing in a closed loops induced in the conducting FM.

This new damping generated here α_{eddy} contributes to the net damping in LLG equation and this contribution can be evaluated by integrating Maxwell's equation across the film thickness d_F [50, 51]. α_{eddy} for the FMR mode (uniform mode, $k = 0$) is calculated in terms of M_s, the thin film conductivity σ, and the film thickness d_F as [47–50],

$$\alpha_{eddy} = \frac{1}{16} M_s \gamma (\frac{4\pi}{c}) \sigma d_F^2 \tag{2.31}$$

α_{eddy} can be significant in FM conductors and it strongly depends on FM conductivity. Interestingly, this effect is found to be significant not only in bare conducting FM films but also conducting or insulating FM when capped with conducting spin sink material. In this FM/Spin-sink structure, eddy current produces either a distortion of the FMR lineshape with no influence on the ΔH [49] or additional damping induced by the inhomogeneous precession in FM insulator producing an eddy current in the capping layer [8]. This latter adds small and finite damping which can be detected when using low-damping FM spin injector like epitaxial YIG, demonstrated in chapter 4.

The second process of the intrinsic damping is caused by magnon-phonon coupling (MPC) α_{Ph}[52]. MPC describes the uniform mode (UM) degradation by the direct energy transfer from the UM to the lattice motions (phonon) or energy transfer into the non-uniform modes and then decays into the lattice [53]. Both relaxation processes are illustrated in figure 2.5. The magnetic damping parameter due to MPC mechanism can be described by [52, 53]

$$\alpha_{Ph} = \frac{2\eta\gamma}{M_s} \Big(\frac{B_m(1+\nu)}{\mathcal{E}}\Big)^2 \tag{2.32}$$

Where η, B_m, ν, M_s and $\mathcal{E}$ are the phonon viscosity, the magneto-elastic shear constant, the Poisson ratio, saturation magnetization, and the Young modulus, respectively. The intrinsic part of the damping is extracted from the $\omega_{rf} - \Delta H$ linear dependence shown in Eq. 2.24.

On the other hand, extrinsic damping originates from two-magnon scattering (TMS) where the uniform mode decay is due to coupling with other spin waves (magnons). This is caused by the material defects and thus it is proportional to the

magnetic inhomogeneity.

Despite the link of the magnetic inhomogeneity to TMS, the inhomogeneous broadening ΔH_0, however, is mainly attributed to the distribution of magnetic properties (such as saturation magnetization and/or effective magnetic fields) which results in distribution of resonance frequencies and therefore additional line broadening [52, 54]. As a result, the $\omega_{rf} - \Delta H$ dependence will have the form,

$$\Delta H = \alpha \frac{\omega}{\gamma} + \Delta H_0 \tag{2.33}$$

In FMR experiments, this linewidth-frequency dependence is employed to extract the magnetic damping.
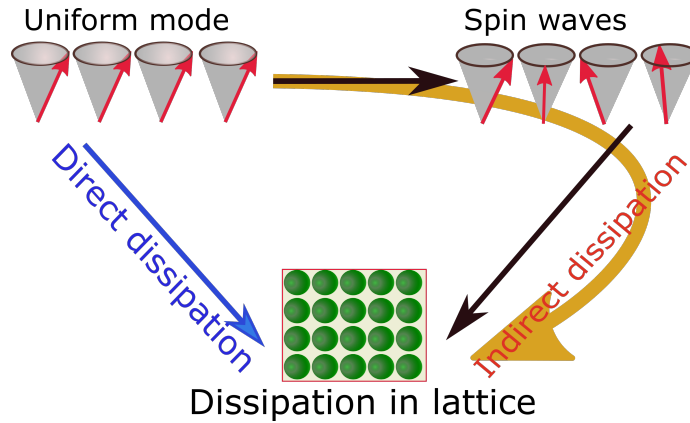
Figure 2.5 – An illustration of the two dissipation mechanisms occurring due to the Magnon-phonon coupling indicating the UM dissipates energy to the lattice, directly or indirectly by intermediate interaction with spin waves. Based on [53].

2.4. Spin Pumping

The discovery of the spin pumping and spin current injection had started with the first principles of the spin-polarized transport presented in the pioneering work by Mott in 1936. He postulates that the spin mean free path in FM metals is much longer than the electron mean free path. This means the electron transports in FM metals have different channels based on their spin state. This scenario yields a difference in the DOS for the two-electron spins which results also from the antisymmetric situation for both spins wavefunction due to Pauli exclusion principle.

This antisymmetry affects the total energy of the system which results in energy shift called exchange energy [2] E_{ex}. This situation shown in Fig. 2.6b which indicates the FM system in equilibrium case. This is distinctly different from the case of normal metals where DOS for electrons near E_F are equal for spin-up and spin-down states (Fig. 2.6 a). The spin pumping can be understood in terms of the spin accumulation induced by the change in magnetization in FM. Basically, the

---

[2]The energy due to exchange interaction is described using Heisenberg Hamiltonian $\mathcal{H} = -\sum_{ij} A_{ij} S_i.S_j$, A_{ij} is exchange constant and S_{ij} are spin states. In FMs , E_{exc} favors parallel alignment of electron spins and this exchange interaction is dominant over a length l_{ex} given by $l_{ex} = \sqrt{\frac{A}{2\pi M_s^2}}$ [52].

change in the magnetization leads to spin accumulation, and this results in a shift in the energy bands between both spin states (Fig. 2.6 c). Electrons with $E > E_F$ relax by filling the lower energy state through spin flip process till both states go back to the equilibrium E_F (Fig. 2.6d). This relaxation process is enhanced when an adjacent normal metal is attached to the FM layer and a spin current carrying angular momentum is pumped through the FM/NM interface. The resulting spin current J_s is easily defined as the difference of the current density for both individual current $j_\uparrow$ and $j\downarrow$, as $J_s = \frac{\hbar}{2e}(j_\uparrow - j\downarrow)$.
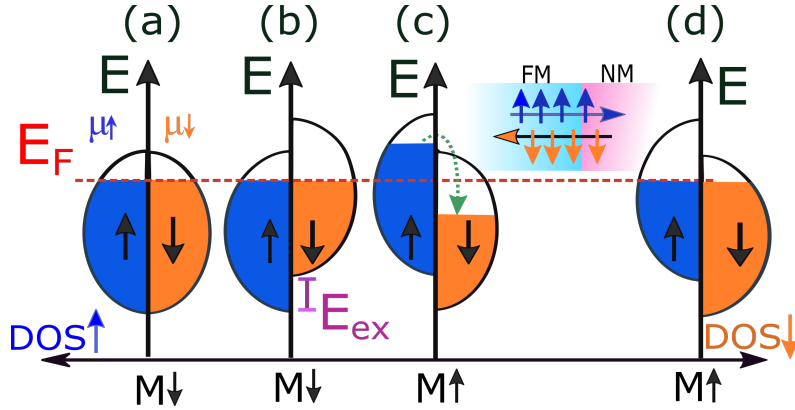
Figure 2.6 – A schematic representation of the spin pumping in terms of the electrons DOS and spin accumulation. (a) DOS for both spin states in the normal metal. (b) DOS for spin states in FMs in equilibrium. (c) DOS in FM where spin accumulation is induced by magnetization change which drives the energy levels from equilibrium. (d) Relaxation process for the electrons with $E > E_F$ through spin flip mechanism which drives them back into equilibrium.

The transfer of the angular momentum from FM into spin-sink occurs also when using FM insulator. This case refers to the *spin pumping* as distinct from the spin injection mechanism which usually is linked to the conducting FMs. In the spin pumping, the angular momentum is carried in the FM insulator and flows into an adjacent material due to spin gradient - spin accumulation - caused by magnetization precession induced by FMR [5–14] or due to thermal gradients in the FM [15–17].

In the spin pumping induced by FMR, the precession of magnetization in the FM insulator results in a non-equilibrium in the spin chemical potential for the spin-up and spin-down $\mu^\uparrow$ and $\mu^\downarrow$. This non-equilibrium refers to the (spin accumulation) $\mu_s = \mu^\uparrow - \mu^\downarrow$ which can diffuse into the nonmagnet, Fig.2.7. The resulting spin current J_s in this case depends on the gradient of the spin accumulation as $J_s \propto \nabla \mu_s$.

The chemical potential decay and then splitting at FM/NM interface are illustrated in figure 2.7. In FM insulator (e.g YIG) as a spin current source, a magnon chemical potential μ_m is introduced where a pure spin current is pumped into NM. μ_m and its relaxation is different from the case of spin-polarized current injection. Here the spin current is pumped as a result from the difference in the $\Delta\mu_m$ around the interface and also from the interaction between the localized spins at the FM with the conduction electrons at the NM. This case is illustrated in figure 2.7a.
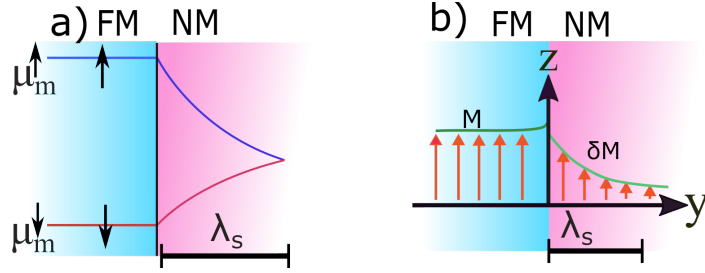
Figure 2.7 – Spin pumping and spin accumulation- Chemical potential decay $\mu_e^{\uparrow\downarrow}$ and splitting at the FM/NM interface.(a) The $\mu_m^{\uparrow\downarrow}$ splitting and then decay when pumping pure spin current from FM insulator where the SDL (λ_s) of FM is very long. λ_s represents the length where the spins are flipped in NM due to their interaction with the localized spins in FM . (b) The spin accumulation concept in terms of the nonequilibrium magnetization δM (which is equivalent to $\nabla\mu_s$) induced by the magnetization precession in FM. δM diffuses into NM in a length scale characterized by the spin diffusion length λ_s. These schemes are created based on [13, 55].

The chemical potential gradient $\nabla\mu_s$ (spin accumulation) driving spin pumping also describes the spatial magnetization nonequilibrium δM. Therefore, the spin pumping can be explained in terms of the spatial magnetization nonequilibrium δM through the NM, [13, 55] as shown in figure 2.7b.

δM can be achieved either by injecting spin-polarized current [13, 55] or through magnetization precession around H_{ext} which is driven from the equilibrium by ferromagnetic resonance, section 2.2. The effective decay length is equivalent to the spin diffusion length λ_s of the nonmagnet.

In the spin pumping process, the spin accumulation has a time-independent component which is collinear to the external bias field of the FMR and a time-dependent precessing component which is perpendicular. If the spin accumulation created in the nonmagnet experiences sufficient spin flip, it does not flow back into the ferromagnetic material, and the out diffusion of the spin current reduces the spin accumulation in the FM. The spin pumping induced by time-independent spin accumulation results in dc spin current diffusion into the NM and damping increase, and this case is illustrated in figure 2.8.
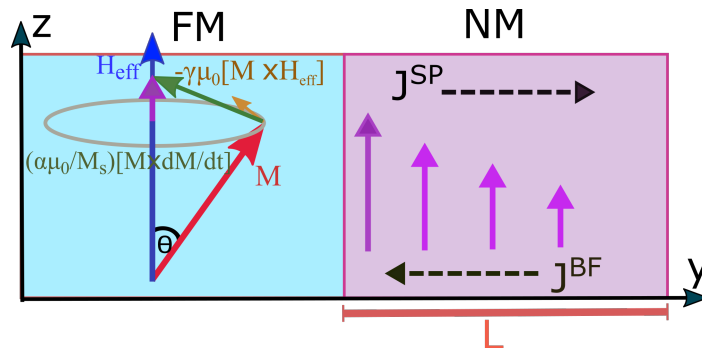
Figure 2.8 – Schematic view of FM/NM bilayer illustrates the time-independent component of the spin accumulation resulting from the magnetization precession in FM around H_{ext}. This component is responsible for the dc spin current pumped into NM which relaxes by spin flip and then produces a dc voltage by ISHE.

2.4.1. Spin Current Injection and Relaxation in Spin Sink

Following the model presented by Tserkovnyak *et al.*,[56], and assuming NM with a finite length L extends from the interface (y=0) to y=L, figure 2.8, the spin accumulation $\mu_s(y)$ flowing along y into the normal metal is defined by the spin diffusion equation

$$\frac{d\mu_s}{dt} = D\Delta\mu_s - \tau_s^{-1}\mu_s \tag{2.34}$$

Solving this equation using the boundary conditions for the spin accumulation at $y(0,L)$ we get

$$\mu_s(y) = \frac{cosh\ k(y-L)}{sinh\ kL}\mu_s^0 \tag{2.35}$$

Where the total spin accumulation $\mu_s^0 = [2I_s]/[\hbar\mathcal{N}SDk]$. $\mathcal{N}$, S D are the DOS, area of the interface and the spin diffusion coefficient, respectively.

In conventional NM, the diffusion of the spin accumulation across the NM is not conserved process, but it experiences a decay due to the spin-flip induced by the SOC. k is the wavevector and it is given by

$$k = \frac{[1+i\omega\tau_s]^{1/2}}{\lambda_s} \tag{2.36}$$

For most of high-Z metals, $k \simeq 1/\lambda_s$ and this approximation is valid if we assume the precession frequency ω is smaller than the spin-flip relaxation rate $(1/\tau_s)$ [56].

The spin diffusion length λ_s and spin-flip time τ_s are related via the diffusion coefficient D

$$\lambda_s = \sqrt{D\,\tau_s} \tag{2.37}$$

Using equation 2.35, and referring to the derivation details reported in [56–58], the decay of the spin accumulation μ_s along y causes a spin current J_s. The spin current change in the NM thickness d_{NM} along y direction from the interface is given by

$$J_s(y) = J_0\frac{sinh\ (d_{NM}-y)/\lambda_s}{sinh\ d_{NM}/\lambda_s} \tag{2.38}$$

where J_0 is the spin current at the FM/NM interface (y=0) and it is equivalent to the pumped spin current J_s^{sp}. The decay of the spin current along the NM demonstrated by equation 2.38 is illustrated in figure 2.9 for different d/λ_s cases. As shown in this figure, when d $\gg \lambda_s$ the spin current decay is large due to the high spin relaxation through spin flip process, and most of the spin current vanishes in the spin-sink before reaching its surface. In this case, the net spin current J_s^{net} out of the pumped current J_s^{sp} is high and the backflow current J_s^{BF} is small. On the other hand, when d $\ll \lambda_s$ the relaxation of the spin current is very weak and this results in large spin accumulation. The large spin accumulation created here induces more backflow current J_s^{BF}, therefore most of the pumped current flows back to the FM [52, 56, 59]. As explained here, the spin pumping process includes three currents, the pumped spin current J_s^{sp}, net spin current J_s and backflow spin

current J_s^{BF}. In this situation, the net spin current flowing into NM is given by

$$J_s^{net} = J_s^{sp} - J_s^{BF} = \frac{\hbar}{4\pi}\Big(A_r^{eff}m \times \frac{dm}{dt}\Big) \qquad (2.39)$$

where $A_r^{eff} \simeq g_{eff}^{\uparrow\downarrow} \simeq [g^{\uparrow\downarrow}]/[1 + \beta g^{\uparrow\downarrow}]$. β is the backflow parameter and it is expressed as $\beta = \frac{\tau_{sf}\delta_s/h}{tanh(d_{NM}/\lambda_s)}$. δ_s is the spin-flip scattering energy δ_s ($= 1/[\mathcal{N}S\lambda_s]$) [56]. In perfect spin-sink materials like Pt and Ta, when the d $> \lambda_s$,J_s^{BF} is not significant. However, it becomes very significant for the ultrathin films and also for nonperfect spin sinks like semiconductors and organic materials [8].
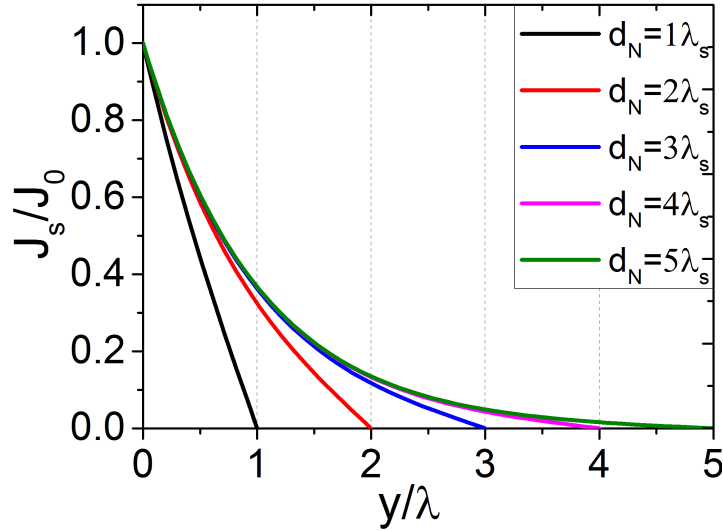
Figure 2.9 – The decay of J_s along the NM at different NM thicknesses d_N compared to the λ_s. The curves are plotted according to equation 2.38.

2.4.2. Spin Mixing Conductance and Effective Damping

The recent theories on the spin pumping into nonmagnetic materials were inspired by the theory of DC current pumping presented by Brouwer in 1998 [60]. Brouwer derived a formula that relates the pumped DC current to the parametric derivatives of scattering matrix S(X1, X2) of the system. Adopting Brouwer's theory, Tserkovnyak *et al.*, presented a mechanism for the spin pumping based on the scattering at the time-dependent spin potential at the FM/NM interface [11]. To shed light on the role of the FM/NM interface as the main environment for the spin pumping, we follow the approach by Tserkovnyak, Brataas and Bauer [11, 56]. As explained in detail in the previous sections, the enhancement of the magnetic damping in the FM/NM system results in a spin current J_s^{sp} to leak into the adjacent NM as a result from the magnetization precession in FM material. The resulting spin current pumped by magnetization precession perpendicular to the interface is

$$J_s^{sp} = \frac{\hbar}{4\pi}\Big(A_r m \times \frac{dm}{dt} - A_i\frac{dm}{dt}\Big) \qquad (2.40)$$

Where A_r and A_i are interface parameters defined as,

$$A_r = \frac{1}{2}\sum_{mn}\left[|r_{mn}^{\uparrow} - r_{mn}^{\downarrow}|^2 + |t_{mn}'^{\uparrow} - t_{mn}'^{\downarrow}|^2\right] \tag{2.41}$$

$$A_i = Im\sum_{mn}\left[r_{mn}^{\uparrow}(r_{mn}^{\downarrow})^* + t_{mn}'^{\uparrow}(t_{mn}'^{\downarrow})^*\right] \tag{2.42}$$

Where $r_{mn}^{\uparrow}(r_{mn}^{\downarrow})$ and $t_{mn}'^{\uparrow}(t_{mn}'^{\downarrow})$ are the reflection and transmission coefficient for spin-up (spin-down) electrons at FM/NM interface. m and n label the transverse modes at the Fermi energy in the adjacent normal metal. Equations 2.42 and 2.41 can be written as

$$A = [A_r + iA_i] = g^{\uparrow\downarrow} + t^{\uparrow\downarrow} \tag{2.43}$$

$g^{\uparrow\downarrow}$ and $t^{\uparrow\downarrow}$ denote the interface spin mixing conductance and transmission coefficient, respectively. When FM film is thicker than the transverse spin-coherence length $d > \lambda_{coh}$, $(\lambda_{coh} = \pi/(k_F^{\uparrow} - k_F^{\downarrow})$, where $k^{\uparrow\downarrow}$ is the spin-dependent Fermi wave vector), $t^{\uparrow\downarrow}$ vanishes. For several normal metals used as a spin sink in spin pumping such as Pt and Ta, λ_{coh} is very small. Hereby, the spin pumping through the interface is controlled by the reflection parameters $A_r \simeq Re[g^{\uparrow\downarrow}]$. Only the real part will be considered in this work since $Im[g^{\uparrow\downarrow}]$ vanishes for the diffusive and ballistic FM/NM contacts [11, 61]. Using this assumption, equation 2.40 becomes

$$J_s^{sp} = \frac{\hbar}{4\pi}\left(A_r m \times \frac{dm}{dt}\right) \tag{2.44}$$

From conservation of the angular momentum, assuming the entire emitted spin current is absorbed in NM [52], one can get

$$J_s^{sp} = \frac{1}{\gamma}\frac{dM_{tot}}{dt} \tag{2.45}$$

where $M_{tot} = MV$ is the total magnetic moment through the entire FM volume V. From equations 2.44 and 2.45 we get,

$$\frac{dm}{dt} = \alpha_{sp}\left(m \times \frac{dm}{dt}\right) \tag{2.46}$$

α_{sp} denotes to the spin pumping contribution to the Gilbert damping constant which represents the magnetic damping enhance due to the spin pumping process into the FM/NM interface. α_{sp} can be obtained after carrying out simple algebraical steps as [52]

$$\alpha_{sp} = \frac{g\mu_B g^{\uparrow\downarrow}}{4\pi M_s d_F} \tag{2.47}$$

Eventually, for FM/NM bilayer system, the net magnetic damping will be

$$\alpha = \alpha_0 + \alpha_{sp} \tag{2.48}$$

where α_0 is the initial magnetic damping which is equivalent to the damping of the bare FM. Spin mixing conductance $g^{\uparrow\downarrow}$ is an important factor in spin pumping

processes and spinterface phenomenon and it tells a lot about the spin pumping transparency. Due to its dependence on both, interface and the spin-sink material, $g^{\uparrow\downarrow}$ is considered not only an interface parameter but also a bulk parameter.

It is worth mentioning that, equation 2.47 is valid when we have a perfect spin sink where the injected spins relax very quickly due to the high spin-flip rate. This case is consistent with some normal metals like Pt, Ru, and W. In this situation, any backflow results from spin accumulation will be very small. However, on the other side when the spin sink has a small spin-flip rate which results in a small spin relaxation for the injected spins, like the case in some NMs and most organics . In this situation, a significant amount of spins return back to the FM (J_s^{BF}) and then the spin pumping contribution to the magnetic damping becomes α_{sp}^{eff}

$$\alpha_{sp}^{eff} = \frac{g\mu_B g_{eff}^{\uparrow\downarrow}}{4\pi M_s d_F} \tag{2.49}$$

$g_{eff}^{\uparrow\downarrow}$ is the effective spin-mixing conductance for the system and it affects the net spin current as shown in equation 2.39. $g_{eff}^{\uparrow\downarrow}$ is given by [10, 56]

$$g_{eff}^{\uparrow\downarrow} = g^{\uparrow\downarrow}\Big[1 + g^{\uparrow\downarrow}\frac{\tau_s\ \delta_s/h}{tanh(d_{NM}/\lambda_s)}\Big]^{-1} \tag{2.50}$$

δ_s is linked to the spin resistance R_s of the spin-sink material as

$$\delta_s = \frac{R_s h}{\tau_s} \tag{2.51}$$

R_s is the resistance per spin in units of h/e^2 of the spin-sink with thickness λ_s. In terms of R_s, and for the case of $d \longrightarrow \infty$, the effective spin mixing conductance $g_{eff}^{\uparrow\downarrow}$ in equation 2.50 can be simplified as

$$\frac{1}{g_{eff}^{\uparrow\downarrow}} = \frac{1}{g^{\uparrow\downarrow}} + R_s \tag{2.52}$$

Based on equation 2.51 and the definition of δ_s, $g_{eff}^{\uparrow\downarrow}$ can be written as

$$\frac{1}{g_{eff}^{\uparrow\downarrow}} = \frac{1}{g^{\uparrow\downarrow}} + \frac{e^2\lambda_s}{h\sigma S} \tag{2.53}$$

where $\sigma = D\mathcal{N}e^2$ which results from the Einstein's relation which links σ and D. Equation 2.53 clearly demonstrates that, the effective spin pumping out of the FM/spin-sink interface is governed by the effective spin-mixing conductance which is strongly depends on the spin diffusion length and the conductivity of the spin-sink. Furthermore, from this equation we can elucidate two cases, small $g^{\uparrow\downarrow}$ leads to weak spin pumping and on the other side, large λ_s causes large back flow and small net current J_s^{net}. This explains the weak spin pumping into weak SOC materials with large λ_s as also shown in experiments [8]. Furthermore, the proportional relation $R_s \propto (\lambda_s/\sigma)$ assumes a constant $g_{eff}^{\uparrow\downarrow}$ when σ of the spin sink is proportional to λ_s. This case addressed here is important when studying ISHE at different temperatures T when the change in T influences σ and λ_s and hence R_s. The $R_s - T$ relation

then defines how does $g_{eff}^{\uparrow\downarrow}$ change with T. The effective additional damping due to the spin pumping α_{sp}^{eff} will be written as

$$\alpha_{sp}^{eff} = [\frac{g\mu_B}{4\pi M_s d_F}][\frac{1}{g^{\uparrow\downarrow}} + \frac{e^2\lambda_s}{h\sigma S}]^{-1} \tag{2.54}$$

As it is shown from this equation, any additional damping due to spin pumping is suppressed by the additional effect added by the second term in the RHS of equation 2.54. This is due to the weak spin-flip rate in the spin-sink which results in flowing of the spin angular momentum back to the FM. This situation is unlikely for the perfect spin sink materials which have high spin-flip rate and small spin diffusion length[10, 56].

More clarification for the effective spin mixing conductance $g_{eff}^{\uparrow\downarrow}$ can be made by recalling the resistor model [Fig. 2.10]. Based on the equivalent circuits drawn here, the spin resistance R_s of the spin sink acts as a short resistance (shunting path) between the spins of the minority and majority spin channels. Adopting that, in perfect spin sink where λ_s is small, R_s becomes insignificant and the spin current is shorting through the normal metal without being affected by the R_s [Fig. 2.10a]. Here, the spin current is governed by the intrinsic spin mixing conductance $g^{\uparrow\downarrow}$. This situation is distinctly different from the case of large λ_s which yields high R_s and hence the spin mixing conductance decreases. In this case the spin current is significantly affected by R_s and governed by $g_{eff}^{\uparrow\downarrow}$, [Fig. 2.10b].
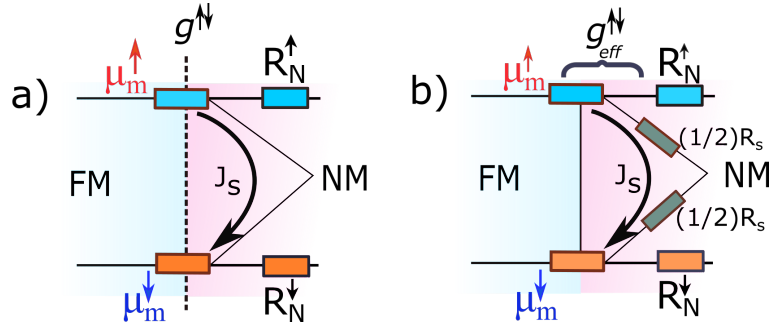
Figure 2.10 – Schematic illustrations of $g^{\uparrow\downarrow}$ and $g_{eff}^{\uparrow\downarrow}$ in NM. (a) The spin current is shunting through the NM with no influence by R_s. In this case only the intrinsic spin-mixing conductance $g^{\uparrow\downarrow}$ is considered for the spin pumping. (b) The case when R_s is significant where it acts as a shorting path for the spin current. The spin current here is governed by $g_{eff}^{\uparrow\downarrow}$. Here $R_N^{\uparrow}$ and $R_N^{\downarrow}$ are the spin-up and spin-down resistors, respectively, where $R_N^{\uparrow} = R_N^{\downarrow} = 2\,R_N$.

2.5. Spin-Charge Interaction

The interaction between spin and charge which includes generation and detection of spin currents is encapsulated by three known mechanisms: anomalous Hall effect (AHE), spin Hall effect (SHE) and inverse spin Hall effect (ISHE). Spin-orbit coupling (SOC) is the central hallmark for these three mechanisms.

2.5.1. Spin-Orbit Coupling - SOC

Spin-orbit coupling (SOC) is a relativistic effect describing the coupling of the spin s and orbital l of the electrons. The corresponding Hamiltonian of SOC is given by [62],

$$H_{SO} = -\frac{e\hbar}{4m^2c^2}(\sigma.[E \times p]) \simeq \frac{e}{2m^2c^2}\left(\frac{dV}{rdr}\right)(s.l) \tag{2.55}$$

where σ is the spin factor of Pauli matrix and it is related to the spin angular momentum S

$$S = \frac{\hbar}{2}\sigma \tag{2.56}$$

$$\sigma_x = \begin{pmatrix} 0 & 1 \\ 1 & 0 \end{pmatrix}, \sigma_y = \begin{pmatrix} 0 & -i \\ i & 0 \end{pmatrix}, \sigma_z = \begin{pmatrix} 1 & 0 \\ 0 & -1 \end{pmatrix} \tag{2.57}$$

c, E, p, $\frac{dV}{dr}$, are the speed of light, electric field, electron momentum, and potential gradient, respectively.

Indeed, because SOC is linked to the $s-l$ interactions, it increases significantly with the atomic number Z [63, 64]. SOC is the origin behind spin-dependent scattering for charge currents. This scattering causes up and down spins to deflect in opposite directions. Three SOC mechanisms are included here, two extrinsic mechanisms, side-jump and skew scattering which are caused by impurity potential and one intrinsic mechanism which is related to the atomic structure.

Skew scattering (SS), refers to Mott scattering studied in relativistic physics in 1929 [65] which then was identified in FMs by Smit in 1958 [66]. This mechanism is an asymmetric scattering process originating from SOC between electrons and impurities in the material. In this mechanism, the final momentum directions of the spin-up and spin-down are different and the spin Hall conductivity σ^{xy} [3] is proportional to the momentum relaxation time τ_e [67].

Side-jump scattering (SJ), also originates from the presence of the material impurities and was first proposed by Berger [68]. SJ is superimposed on SS deflection after electrons are scattered from the impurities in multiple scattering events (Fig. 2.11), then they are deflected back because of the opposite field. As a result, the outgoing trajectories of the quasiparticle are displaced by a side-step shift Δ. In this case, σ^{xy} is independent of τ_e [59, 67, 69].

---

[3]$\sigma^{xy} \propto \frac{J_s}{J_c}$ and it is related to the spin Hall angle θ_{SH} and the electrical conductivity σ, $\sigma^{xy} = \sigma \times \theta_{SH}$

Intrinsic interaction (II) is dominant in large Z metals and ideal crystals. In this case, spin-orbit coupling in combination with virtual inter band transitions gives rise to spin-dependent transverse velocity [67, 69]. Like SJ, the spin Hall conductivity here is independent of τ_e. The three mechanisms are illustrated in figure 2.11.
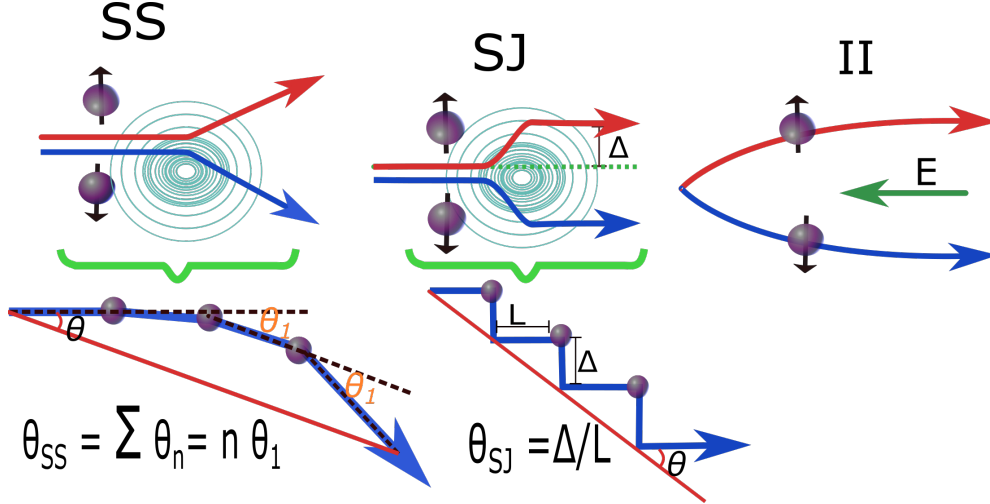
Figure 2.11 – Illustrations of the three mechanisms of the spin-orbit coupling including the extrinsic mechanisms, SS and SJ and also the intrinsic interaction II. The schemes are created based on [59, 69, 70]. Δ is the side-step displacement resulting from the SJ scattering process.

2.5.2. Spin-Hall Effect - SHE

As a consequence of the microscopic scattering processes discussed in the previous section, two mechanisms manifest macroscopically, i.e AHE and SHE. The spin Hall effect (SHE) was first proposed in 1971 by Dyakonov and Perel [71] and explained by the relativistic interactions between spin and orbit of electrons in metals. This transforms charge current into a transverse spin current. Then later, a theoretical work by Hirsch triggered this process' resurgence calling this phenomenon spin-Hall effect (SHE) [72]. He also proposed a way to experimentally measured spin current using the same principle that allowed the spin imbalance to be created in the first place. Thereafter, many works have investigated this phenomenon electrically [73–77], and optically [73, 78, 79].

The AHE case can be explained by the conducting FM's DOS for spin-up (majority) and spin-down (minority) electrons which are unequal. The majority electrons scatter in one direction and minority scattered in an opposite direction producing a transverse spin-polarized current. So this case will include creation of J_s and $J_c^{''}$ perpendicular to the generated charge current J_c. The case of AHE is illustrated in Fig. 2.12a. On the other hand, in nonmagnetic material the DOS for both spin states are equal and then the scattering rate is the same for both. As a result, the scattering processes create a pure spin current $J_s \perp J_c$, accumulating at the edges of the material. This case represents the SHE and it is illustrated in figure 2.12b.
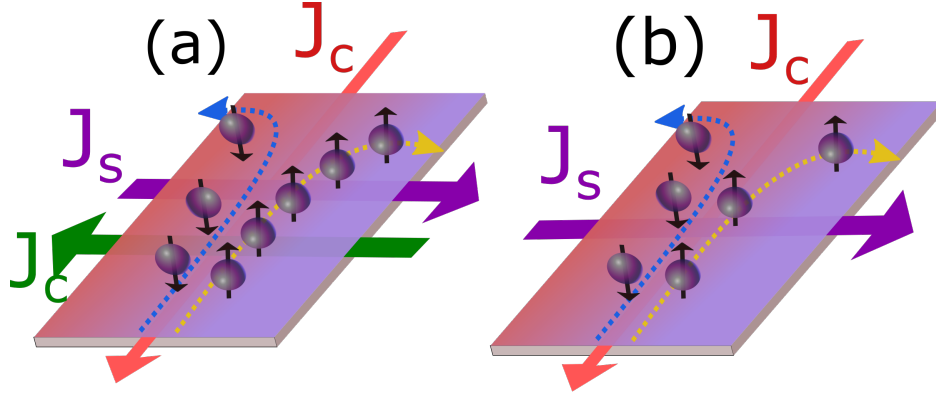
Figure 2.12 – (a) Illustration of AHE produced in FMs indicating both, the spin-polarized current J_c^s and spin current J_s perpendicular to the charge current J_c .(b) SHE which yields a pure spin current J_s also perpendicular to the charge current J_c .

The relation between J_s and J_c is defined by a vector product, and both are linked by the spin Hall angle (SHA) θ_{SH} which quantifies the spin-charge conversion efficiency in the NM [24].

$$J_s = \frac{\hbar}{2e}\theta_{SH}[J_c \times \sigma] \tag{2.58}$$

Where σ denotes the direction of the spin index, Fig.2.12b.

2.5.3. Inverse Spin-Hall Effect - ISHE

The ISHE is the reciprocal process of the SHE and it describes the conversion of spin current J_s into charge current J_c, a result of SOC in the materials, Fig 2.13a. Similarly, ISHE is linked to the SHA and J_c by a vector product as [7, 20, 24],

$$J_c = \frac{2e}{\hbar}\theta_{SH}[J_s \times \sigma] \tag{2.59}$$

It is obvious from this formula that, the DC voltage V_{ISHE} resulting in the ISHE process is measured in a direction perpendicular to both J_s and the direction of the spin polarization. This picture for V_{ISHE}, J_s and σ is illustrated in the figure 2.13b which shows a spin-pumping device composed of FM/NM bilayer structure. As shown here, the spin current J_s is injected from a FM into a NM across FM/NM interface. The resulting DC voltage is detected as $V_{ISHE}(x)$ where the spins polarization $\sigma(z)$ is oriented perpendicular to both $J_s(y)$ and $V_{ISHE}(x)$ and along H_{ext}.

Assuming the spin current $J_s(y)$ is injected uniformly across the whole NM layer which gives rise to the electric field $E(x)$. The value of this field and hence V_{ISHE} is obtained by integrating the spin current over the whole NM thickness [18, 58]

$$E(x) = \frac{\theta_{SH}}{\sigma_{NM}} < J_s(y) > \tag{2.60}$$

Using the spin current definition demonstrated by equations 2.38, 2.58 and 2.59 and considering the boundary conditions at y=(0,L) (equation. 2.34), we get

$$V_{ISHE} = -\frac{l\ \theta_{SH}\ \lambda_s\ tanh(d_{NM}/2\lambda_s)}{d_{NM}\sigma_{NM} + d_{FM}\sigma_{FM}}\left(\frac{2e}{\hbar}\right)J_0 \tag{2.61}$$

which yields

$$V_{ISHE} = \frac{-e\ \theta_{SH}\ \lambda_s\ tanh(d_{NM}/2\lambda_s)\ g_{eff}^{\uparrow\downarrow}\ f\ lP\ \Theta^2}{d_{NM}\sigma_{NM} + d_{FM}\sigma_{FM}} \tag{2.62}$$

Where l is the effective length of the area of spin pumping (the length of FM), P is a factor that arises from the ellipticity of the magnetization precession, and Θ is the cone angle [12, 18, 80]. The cone angle is given by $\Theta = [\gamma h_{rf}]/[2\alpha\omega]$, where h_{rf} is the MW field amplitude.
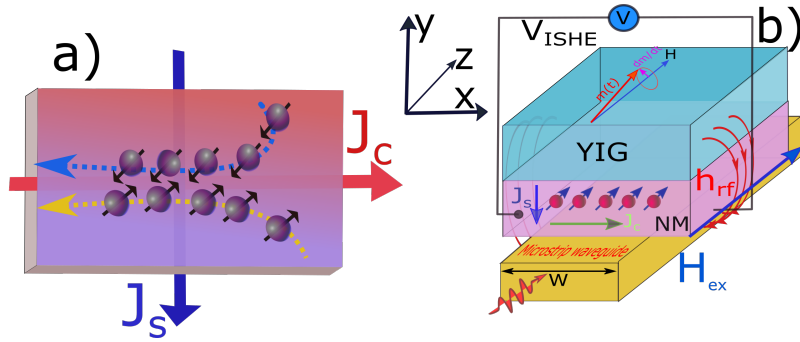
Figure 2.13 – (a) An illustration of the ISHE creation indicating the spin accumulation and the resulting charge current J_c. (b) A schematic of the FM/NM bilayer structure indicating ISHE measurements configuration during the spin pumping process. The microstrip waveguide is employed to transfer rf power which drives FM into the resonance.

Equation 2.62 represents the decay of the ISH voltage through the thickness of the spin-sink material. This equation is important for studying ISHE and it clearly shows that the resulting DC voltage significantly depends on the NM dimensions (length and thickness) and also the characteristic parameters (SHA, spin mixing conductance $g^{\uparrow\downarrow}$, and SDL λ_s) of the NM.

2.6. Spin Waves

Spin waves (SWs) represent the phase-coherent precession of microscopic vectors of magnetization propagating in the magnetic medium [81]. The low-energy quantized spin waves in the magnet are called magnons and it was first introduced by Holstein and Primakoff [82], and Dyson [83] who predicted they behave like Bosons obeying Bose-Einstein statistics.

Among the many types of spin waves and oscillations, one of the most important spin waves is that called magnetostatic spin waves (MSWs). MSWs are classified into three distinct classes depending on the direction of the magnetization vector - which is aligned to the effective magnetic field $\boldsymbol{H}$- relative to the wave propagation vector $\boldsymbol{k}$.

Backward volume magnetostatic spin waves (BVMSWs) have ($\boldsymbol{H} \| \boldsymbol{k}$). Whereas there are two different types associated with $\boldsymbol{H} \perp \boldsymbol{k}$. If $\boldsymbol{H}$ field is applied out of plane, the spin waves generated are forward volume magnetostatic spin waves (FVMSWs). If the $\boldsymbol{H}$ field is applied in plane, the spin waves generated are magnetostatic surface spin waves (MSSWs).
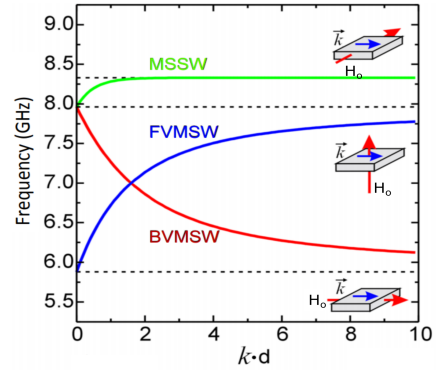
Figure 2.14 – Dispersion relation of the three SWs types, MSSWs, BVMSWs and FVMSWs. Adapted from [84].

The three MSWs classes are distinguished by different dispersion properties (i.e. f (k) relations) as shown in figure 2.14, [81, 84, 85].

MSSWs especially that so-called Damon-Eshbach modes (DEM) will be discussed in this section because these modes largely influence spin pumping and ISHE.

Spin pumping from spin waves

It was found that the FMR mode ($\boldsymbol{k} = 0$) isn't the only source for spin pumping. SWs contribute as well. The spin pumping efficiency for SWs becomes significant for low damping films like YIG [86–89].

Furthermore, spin pumping was found to be mode selective. More specifically, in thick FMs, MSSWs are more densely located at the surface where the dynamic magnetization is higher in the surface area than at the volume of the sample which is different from the volume waves where the magnetization over the whole volume. As a result, the coupling of the conduction electrons in NM with the MSSWs in FM is enhanced beyond the coupling with BVMSWs. Thus, MSSWs contribute more in the spin pumping process than BVMSWs [86, 87]. However, in thin FMs, both MSSWs and BVMSWs contribute equally to the spin pumping because the localization difference for both is not as strong as the case of thick FMs.

MSSW and spin heat conveyer

In the surface of the in-plane magnetized FM, MSSWs or that so-called DEM modes flow in direction $\boldsymbol{D}$ corresponding to

$$\boldsymbol{D} \| \boldsymbol{M} \times \boldsymbol{n} \tag{2.63}$$

Where $\boldsymbol{M}$ and $\boldsymbol{n}$ represents the uniform magnetization and the surface normal vector, respectively. This means, the modes moving in on side of film propagate in the opposite direction as the modes propagating on the other side of the film. This phenomenon called "field displacement nonreciprocity" [51, 90] and it is explained due to the difference in the k population for the DEMs on both sides of the film.

It was found that DEM in the range of microwave frequencies can convey heat at a far distance creating a negative temperature gradient different from conventional microwave heating, [90]. This phenomenon is illustrated in figure 2.15a.

In experiments, when SWs are excited in FM film (e.g YIG) via MW rf power using planar waveguides, the MW field is inhomogeneous through the FM thickness and decreases with the distance from the rf waveguide.

This means MW power absorption will be higher for the MSSWs at the surface close to the Rf source which results in transferring more heat than the other surface, figure 2.15b. This in turn, produces heat gradient ∇T between the two ends.

The temperature gradient ∇T caused by DEM in YIG was observed clearly not only in thick films [90], but also thin films [91, 92].

Although the thermal effect resulting here is relatively small, it becomes significant when used these FMs for spin pumping into an adjacent spin-sink with high thermoelectric-response i.e high Seebeck or Nernst coefficient.
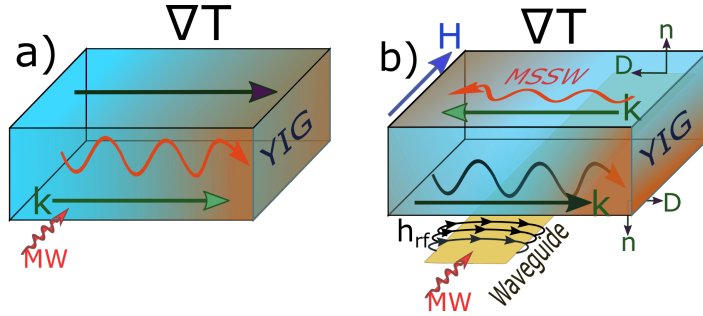
Figure 2.15 – The spin-heat conveyor in YIG due to DEM. (a) A schematic illustration of the thermal gradient created by the DEM flowing and conveying heat through FM material. (b) The nonreciprocity feature of the DEM created in both sides of YIG surface and the induced heat gradient. These schematics are created based on the spin-wave heat conveyor theory proposed in [90].

2.7. Organic Spintronics : Spins in Polymers

Unlike metals and inorganic semiconductors, organic polymers are highly flexible and can be easily integrated into many devices. Besides that, their electrical and thermoelectric properties can be easily tuned and controlled via doping [93–95].

These advantages make organic polymers promising candidates in microelectronics and flexible devices. However, employing polymers in spin pumping and ISHE is still very limited because their typically large spin diffusion length results in slow magnetization relaxation and weak spin pumping efficiency. Besides that, the small SOC results in weak spin-charge conversion which is measured by ISHE. One of the main polymer families is the π-conjugated polymers (πCP). In this section, some of the key spin-relevant features of πCPs are presented. In addition, the transport mechanism of spin carriers (polarons) and the spin relaxation mechanisms which have a major role in the spin transport in πCPs are also presented.

2.7.1. π-conjugated Polymers - πCPs

πCPs are polymers composed of series of molecular stacking layers with atoms connected via π-bonds resulting from p_z orbitals, figure 2.16. Despite the backbone structure containing σ-bonds, which result from the hybridization of sp^2 orbitals in C atoms, only π electrons are responsible for the material's electrical and optical properties. This is due to the large gap (several eVs) between σ electrons and the valence band. While π electrons are sensitive to the SOC in πCP, σ electrons only are effective when hyperfine interactions (HFI) of π electrons is considered [96]. For this reason , only π electrons are considered in many models studying πCPs [97, 98].

In heavy metals, high atomic number Z gives rise to the SOC as discussed in section 2.5.1. πCP on the other hand - like most of the organic materials - are composed of light atomic weight compounds which are mostly C-based. This leads to suppressed and weak SOC. Some polymers contain some medium weight atoms like sulfur, but the SOC is not affected as much as the case with heavy atoms. Besides that, the hopping events of the charge carriers take place at the cites of the C atoms.
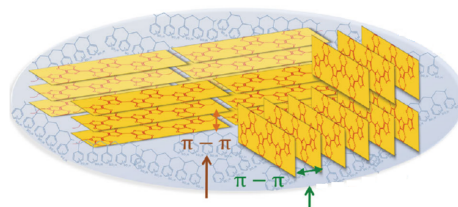
Figure 2.16 – An illustration of the $\pi - \pi$ stacking layers for πCPs PEDO:PPSS. Adapted from [99]

2.7.2. Polarons in πCPs

In order to understand the spin transport and spin relaxation mechanisms in πCPs, it is important to shed light on the spin carriers in these materials, polarons. In the language of condensed-matter physics, polarons are quasiparticles represented by electrons coupled to the quantized vibration of crystal lattice (phonons). This concept was first discussed in 1933 by Lev Landau in his work on the motion of the electrons in solids [100] and recently many studies have been done on this topic [101, 102]. Polaron type and size are features most relevant to organic spintronics.

The size depends on the distortion strength resulting from the displacement of

the atoms within the crystal structure due to the electron/hole -lattice coupling. Two types of polarons exists, electron-polaron and hole-polaron. Figures 2.17 show *e*-polaron and *h*-polaron with different sizes coupled with phonons. (More details can be found here [101, 102]).
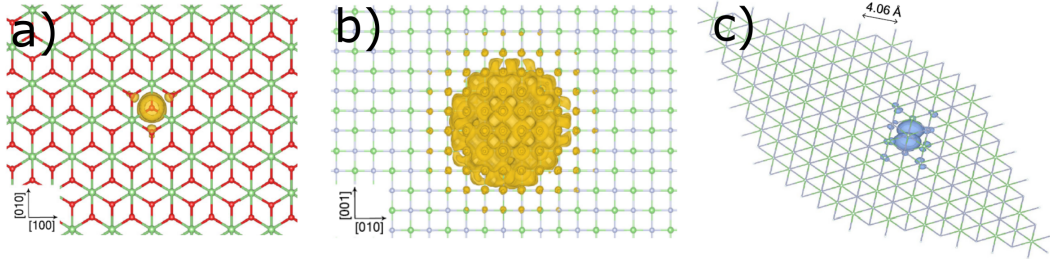
Figure 2.17 – Schematics for the polaron creation via the coupling between electron/hole and the lattice distortion. The schemes illustrate isosurface plots of the polarons density $|\psi|^2$ of LiF for a small size electron polaron a, large electron polaron b, and a hole polaron c. a,b are adapted from [101] and (c) is adapted from [102] .

2.7.3. Charge Carrier Transport Mechanism

The temperature dependence of conductivity and charge transport in πCPs are interpreted in terms of the variable-range-hopping (VRH) model which describes the hopping transport between localized states [4], [103, 104]

$$\sigma(T) = \sigma(0)exp\Big[-\Big(\frac{T_0}{T}\Big)^{1/d}\Big] \qquad (2.64)$$

T_0 is a material-dependent parameter called the characteristic temperature and it is linked to the DOS at Fermi energy level $g(E_F)$ and charge carrier localization length ζ via $T_0 = \beta/[g(E_F)\zeta^3 k_B]$ where k_B is the Boltzmann constant, β is a numerical factor (β= 18.1 - 21.1 in VRH model [105, 106]). $d = D+1$ where D represents the dimensionality of the charge carrier path [106]. For the 3D-VRH which characterizes most of the πCPs, (e.g PEDOT:PSS[5] d = 4 [106, 107]. However, for other πCPs like highly-doped PBTTT [6] d value was obtained between 2 and 3 [108].
The charge carrier localization length ζ depends on the πCP particle size and also the doping ratio. Its importance comes from its influence on the spin relaxation during the polaron transport in πCP. This is because a significant spin relaxation events during hopping in some highly-doped πCPs was found to take place not only during the single hopping event but also in the trap process after several hopping events [105], Fig.2.18. The magnitude of ζ fluctuates between less than a nanometer in some πCPs (e.g., PBTTT [30]) to several nanometers in others (e.g, PEDOT:PSS [109]. The polarons hopping, localization and relaxation lengths are illustrated in figure 2.18 which shows these parameters in FM/polymer bilayer.

---

[4]The states denote to localized states i,j which are occupied by two charge carriers separated by $r_{ij} = |r_i - r_j|$ and have energy $E_{ij} = e^2/kr_{ij}$, k is constant.

[5]PEDOT:PSS : poly(3,4-ethylenedioxythiophene):poly(styrenesulfonate)

[6]PBTTT : poly(2,5-bis(3-hexadecyllthiophen-2-yl)thieno[3,2-b]thiophene

The diffusion coefficient D_{hop} of the hopping polarons which carry spins through πCPs is linked to the spin-flip time τ_s by the equation $\lambda = \sqrt{D_{hop}\tau_s}$.

D_{hop} is temperature dependent and strongly depends on carrier mobility μ as defined by the Einstein relationship for thermally-excited transport [29, 30],

$$D_{hop} = \left(\frac{\mu k_B}{e}\right)T \tag{2.65}$$

In highly-doped semiconductors, the diffusion coefficient depends on the conductivity and the density of states at Fermi energy $g(E_F)$. This represents the degenerate case which is similar to the metallic systems [105, 109]. In this case, Einstein relationship has the form,

$$D_{hop} = \left(\frac{\sigma}{g(E_f)e^2}\right) \tag{2.66}$$
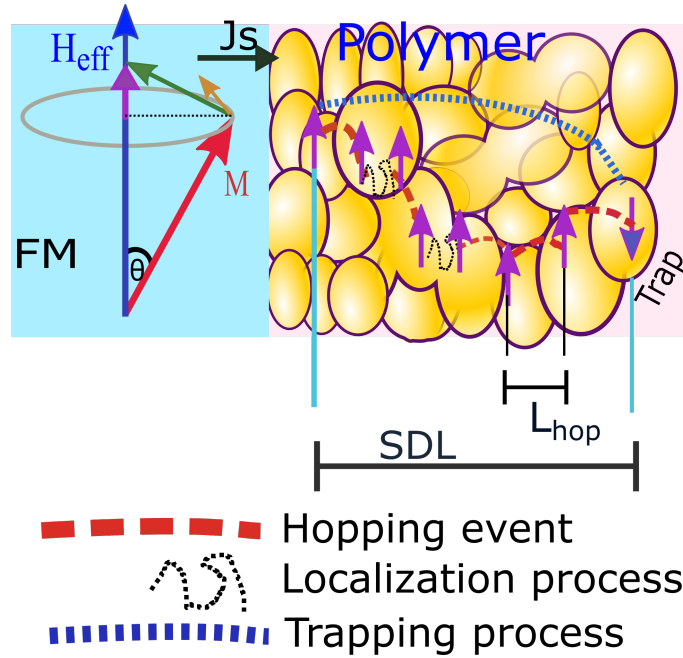
Figure 2.18 – Schematic of πCP indicating spin transport and relaxation in a polymer attached to FM. The hopping, trap, and localization events as well as the parameters SDL (λ_s), ζ are shown. This core-shell-like structure is similar to that reported for PEDOT:PSS πCP. The parameters illustrated in the schematic are defined according to [105].

2.7.4. Spin Relaxation Mechanisms in πCPs

In solids, there are four mechanisms for spin relaxation, the Elliott–Yafet (EY)[110], D'yakonov–Perel (DP) [111], Bir–Aronov–Pikus (BAP)[112] and hyperfine interaction (HFI) between nuclear and spin carriers (electrons or holes) [113]. Out of these four mechanisms, only EY and DP are significant in polymers. HFI is not effective in πCPs because the spin hopping events take place through states localized at C atoms which have no nuclear spin [113–115], unlike inorganic materials. Besides, HFI is also insignificant at high magnetic field regime. BAP also is insignificant in unipolar materials which have only either electron or hole charge carrier type, because the electron spin relaxation is linked to the exchange and annihilation interaction between electrons and holes. This is enhanced by the strong scattering of the holes by impurities and the fast relaxation of the hole spin [112, 115].

Elliott–Yafet - EY

In EY relaxation mechanism, spin scattering causes spin-flip during the momentum scattering events with phonons or impurities. This mechanism originates from the SOC discussed in section 2.5.1, which causes the spin wavefunctions to have a mixture of Pauli spin-up $|\uparrow>$ and spin-down $|\downarrow>$ states [13]. The spin relaxation rate $1/\tau_s$ in this approach is proportional to the momentum scattering rate $1/\tau_e$ as

$$\frac{1}{\tau_s} \simeq (\frac{L}{\Delta})^2 \frac{1}{\tau_e} \tag{2.67}$$

$(\frac{L}{\Delta})^2$ is a constant related to the spin-flip probability and composed of SOC matrix element between the adjacent bands L and the separation between these bands Δ [116].

D'yakonov–Perel - DP

This mechanism takes place when there is a lack of the inversion symmetry and causes spin state dependent transport. This splitting acts on the electrons as if an internal $\boldsymbol{k}$-dependent magnetic field is present [116]. This can be considered as a loss of spin coherence between scattering events due to the spin precession associated with the change of the $\boldsymbol{k}$ vector. The relation between τ_s and τ_e in DP mechanism is given by

$$\frac{1}{\tau_s} \simeq \Lambda^2 \tau_e \tag{2.68}$$

Here, Λ is the energy scale for the inversion symmetry breaking induced SOC [116]. Since the material resistance is linked to the momentum scattering rate, and also because resistance is temperature-dependent, one can study the behavior of the spin relaxation time with T. In πCPs, one can expect a different $\tau_s - T$ dependence from the case of NM because of the different dependence of σ on T in both cases. The combination of both mechanisms EY and DP scaled with the resistivity can be expressed as [117]

$$\frac{1}{\tau_s} = a\rho + \frac{b}{\rho} \tag{2.69}$$

a, b are constants linked to EY and DP mechanisms, respectively. According to this formula, when both mechanisms affect the spin relaxation, the entire τ_s will change with resistivity in nonmonotonic way. The relation of τ_s with the momentum scattering time τ_e for both mechanisms are depicted in figure 2.19.
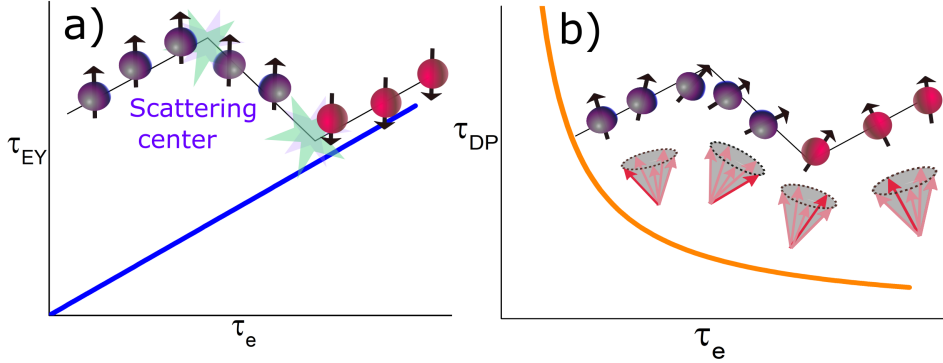
Figure 2.19 – Spin relaxation mechanisms illustrated by the relation between τ_s and τ_e for both EY and DP mechanisms. (a) EY relaxation mechanism where spins are relaxed by scattering from the impurities due to SOC. (b) DP relaxation mechanism where the spin coherence is lost between scattering events due to the spin precession.

2.8. Thermoelectric Response in πCPs

Due to their large influence on spin current measurements, the thermoelectric responses in πCP will briefly be discussed in this section. Among many thermoelectric effects reported in literature, only two will be discussed here due to their major influence on ISHE in πCP, namely the Seebeck effect and Nernst effect.

2.8.1. Seebeck Effect

Seebeck effect is a thermoelectic effect that refers to the generation of an electric field E in the material parallel to the temperature gradient ∇T generating it. The ratio of the resulting E to the thermal gradient is called Seebeck coefficient, $S = E/\nabla T$. Seebeck effect is characterized by the dimensionless thermoelelctric figure of merit [93]

$$ZT = S^2 \left(\frac{\sigma}{\kappa}\right) T \tag{2.70}$$

Where, σ is the electrical conductivity, κ is thermal conductivity and T is the absolute temperature. Although S is small for metals, it is relatively high for many polymers. At low κ, and high energy conversion efficiency $S^2\sigma$, high power factor ZT and then high thermoelectric response is obtained as described in equation 2.70, [94, 118].

Some metals like Pt and Ru have small $S \simeq 0$ and $1\mu V/K$, respectively [119], which is smaller than the S value for conducting polymers like highly-doped PEDOT:PSS which has S $= 20\mu V/K$ [93].

A smaller Seebeck coefficient ($\sim 1 - 10 \mu V/K$) was also found for πCP semiconducting PBTTT doped by F4TCNQ [7] in the high conductivity regime [94].

2.8.2. Nernst– Ettingshausen Effect

The thermoelectric effect emerging in the presence of magnetic field which generates a transverse electric field perpendicular to the both, the longitudinal thermal gradient and the magnetic field is called Nernst– Ettingshausen effect [120]. This voltage V_y resulting from this effect is expressed by the following equation

$$V_y = NlB_x\frac{dT}{dz} \tag{2.71}$$

Where, N, l, B, and dT/dz are the Nernst coefficient, effective material length, applied magnetic field, and the thermal gradient. It is clear from this equation that, the voltage that results here depends on the direction of B. When the magnetic field has opposite polarity, the effect's electric field reverses, too, figure 2.3.
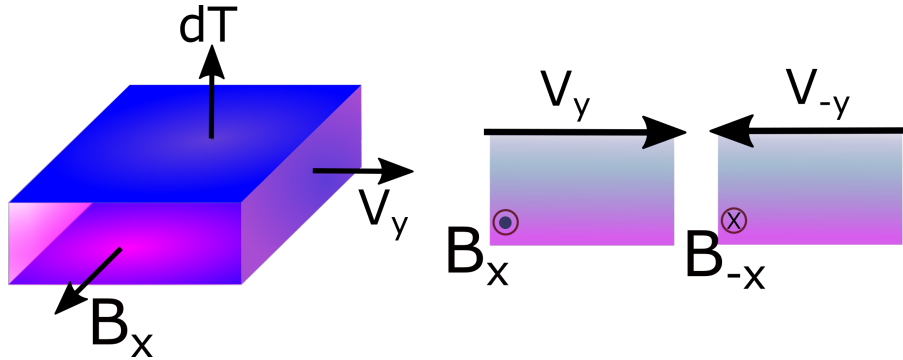
Figure 2.20 – A schematic illustration of the Nernst effect generated in the material producing a transverse electric field E perpendicular to the both, magnetic field B and thermal gradient dT. As illustrated here, the voltage polarity changes by changing B polarity.

In the spin Hall voltage measurements especially ISHE, at FMR condition the absorbed power in the ferromagnet leads to a local heating which causes a temperature gradient in the non-magnet perpendicular to its surface. The induced heating together with the external applied magnetic field produce a transverse voltage due to the Nernst effect. This voltage appears only at FMR, similar to the ISHE, and is reversed with magnetic field applied in the opposite direction. In polymers where the spin-charge conversion is very weak, the generated voltage is comparable to ISHE voltage.

---

[7]F4TCNQ: 2,3,5,6-tetrafluoro-7,7,8,8- tetracyanoquinodimethane

2.9. Materials under Investigation

In this section, the materials which compose the devices fabricated in this thesis are briefly presented. These include three materials , PEDOT:PSS, PBTTT and YIG ferrimagnet. The main properties of these materials which are related to this work will be outlined.

2.9.1. PEDOT:PSS

Poly(3,4-ethylenedioxythiophene):poly(styrenesulfonate) (PEDOT:PSS), is one of the polythiophene based πCPs and is considered to be a conducting polymer [8] because of its metallic-like conductivity, attributed to an intermediate energy bandgap of 1.6 eV [123]. This metallic feature is strongly linked to the large π-orbital overlap which relocalizes the carrier wavefunction at the Fermi energy E_F [109, 122].

The chemical structure of PEDOT:PSS illustrated in figure 2.21 a, shows that this polymer contains two parts, PEDOT and PSS.
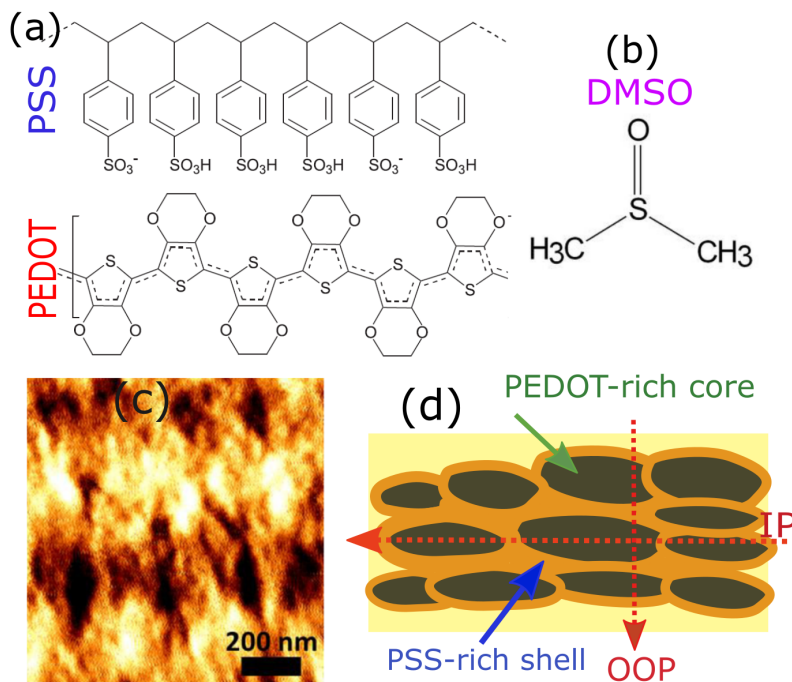
Figure 2.21 – Chemical structure of PEDOT:PSS, a and DMSO, b. (c) AFM image of PEDOT:PSS illustrating the core-shell-like structure. The dark domains are the PEDOT-rich and the light domains are the PSS-rich structures. This image is adapted from [124]. (d) A schematic of the anisotropic structure of PEDOT:PSS indicating the difference between the in-plane path (IP) of the charge carrier and the out-of-plane path (OOP) due to the antisymmetric core-shell structure.

From the microscopic point of view, the molecular structure of PEDOT:PSS man-

---

[8]Conducting polymers - distinct from metallic polymer like polyaniline - refer to the polymers which have semi-metallic features. They are characterized by a small band gap and low DOS at E_F. In contrast to metals and metallic polyaniline [121], semi-metal polymers have a high Seecbeck coefficient S [122].

ifests itself into PEDOT-rich core domains surrounded by PSS-rich shell domains. This is shown in figures 2.21 c,d. This elongated domain structures is the origin of the structural anisotropy in PEDOT:PSS which results in unequal in-plane (IP) and out-of-plane (OOP) conductivity [27] as it is illustrated in the schematic in figure 2.21d.

PEDOT:PSS has high water solubility due to the hydrophilicity of PSS with water, making it is easy to fabricate into smooth thinfilms using spin-coating [109]. It is widely used in electronics devices, diodes, transistors, hybrid solar cells [109, 125]. However, its weak SOC and small mobility μ [28, 108] hinder its use in spin pumping and ISHE experiments.

It is worth mentioning that, low μ hinders the use of PEDOT:PSS as a polaron transport medium as discussed in section 2.7.2. However, this can be compensated by increasing the carrier concentration via doping. A tremendous increase for the electrical conductivity (exceeding 1000 $S.cm^{-1}$) can be easily achieved via doping through the addition of high boiling-point solvents. This value is around five orders of magnitude higher than that of pristine polymer [122].

DMSO, figure 2.21b, is one of the most common dopants used in PEDOT:PSS. It influences electronic properties like carrier concentration and conductivity, and reduces the bandgap by raising the HOMO and lowering the LUMO energy levels [93, 122, 123]. It also influences the back-bone molecular structure via tuning $\pi - \pi$ stacking interdistance which plays a major role in the polaron size and transport [30, 93, 108, 122, 125].

Although the thermal conductivity of PEDOT:PSS is small compared to metals', (~ 0.3 W/(m.K) for the 5% DMSO doped polymer) [93], its thermolectric response namely Seebeck coefficient - which is highly relevant to the electrical efficiency - is relatively high and exceeds 20 $\mu V/K$ [93, 122]. Moreover, in some doping conditions this value reaches a level as high as $150\mu V/K$ [93, 122, 126] . The core-shell clusters in PEDOT:PSS along the polymer backbone structure have a size with diameter range between 20-60 nm. With this size, the localization length ξ is found to be in the range 8-44 nm [109, 127].

2.9.2. PBTTT

Another thiophene-based πCPs is poly(2,5-bis(3- alkylthiophen-2-yl) thieno [3,2-b] thiophene) (PBTTT), figure 2.22a . This polymer is well known in electronics field, especially for its use in organic field-effect transistors (OFET) because of its high field-effect mobility, (1.8 $cm^2 V^{-1} S^{-1}$) which is one of the highest reported to date [29, 108].

Unlike PEDOT:PSS, PBTTT is considered to be a semiconductor polymer because it exhibits a semiconductor-like conductivity and its semiconducting behavior [9] is conferred by its HOMO-LUMO gap which amounts to 2.2 eV [108, 123].

---

[9]Despite the PBTTT semiconductor not showing metallic charge transport like that in polyaniline [121], or semi-metallic like PEDOT-based polymers, it does show evidence of coherent charge transport in metallic grains at low temperature despite its relatively high E_g [108].
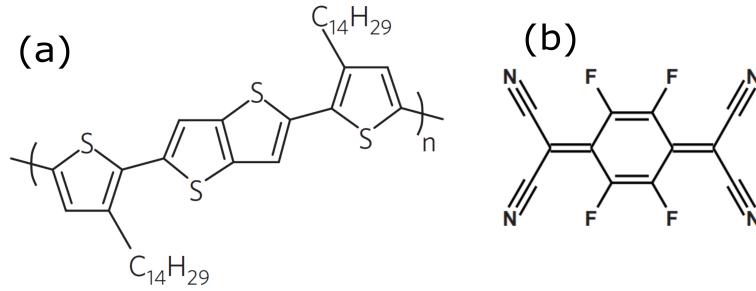
Figure 2.22 – Chemical structure of PBTTT, a, and F4TCNQ, b. Adapted from [29, 128].

Several doping approaches (chemically and electrochemically) have been used to increase the PBTTT conductivity, either those based on redox or acid-based reactions, [129] or co-depositing solution-processable πCPs with strong molecular acceptors such as 2,3,5,6-tetrafluoro-7,7,8,8- tetracyanoquinodimethane (F4-TCNQ) [130], figure 2.22b.

Even though it is easy and popular to use solution-based doping, it was found to insert some disorder into the π-stacking structure and the conductivity obtained was relatively low (~ 2 S.cm^{-1}) [130]. Only recently, a solid-state based doping method was performed via thermally evaporating F4TCNQ on the PBTTT layer and with this method, highly ordered lamellar microstructure and high conductivity polymer (~ 248 S.cm^{-1}) are achieved. More details about that reported here [108]. Such an optimized structure can be promising for spin current transport.

Despite the low thermoelectric efficiency (namely Nernst effect) of PBTTT compared to PEFOT:PSS, its Seebeck coefficient S was found to reach 10 $\mu V/K$ when its electrical conductivity reaches 100 S.cm^{-1} with high doping. On the other hand, S decreases ($\sim 1\mu V/K$) when σ increases beyond 100 S.cm^{-1} [94]. This large coefficient value implies the Seebeck effect must be considered when performing spin-transport measurements.

2.9.3. Yttrium Iron Garnet - YIG

Yttrium-Iron-Garnet (YIG) or $Y_3Fe_5O_{15}$ is a ferrimagnetic insulator is considered to be one of the lowest magnetic damping materials available [131, 132]. YIG has nearly cubic symmetry, definite composition, and only trivalent metal ions. Its cubic unit cell has a lattice constant of 12.37$\pm$0.004 Å and contains 24 Y^{3+} cations , 40 Fe^{3+} cations, and 96 O^{2-} ions . The Fe^{3+} cations are arranged in two sites, a octahedral site contains 16 Fe^{3+} ions and d tetrahedral site contains 24 Fe^{3+} ions. Y^{3+} cations are located in c sites called dodecahedral where each site is surrounded by 8 O^{2-} ions [19, 133, 134]. The three distinct sites with the composing ions are illustrated in figure 2.23b. The locations of these ions within the entire unit cell are illustrated in the figure 2.23a .

Because the Y^{3+} ions have no magneitc moment, the magnetic properties of YIG originate from the exchange interaction between sites a and d containing Fe^{3+} ions. Because each Fe^{3+} ion has magnetic moment of $5\mu_B$, this results in a magnetic moment of $40\mu_B$ for the unit cell [19]. This value corresponds to a saturation magnetization $4\pi M_s = 2470$ Oe which is equivalent to the $4\pi M_s$ measured for YIG

at 4.2K [135, 136]. The value of $4\pi M_s$ reported frequently in literature for YIG at room-temperature is around 1750 Oe [19, 137]. The octahedron-tetrahedron Fe^{3+} network leads to very low magnetic anisotropy which results in very low magnetic damping. As a consequence, YIG has the lowest magnetic damping reported among all magnetic materials. Very low damping values of around 2.7×10^{-5} and 6×10^{-5} are reported for YIG prepared by slow cooling [131] and LPE method [8], respectively. Moreover, several tens of nanometer-thick YIG deposited by PLD also shows an extremely low damping ($\sim 5.6 \times 10^{-5}$) [132]. Curie temperature T_C of YIG is as high as 560 k [138]. Because of this high T_C and ultra low damping, YIG is a very promising candidate for room-temperature magnetic devices and applications.
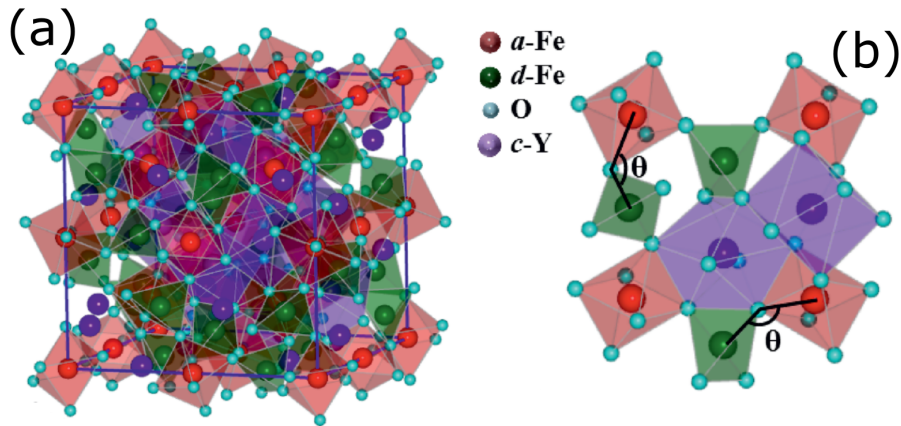
Figure 2.23 – Crystalline structure of YIG. (a) Schematic of the cubic unit cell of YIG indicating the locations of the ions Fe^{3+} , Y^{3+} and O^{2-}. (b) The cations arrangement at a vortex of sub unit cell illustrating O^{2-} ions surrounding the cations in the cites a, d, and c. Adapted from [134].

2.10. Tuning Conductivity in πCPs by Dedoping Process

Dedoping is the opposite process of doping. In the doping process, the dopant content in the polymer is enriched and consequently the conductivity increases. On the other hand for dedoping, the dopant ratio of the polymer is reduced gradually and is associated with conductivity reduction.

One of the most popular methods used in polymers to tune conductivity by dedoping is the thermal-based dedoping. This method is performed by applying a sequence of post-annealing steps on the polymer and during the annealing steps, the dopant content and conductivity are gradually reduced.

The main advantage of the dedoping process in polymers is that the dopant ratio, and hence the conductivity, can be tuned easily and efficiently without destroying the inner structure of the polymer. This is confirmed by some characterization studies reported here [30, 108]. Moreover, this is studied in detail within chapter 3 and chapter 6 of this thesis.

Chapter 3

3. Fabrication and Characterization Methods

This chapter is devoted to covering the details of fabrication and characterization methods which will be presented in two sections.

In the *first section*, we describe the materials used in all structures of our devices, exploring their fabrication conditions and important parameters.

The *second section* covers the setups and instruments employed for all FMR and ISHE measurements and also the characterizations done in this work. For all FMR and ISHE measurements, the cgs unit system will be used throughout the entire thesis.

3.1. Materials Fabrication

All main samples used in this work are composed of FM and spin-sink materials. The FM material used here is an epitaxial film of YIG. The spin-sinks are either platinum or πCPs. Two different πCPs are used, PEDOT:PSS and PBTTT. To measure ISHE, Pt, Ru, and Au electrodes are used.

3.1.1. YIG Fabrication and Surface Optimization

To make YIG ferrimagnetic layers, YIG wafers were purchased from Matesy [10] and grown by liquid phase epitaxy (LPE) on 0.5 mm layer of gadolinium gallium garnet $Gd_3Ga_5O_{12}$ (GGG) substrate. Using GGG substrate is important when depositing YIG because it has a lattice mismatch η of only 0.057%. This is calculated due to $\eta = (\alpha_G - \alpha_Y)/\alpha_Y \times 100$, where $\alpha_Y = 12.376$Å and $\alpha_G = 12.383$Å are the lattice constants for YIG and GGG, respoectivley [133]. For our experiments, we used LPE YIG with two thicknesses, 100nm and 200nm. The roughness of these samples was investigated using AFM, figures 3.1(a,b). The rms surface roughness observed for YIG was 0.28 nm.

In order to boost spin pumping from YIG into the spin-sink material, the YIG surface quality was enhanced employing a sequence of cleaning steps with organic solvents and also using Piranha as explained in appendix B. Our optimization of the YIG surface quality results in an enhancement of the spin pumping and a remarkable increase in the ISHE.

---

[10]https://www.matesy.de
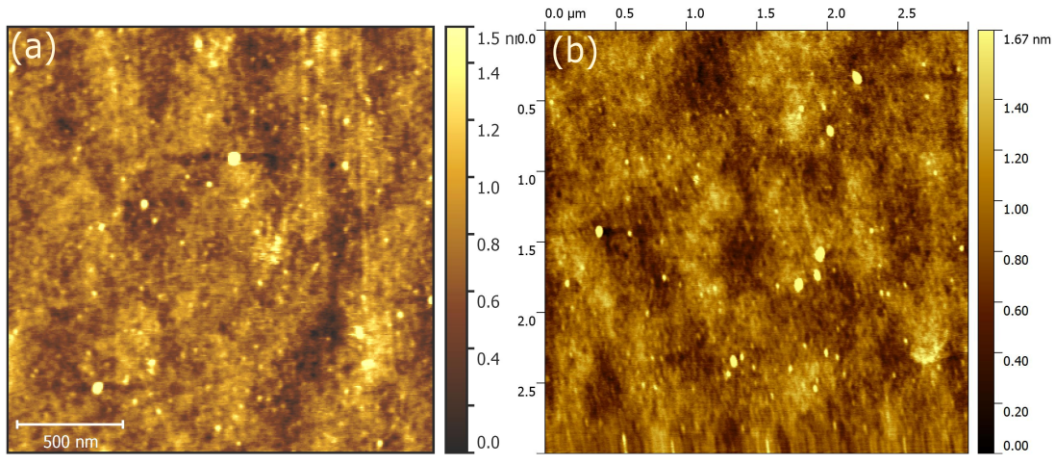
Figure 3.1 – AFM for the YIG (200-nm) surface at two different wafer areas.

These are illustrated in figure 3.2a, which shows the magnetic damping extracted from FMR measurements and in figure 3.2b, which shows the ISHE measurements carried out on two YIG/Pt samples. The first sample went through normal cleaning procedures with organic solvents (Acetone, IPA, NEP). The second sample went through the same cleaning procedure as the first with an additional cleaning step using Piranha. (The cleaning procedures are explained in appendix B).
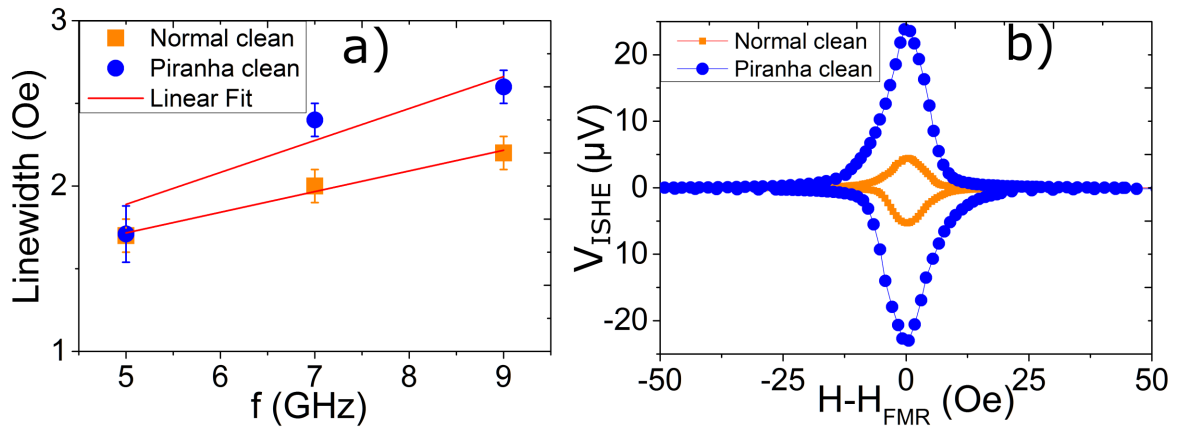
Figure 3.2 – The enhancement of spin pumping a, and ISHE b, due to the surface optimization obtained by piranha cleaning for the YIG surface compared to the normal cleaning procedures done using organic solvents. Both samples have YIG/Pt bilayer structure.

3.1.2. Fabrication and Preparation of Highly-doped PEDOT:PSS

The first πCP employed in the devices fabricated in this work was highly-doped PEDOT:PSS. An ultrathin layer of PEDOT:PSS was deposited using commercially available formulations in water (Clevios PH510, or PH1000 Heraeus). For all spin pumping and ISHE experiments, this solution was additionally doped with 5 $wt\%$ of DMSO to enhance the conductivity as discussed in section 2.9. A small amount of 0.5 $wt\%$ of Dynol is added to the PEDOT:PSS mixture to act as a surfactant, reducing

the surface dynamic tension during spin coating [139]. Ultimately, this enhanced the polymer adhesion. The solution is mixed in magnetic stirrer in an ambient cleanroom atmosphere for 2 h and then spin-coated at different speed depending on the desired thickness. Directly after the spin coating, the films are heated on a hot plate at 140 ^oC for 10 min. Different thicknesses of the PEDOT:PSS film were obtained by varying the spin-coating speed which allowed the range of thicknesses from 30 nm to 200 nm. The in-plane electrical conductivity σ_{IP} is massively increased due to DMSO doping. The σ_{IP} values obtained for the doped film are (300-560) S.cm^{-1} and (800-900) S.cm^{-1} for Clevios PH510 and PH1000, respectively. PEDOT:PSS is known for its highly anisotropic conductivity, so the σ_{IP} is significantly different from σ_{OOP}. The IP and OOP measurements were done on PEDOT:PSS film with thickness of 180 nm and 106 nm , respectively. The dimensions of the measuring area and the electrodes' width are illustrated in figures 3.3(a,b) inset, and also in figures 3.3(c,d). Figures 3.3(a,b) show the J-E plots obtained from the four-point resistivity measurements for PEDOT:PSS doped with DMSO in the, in-plane (IP) a, and out-of-plane (OOP) b, configurations. The conductivity values σ_{IP} and σ_{OOP} extracted from these plots are 900 S.cm^{-1} and 2.5×10^{-3} S.cm^{-1}, respectively.
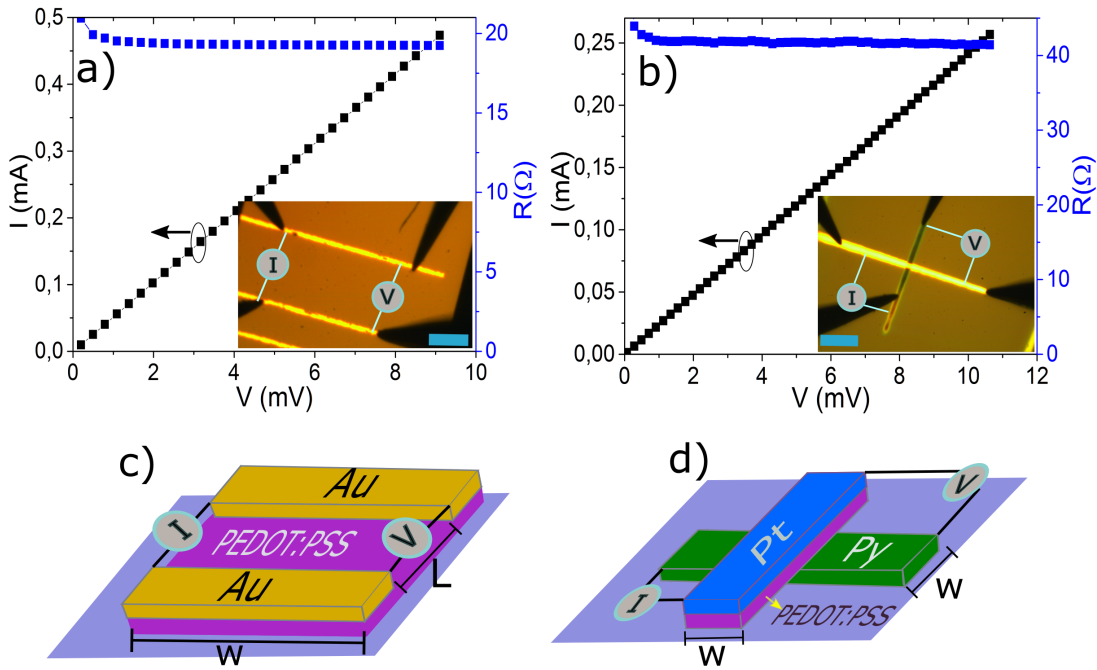
Figure 3.3 – Four-point resistivity measurements for PEDOT:PSS doped with DMSO in both, in-plane a, and out-of-plane b, configurations. The plots show J vs. E calculated from I-V values and the polymer dimensions. For in-plane, Ti/Au electrodes are used and for out-of-plane Py and Pt are used as bottom and top electrodes, respectively. The scale bar in the inset is 400μm. (c,d) Schematic illustrations of the IP and OOP resistance measurements, respectively. L= 1 mm, and w=3 mm for IP configuration. w=100 μm for OOP configuration.

3.1.3. Fabrication and Characterization of PBTTT

The fabrication and characterization steps of PBTTT polymer are done in Cavendish Laboratory in Cambridge by the microelectronics group. PBTTT is fabricated using a PBTTT solution made by dissolving the solid PBTTT-C14 into 1,2-dichlorobenzene (DCB) using concentration ratios for PBTTT:DCB between 10 and 25 (g/l) depending on the targeted thickness.

This PBTTT solution is then deposited onto YIG samples by spin-coating in a glovebox with N_2 atmosphere. Different spin-coating speeds are used to get different thicknesses in the range from 25 nm to 200 nm. Table 1 includes the deposition parameters with the associated concentrations and the obtained thickness.

Table 1 – Spin-coating parameters including the concentration ratios and the nominal thickness obtained for PBTTT.

Spin speed (RPM)	PBTTT:DCB ratio(g/l)	d(nm)
9000 for 60s	10	25
5000 for 60s	12.5	50
5000 for 60s	25	100
1500 for 60s	25	200

After spin-coating PBTTT, the film undergoes two post-annealing steps. First, the film is annealed at 120^oC for 2 min and then annealed at 180 ^oC for 20 min. This gradual annealing prevents any abrupt phase change which occurs between 140-160 ^oC. After annealing, the film is cool down gradually.

The conductivity of this polymer is enhanced by a solid-state doping method via thermal evaporation of F4TCNQ onto the PBTTT layers, figure 3.5a. F4TCNQ evaporation was done on a Kurt.J.Lesker thermal evaporator system number TUR050 in Nitrogen atmosphere under 3×10^{-6} mbar vacuum at a deposition rate of 0.9 $\pm$ 0.1 Å$/s$. The heater was ramped up to 110 ^oC, the F4 started evaporate around 80 ^oC. The dopant particles diffuse into the bulk of the PBTTT film during the evaporation and storage of the film at room temperature after deposition. In this diffusion process, the dopant particles make their way down to the substrate. This was confirmed by many characterization methods, discussed in detail here [108].

Figures 3.4a and b show a top-view and 3D AFM images of 100nm PBTTT film after evaporating F4TCNQ dopant and its diffusion into the polymer, respectively. The white pillars on the surface are dopant molecules which are absorbed by the polymer and diffuse into the polymer layers down till the substrate as demonstrated here [108]. The resulting PBTTT doped polymer has a uniform surface with an r.m.s surface roughness of 3 nm (measured in the $2\mu m \times 2\mu m$ square area as shown in figure 3.4c).
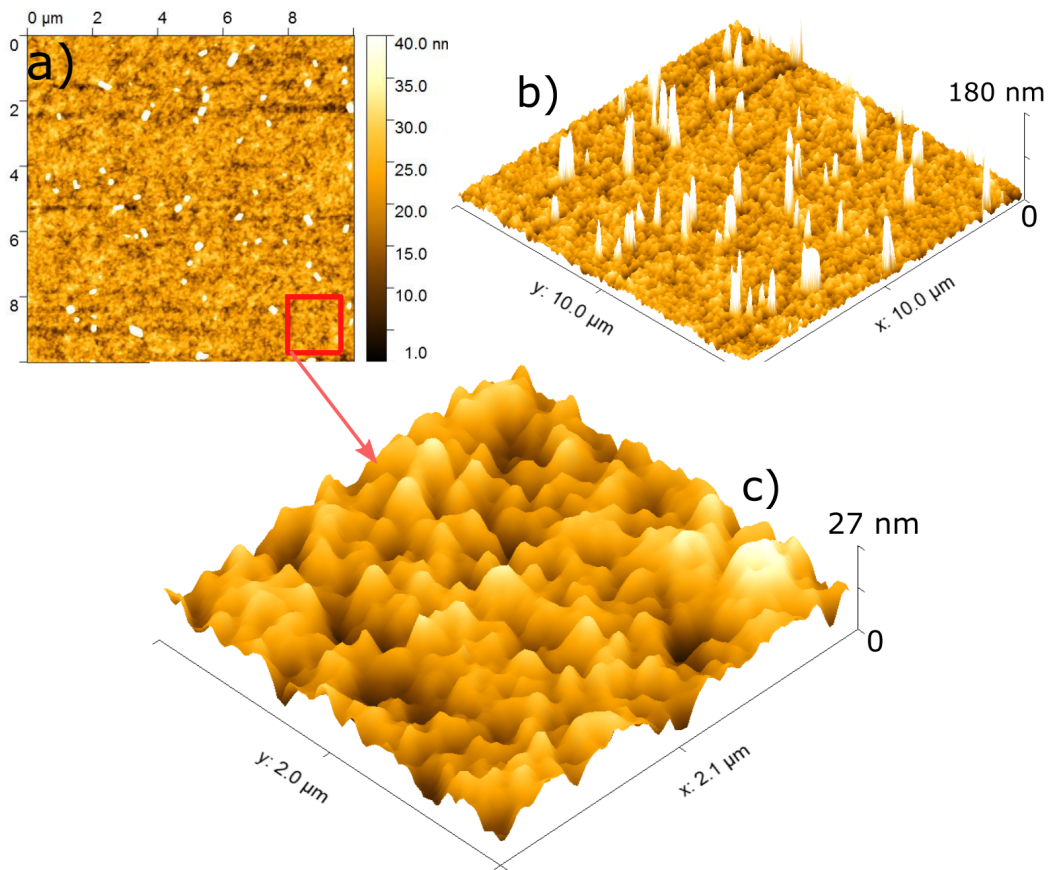
Figure 3.4 – (a,b) AFM surface image of PBTTT/F4TCNQ during the evaporation of F4TCNQ dopant and its diffusion into the polymer, respectively. The particles shown in the images are dopant particles which diffuse into the polymer down till the substrate. (c) A 3D AFM spot from PBTTT doped surface where no dopant left on the surface.

The resulting conductivity of the polymer is tuned by varying the amount of the F4TCNQ, done by varying the nominal thickness of the F4TCNQ deposited in the evaporation. The doping process done via thermally evaporating F4TCNQ on PBTTT is highly efficient and controllable, allowing the conductivity to tune through a wide range of values. And also as shown in Fig. 3.5b, the dopant diffuses throughout the whole film. This was confirmed by studying the depth profile of the composition ratio of the dopant to the polymer (F4TCNQ:PBTTT), characterized by measuring XPS scans while etching the film with an in-situ Ar ion-beam [108]. The molecular ratio F4TCNQ:PBTTT decreases exponentially from the polymer surface until around 10 nm deep. Farther down the ratio has a constant value 30% with nearly no change until the substrate.

41
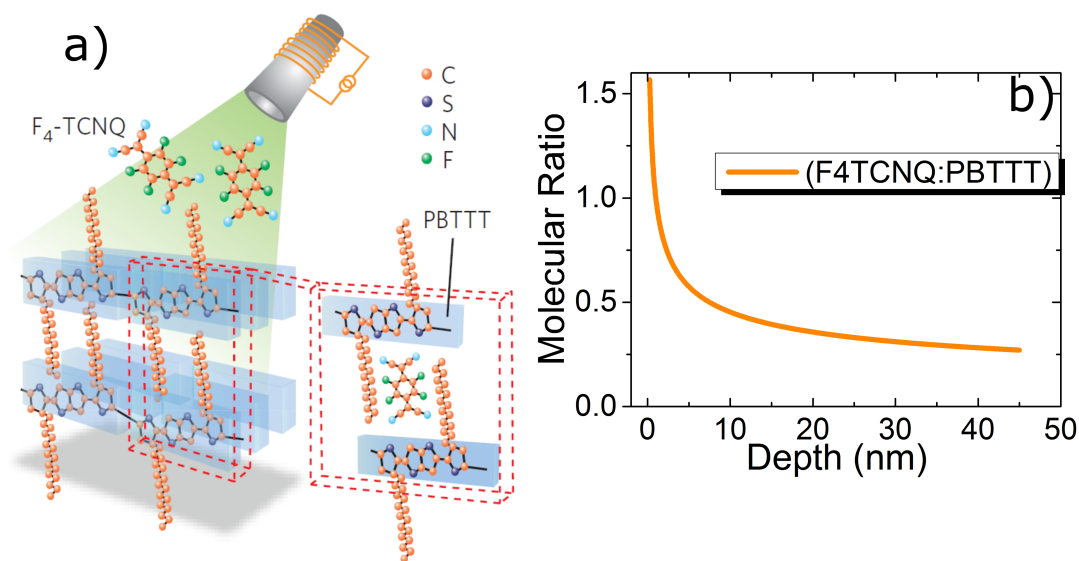
Figure 3.5 – (a) Schematic diagram of the evaporation doping method of F4TCNQ and resulting stacking of PBTTT and F4TCNQ molecules chain. (b) A curve represents the molecular ratio of F4TCNQ:PBTTT obtained from the XPS depth profile data. The schematic is adapted from [108] and the curve is plotted based on the experimental data reported in the same reference.

Efficiency of Dedoping Process for Tuning Conductivity and Dopant Ratio

In doped PBTTT, the conductivity and the dopant ratio can be tuned easily by dedoping as explained is section 2.10. In the dedoping process, the dopant content of the polymer is controlled by annealing the polymer in a sequence of steps. This process is efficient for tuning conductivity as assessed by ultraviolet-visible (UV-Vis) absorption spectroscopy. Figure 3.6a shows UV-Vis spectra performed for 100 nm PBTTT doped with evaporated F4TCNQ. The sample were dedoped at 100 ^{o}C in N_2 atmosphere at each dedoping step. The figure shows two distinct peaks at 555 nm (2.2 eV), which corresponds to the neutral absorption peak (the pristine PBTTT), and at 400 nm (3.1 eV) which corresponds to the dopant peak, F4TCNQ. As clearly shown in the spectra, the peak intensity at the dopant position decreases gradually during the dedoping process (8-steps dedoping) from its its maximum when the sample had its original dopant ratio until a small peak at the 8th dedoping step, indicating decreased dopant content. This gradual decrease in the dopant contents is associated with the gradual conductivity decay from 150 S.cm^{-1} for a fully-doped polymer to 0.34 S.cm^{-1} for a polymer at dedoping step 8 as shown in figure 3.6b. This plot contains the conductivity versus the relative absorbance at the peak 400nm which refer to the dopant contents . The additional two peaks that appear at 770 nm and 870 nm in figure 3.6a, are attributed to the presence of fully ionized singly charged F4-TCNQ anions on top of the broadband polaron absorption of PBTTT [108]. The information of the annealing steps performed for dedoping are listed in table 2.
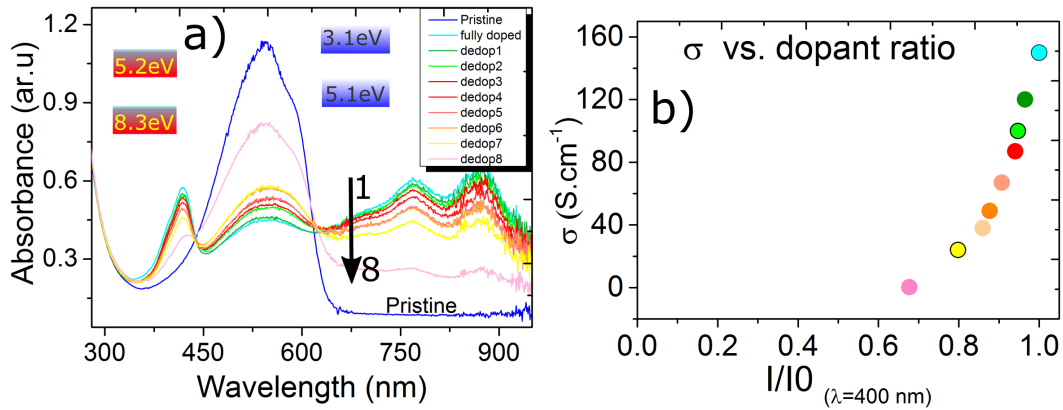
Figure 3.6 – Tuning conductivity and dopant ratio by dedoping process. (a) UV-Vis absorption spectrum performed for 100 nm PBTTT sample doped with F4TCNQ. The plot includes the spectrum of each dedoping step. (b) Conductivity measured at each dedoping step plotted versus the relative intensity at 400 nm. I0 represents the intensity of the fully doped step.

Table 2 – The information of post-annealing steps performed for dedoping PBTTT. Zero step refers to the fully doped poylmer

Annealing step	0	1	2	3	4	5	6	7	8
Annealing time (min)	-	20	20	20	40	44	70	345	12h
σ (S.cm^{-1})	150	120	100	87	67	49	38	24	0.34

3.1.4. Fabrication of the Electrodes and the Interfacial Layer

In addition to the three main materials composed the devices used in this work (YIG, PEDOT:PSS, and PBTTT), other materials also are used, namely, Pt, Ru, Au, and Al_2O_3. Pt and Ru are deposited either as electrodes for the samples prepared for ISHE measurements or as spin-sink full layers for some control samples. The deposition is done by magnetron sputtering for which the thickness is obtained by calibrating the growth rate using x-ray reflectometry. The electrodes are defined using shadow masks. For measuring ISHE in YIG/PBTTT samples, Au electrodes are used which are deposited by electron beam evaporation and defined on the samples using a shadow mask. On the other hand, for some devices an interfacial layer of ca. 30 nm Al_2O_3 was deposited on the YIG by electron beam evaporation. This layer is used in some control experiments to exclude the effect of spin pumping from YIG into the spin sink. The thickness of the oxide is measured directly while the deposition is running using a quartz microbalance integrated into the thermal evaporation device.

3.2. Characterization Setups and Instruments

This section will be devoted to reviewing the experimental setups and instruments used in both FMR and ISHE measurements which are the main pillars of the experiments presented in this thesis.

In both FMR and ISHE measurements, YIG is driven to the FMR by rf field generated by rf current transmitted through an antenna. For this purpose, a microstrip waveguide (MSWG) is used.

3.2.1. Microstrip Waveguide - MSWG

MSWG is one of the wide range planar waveguides used to transmit rf power from one port to the other. These waveguides can be used for transmitting rf power in wide range frequency in both MHz and GHz regimes. The general aspects of the MSWGs are shown in figure 3.7a, which shows a conductor with width w and thickness t printed on top of a grounded dielectric substrate of thickness d and relative permittivity ε_r.

Such a geometry provides us with a hybrid of TM-TE wave [11] and the (E,H) field lines distributing in the insulator region - between the stripline and the ground plane - and also in the air region as shown in figure 3.7b.

The MSWG used in our experiments has a characteristic impedance of 50 Ω and has a 250 μm wide transmission line with a thickness of 35 μm. The top-view image of this MSWG is shown in figure 3.7c. As shown here, the transmission line of the MSWG is located on the top of the WG where the rf power is transmitted. For FMR and ISHE measurements, the sample is placed in the middle of this transmission line.
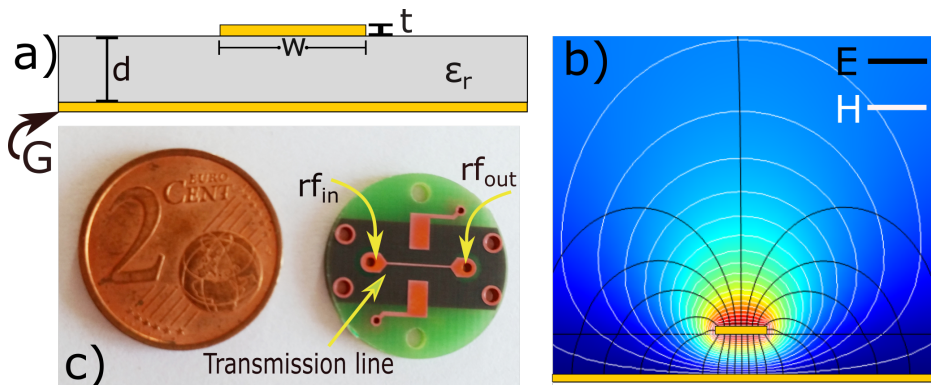
Figure 3.7 – Illustrations of the Microstrip waveguide (MSWG) used in FMR experiments. (a) A side-view schematic for the MSWG indicating the transmission strip line and the separating grounded dielectric layer. (b) Comsol dc simulation for the electric and magnetic field (E , B) lines distribution within the dielectric region and on top of the transmission line (COMSOL Multiphysics ®). (c) A top-view image for the MSWG used in our experiments illustrating the stripline and the input and output rf power.

[11]For the case of MSWG it is not possible to get a pure TEM wave because the phase velocity of TEM fields in the dielectric region would be c/ε_r, whereas the phase velocity of TEM fields in the air region would be c. So, it is impossible to fulfill the phase-matching boundary condition at the dielectric-air interface [140].

3.2.2. FMR Setup Configuration

For FMR measurements, the device under test (DUT) is placed face down on the stripline antenna. While an external homogeneous magnetic field (H_{ex}) fixes the magnetization of YIG parallel to the antenna, a radio-frequency (rf) current through the antenna is used to create an rf field (h_{rf}) which excites the ferromagnetic resonance in YIG. The spectrum is taken by sweeping the external field.

For FMR measurements, H_{ex} is modulated at a low amplitude and using low modulation frequencies, between(100-1000) Hz allowing for FMR measurements using a lock-in amplifier. More details regarding magnetic field modulation is here [141]. The magnetic field is modulated using two small coils attached to electromagnet poles. The resolution of the field control is around 0.05 Oe. The rf power is generated using a RHODE and SCHWARZ SMF100A Microwave Signal Generator. To determine the FMR amplitude, the absorption in the waveguide is measured using a high-pass filter connected to a Schottky diode whose signal is fed into a lock-in amplifier. The output signal of the lock-in amplifier is measured using an Agilent 34420A 7.5 digit nanovoltmeter. The microwave signal transmitted through the sample is measured as a function of the H_{ex} for the given frequency. The setup layout and the included devices and connection profiles are illustrated in figure 3.8.
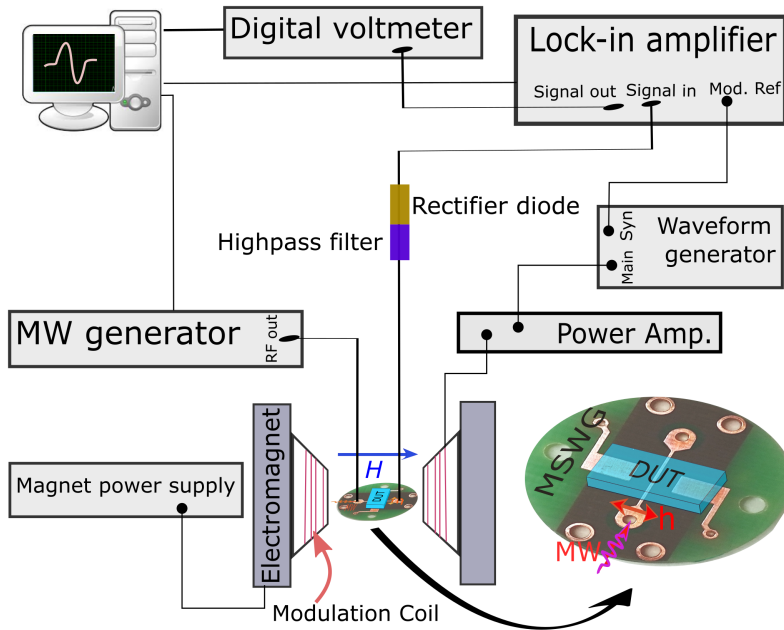
Figure 3.8 – Basic configuration of FMR setup used in spin pumping experiments. The figure illustrates the device under test (DUT) located on the MSWG and also all employed devices involved in the measurements.

The FMR signal obtained from rf absorption in the sample is proportional to the imaginary part of the microwave susceptibility $\chi^{''}$ shown in equation 2.23. However, because we add magnetic field modulation, the susceptibility $\chi(H)$ becomes $\chi(H + he^{i\omega t})$, where ω and h are the modulation frequency and magnetic field of the modulation coil, respectively [142]. Using Taylor expansion for the susceptibility with respect to time, the first two terms will be $\chi(H) + i\omega h e^{i\omega t}[\frac{d\chi}{dH}]$, and this is the
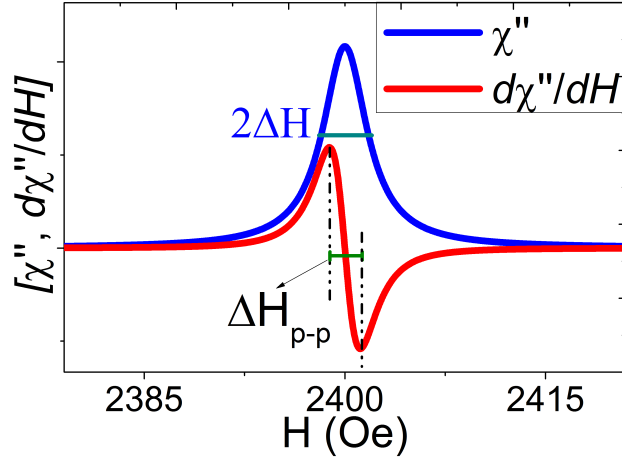
Figure 3.9 – Typical FMR spectrum indicating χ'' curve and also the $\frac{d\chi''}{dH}$ curve fed into Lock-in amplifier. ΔH_{p-p} which is estimated from the differential curve of χ'' obtained in experiments is indicated.

signal which is fed into the lock-in amplifier. Looking at this formula, the first term represents a dc term and it is filtered out. The second term represents an oscillatory signal with the same frequency as the field of modulation signal which is used a reference for the Lock-in amplifier. As a result of that, the second term which is the first derivative of the susceptibility will get into Lock-in amplifier. So, in FMR characterizations where the FMR spectrum is recorded using a Lock-in amplifier, the FMR parameters are extracted from the first-derivative susceptibility curve $\frac{d\chi''}{dH}$. The linewidth (HWHM) ΔH used for damping calculations is calculated from the peak-to-peak linewidth ΔH_{p-p} extracted from the differential curve. The ΔH is linked to ΔH_{p-p} by the relation

$$\Delta H = \frac{\sqrt{3}}{2}\Delta H_{p-p} \tag{3.1}$$

Both parameters are illustrated in the figure 3.9.

The damping is obtained by fitting the frequency dependence of the linewidth ΔH according to the equation $\Delta H = \alpha\frac{\omega}{\gamma} + \Delta H_0$, [section 2.3]. The value of the gyromagentic ratio $\frac{\gamma}{2\pi}$ is estimated by plotting the values of exciting frequency f as a function of the resonance field H_{FMR} and then fitting the plot to the Kittel equation

$$f = |\gamma|\sqrt{H_{FMR}[H_{FMR} + 4\pi M_{eff}]} \tag{3.2}$$

Figure 3.10a, shows the plotted data for 100nm YIG which are fitted according to Kittel formula, 3.2. The value obtained from the fit for γ is 2.8 MHz/Oe. The saturation magnetization $4\pi M_s$ is measured using SQUID magnetometry and found to be 1800 Oe, figure 3.10b.
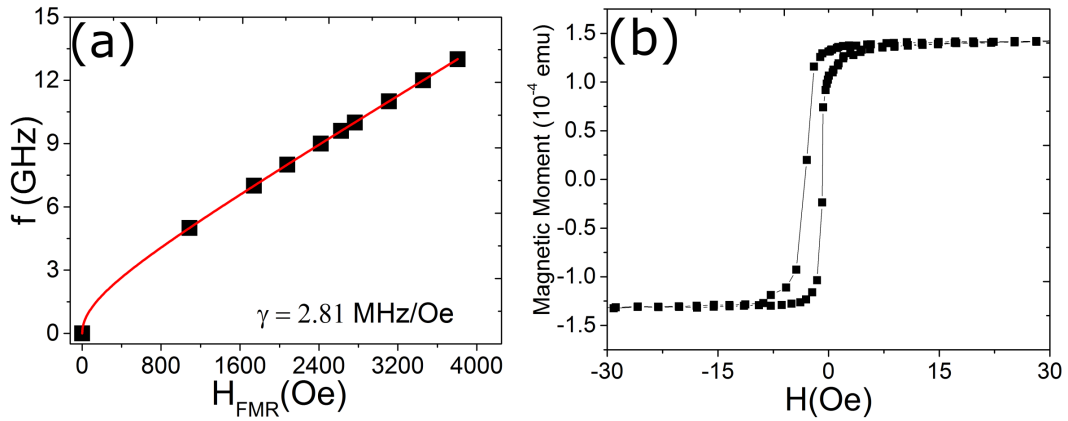
Figure 3.10 – Calculation of the gyromagnetic ratio γ and the saturation magnetization $4\pi M_s$ for 100nm LPE YIG. (a) H_{FMR} data plot as a function of the exciting rf frequency fitted due to Kittel equation, equation 3.2. (b) Hysteresis loop measured by SQUID magnetometery for the YIG film. This curve is obtained after subtracting the paramagnetic background of the GGG substrate. The sample size is $5.73 \times 1.74\ mm^2$.

3.2.3. ISHE Setup Configuration

Similar to FMR, ISHE measurements also are done by placing the device face down on a MSWG antenna with a transmission line thickness of $35\,\mu$m and width of $250\,\mu$m. ISHE is measured at the FMR which is excited by h_{rf} while the YIG magnetization is saturated by H_{ex} as explained in section 3.2.2.
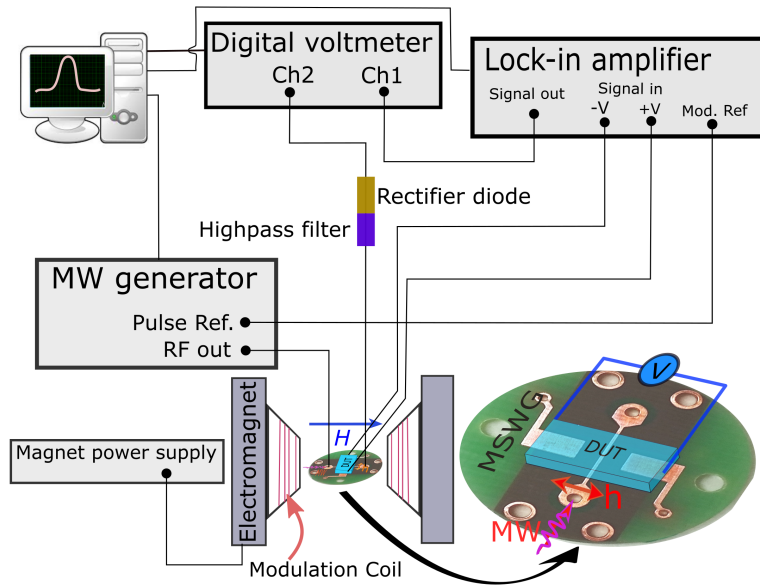
Figure 3.11 – Schematic of the ISHE measurement setup including all instruments used in the measurements.

The stripline is isolated with a thin layer of PMMA or polyimide to avoid any shorting between the antenna and the sample conducting layer. The rf amplitude

is measured using a high-pass filter, a diode, a Lock-In amplifier, and a Keysight 34420A nanovoltmeter. ISHE measurements are carried out using copper leads attached to the sample contacts (Pt, Ru, Au) with silver glue. For these measurements, the rf amplitude rather than the magnetic field is modulated. For amplitude modulation, we used modulation frequency f_{mod} of 500 kHz with a pulse period of $2\mu s$ and pulse width of $1\mu s$. The experimental setup used for ISHE measurements including all employed instruments is illustrated in figure 3.11.

Signal:Noise Optimization

ISHE is easily detectable when using high SOC NMs as spin sinks because of high spin-charge conversion efficiency.

However, in πCPs like PEDOT:PSS and PBTTT, the ISHE detection becomes a challenging task due to the small resulting signal (several tens of nV). The noise level is approximately equal to the signal level or even higher. On the other hand, increasing the rf excitation power rises the ISHE signal but also induces much noise. Furthermore, using high excitation power generates artifacts like thermovoltages. For these reasons, it is more reliable to measure the ISHE at low power than at high power. For these reasons, it was necessary to optimize the ISHE signal by treating the relatively high noise. This was achieved by applying many strategies:

• Instead of attaching the polymer directly to the voltmeter using the Cu leads, rectangular contact electrodes made of Pt, Ru or Au are defined at the edges of each sample. This prevents a Schottky barrier which may be formed at the contacts. A Schottky barrier creates high background noise and consequently adds a large voltage offset to the measurements. Performing ISHE measurements with low expected signal at high sensitivity with the Lock-in amplifier when a Schottky barrier exists is very difficult. Finally, using silver paste to attach the leads to these metals contacts reduces contact resistance as well.

• To detect clear and pure ISHE signal, one of the most influential sources, low frequency noise [143], must be treated. This includes the modulation frequency, so for simplicity we will call it $1/f_{mod}$ noise.

The main effective strategy for treating $1/f_{mod}$ noise is to use a high modulation frequency f_{mod} while modulating the rf amplitude. This is because $1/f_{mod}$ noise inversely scales with the f_{mod} and thus decreases significantly when high f_{mod} is used. To show the effect of the modulation frequency on the ISHE signal and noise, we performed a series of ISHE measurements on one of our samples (YIG/PBTTT) at different f_{mod}. The figures 3.12(a-f) show the ISHE measurements for YIG/PBTTT sample carried out by modulating the amplitude at f_{mod} : 1kHz, 10kHz, 50kHz, 100kHz, 200kHz and 500kHz.

It is obvious from these figures that the signal:noise increases rapidly with increasing f_{mod}. This can be shown more clearly in figures 3.12(g-h) which include the values of the signal and noise for each curve, which are extracted from the amplitude of the curves and the width of the noise in the curves, respectively. As shown in figures 3.12(g), while f_{mod} increases, the noise is suppressed and the signal purity improves. As a result, the signal amplitude grows higher than the noise amplitude, Fig. 3.12(h). The signal amplitude measured here is around 15 times bigger than

the noise width which is very significant for such an ISHE measured at this low voltage level,($\sim 20\,nV$).
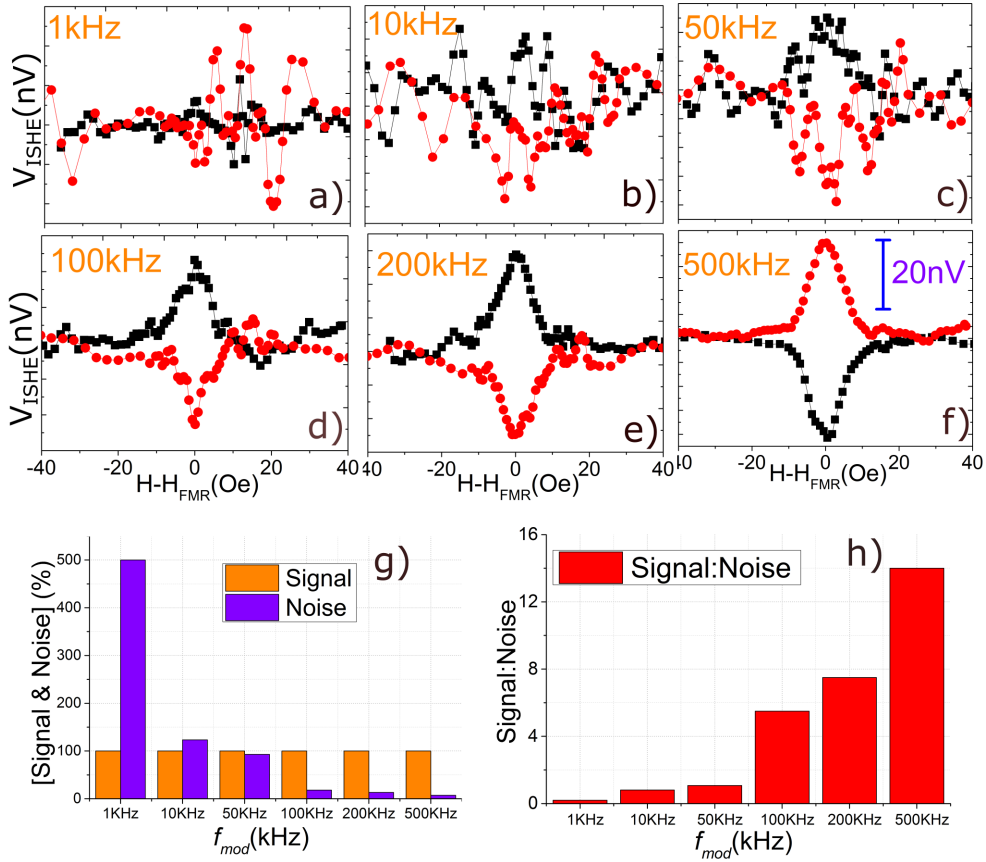
Figure 3.12 – Investigation of the $1/f_{mod}$ noise by studying the influence of the modulation frequency f_{mod} on the ISHE signal:noise ratio. (a-f) The ISHE curves measured for a YIG/PBTTT(25nm) sample at different f_{mod}. (g) The noise is suppressed with increasing f_{mod} for the frequency range between 1-500 KHz. (h) The purity of the ISHE-signal grows which is indicated by the rise of the signal:noise at the selected modulation frequencies. The optimal ISHE signal used for comparing the noise is measured at 500 kHz and shown in figure f. ISHE measurements were carried out at $h_{rf} = 9$ GHz, and $P_{rf} = 40$ mW (16 dBm).

Chapter 4

4. Radiation Damping in FMR Induced by a Conducting Spin Sink

4.1. Introduction

In this chapter [12], we investigate the damping in the FMR of YIG caused by spin pumping into adjacent conducting materials namely Pt and the conducting polymer PEDOT:PSS. By a systematic study which also includes multilayers in which the conducting layer is separated from the YIG by an insulator, we investigate the predominance of so-called radiation damping which originates from the interaction of the magnetic fields caused by the precessing magnetization with the conducting layer. Especially when PEDOT:PSS is used as a spin sink, this damping source becomes dominant and no contribution from the spin pumping can be identified. Based on the studies performed here, we demonstrate the validity and the limits of using the Gilbert damping as a measure of spin pumping in spin sinks materials including NMs and πCPs. To achieve all of that, we perform ferromagnetic resonance experiments on various structures based on YIG/PEDOT:PSS and YIG/Pt. Many steps and control experiments were performed to precisely investigate the resulting magnetic damping and its origins.

Spin pumping describes the flow of spin current into a spin sink. When the spin current flows into a material with sufficient SOC, it can be converted into a charge current by the ISHE. To investigate spin pumping, however, not only can ISHE be used, but also the damping in FMR can be used as a measure for spin pumping. This is because it is increased when spin current resulting from spin pumping flows into a material in which spin flip can take place, an effect which is often used for the quantification of spin pumping in literature [9–14, 20, 21].

---

[12]This study has been published in Ref. [8].

4.2. Magnetic Damping Origins in YIG/Spin-sink Bilayers

In fact, in addition to the intrinsic damping α_{in} and the damping contribution from spin-pumping α_{sp} [9–14, 18, 20, 21], other damping sources also can have a significant contribution to the overall damping, which may become dominant depending on the layers structure, sample and waveguide dimensions, and the experimental parameters and conditions. These damping sources include: eddy current damping α_{eddy}, radiative damping α_{rad}, and electromagnetic shielding damping α_{sh}.
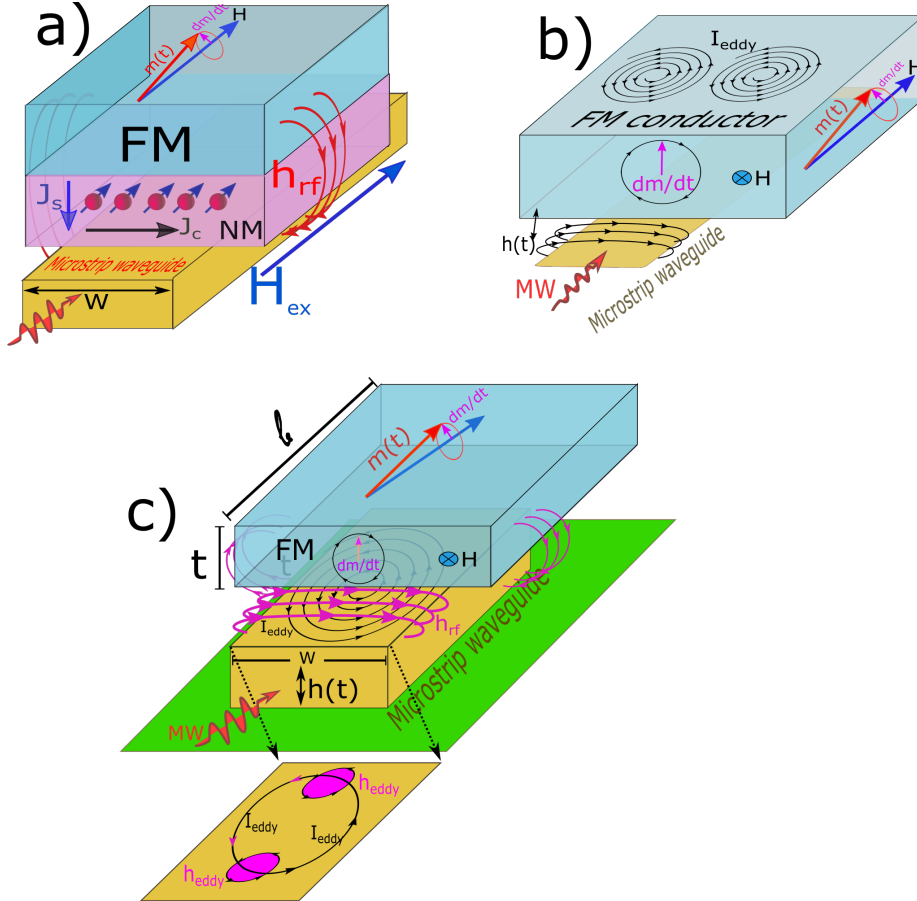
Figure 4.1 – The major origins of magnetic damping in FM/spin-sink bilayer systems. (a)α_{sp}. (b) α_{eddy}. (c) α_{rad}

Eddy current damping α_{eddy} refers to that originated from the eddy currents induced in conducting FMs, section 2.3. α_{eddy} only is effective in FM conductors and since all our devices are based on FM insulator YIG, so α_{eddy} will be skipped in our discussions [47–50].

Radiative damping α_{rad} is caused by the eddy currents I_{eddy} induced in the waveguide and it more strongly depends on the waveguide properties than the properties of the device under test [144–146].

Electromagnetic shielding damping α_{sh} is arises due to the shielding of the electrical and/or magnetic microwave fields along the MSWG caused by the conducting

film placed close to it. Although the shielding effect has the biggest influence on the FMR phase and amplitude, however, its effect on the waveguide impedance changes the radiation damping as well [147–149]. Illustrations of the damping sources which have a major contribution to the net damping are shown in figures 4.1(a-c).

4.3. Experimental Details

4.3.1. Samples Information

The work presented in this chapter is based on a sequence of control experiments employing different samples.

All samples are based on a series of layers based on 200 nm thick films of single-crystal YIG with dimensions $\sim 2 \times 5\ mm^2$ grown on GGG by liquid phase epitaxy (LPE). All samples are cut from the same YIG/GGG wafer and cleaned with organic solvents following the cleaning steps explained in appendix B. For the investigation of spin pumping, nine samples represent two sets prepared using two different materials as a spin sink. One set uses Pt full layer deposited by magnetron sputtering. Another set uses highly-doped PEDOT:PSS obtained from the commercial formulation in water (Clevios PH510, Heraeus), deposited and doped in the same way explained in section 3.1.2. The solution is spin-coated in the ambient atmosphere at 4000 r.p.m. for 1 min. The films are heated on a hot plate at 140 ^0C for 10 min. The nominal in-plane conductivity σ_{IP} of the material is 300 $S.cm^{-1}$, and the resulting PEDOT:PSS has an optimal thickness of 140 nm, and $\sigma_{IP} = 560\ S.cm^{-1}$. The thickness is measured using a DEKTAK surface profilometer. For control experiments, an additional Al_2O_3 interfacial layer with 30 nm thickness is deposited on some samples by electron beam evaporation. The layers and thicknesses of all nine samples are listed in table 3.

Table 3 – Samples used with materials and layer thicknesses

Sample	YIG (nm)	Al_2O_3 (nm)	Pt (nm)	PEDOT:PSS (nm)
S1:[YIG]	200	-	-	-
S2:[YIG/PEDOT:PSS]	200	-	-	140
S3:[YIG/Pt]	200	-	10	-
S4:[YIG/Al_2O_3]	200	30	-	-
S5:[YIG/Al_2O_3/PEDOT:PSS]	200	30	-	140
S6:[YIG/Al_2O_3/Pt]	200	30	5	-
S7:[YIG/Al_2O_3/Pt]	200	30	10	-
S8:[YIG/Al_2O_3/Pt]	200	30	15	-
S9:[YIG/Al_2O_3/Pt]	200	30	20	-

4.3.2. Experimental Setup

Magnetic Damping and Ferromagnetic Resonance

The original goal of the experiments was to determine the spin-mixing conductance for YIG/PEDOT:PSS by measuring the difference in FMR damping for pure YIG and a YIG/PEDOT:PSS bilayer. Special emphasis was to be put on the identification of artifacts because a low spin mixing conductance is to be expected for the polymer. This is due to dependence of the effective spin mixing conductance on the SDL and spin-flip rate, equation 2.50. In low spin-flip rate materials like polymers, this results in additional factors reducing the spin mixing conductance as illustrated in this equation and hence suppressing the spin pumping. To check the validity of the experiments a comparison with YIG/Pt should be done. For the various experiments, the FMR is measured for all samples and the damping enhancement with respect to pure YIG is extracted from the spectra. For the FMR measurements, the samples are placed face down on a strip-line antenna. While an external homogeneous magnetic field H_{ex} fixes the magnetization of the YIG parallel to the antenna, a radio frequency (RF) current through the antenna is used to create an rf field h_{rf} which excites the ferromagnetic resonance in the YIG, Fig.4.1a. The spectrum is taken by varying the external field at constant frequency. The FMR measurement configuration is illustrated in figure 3.8.
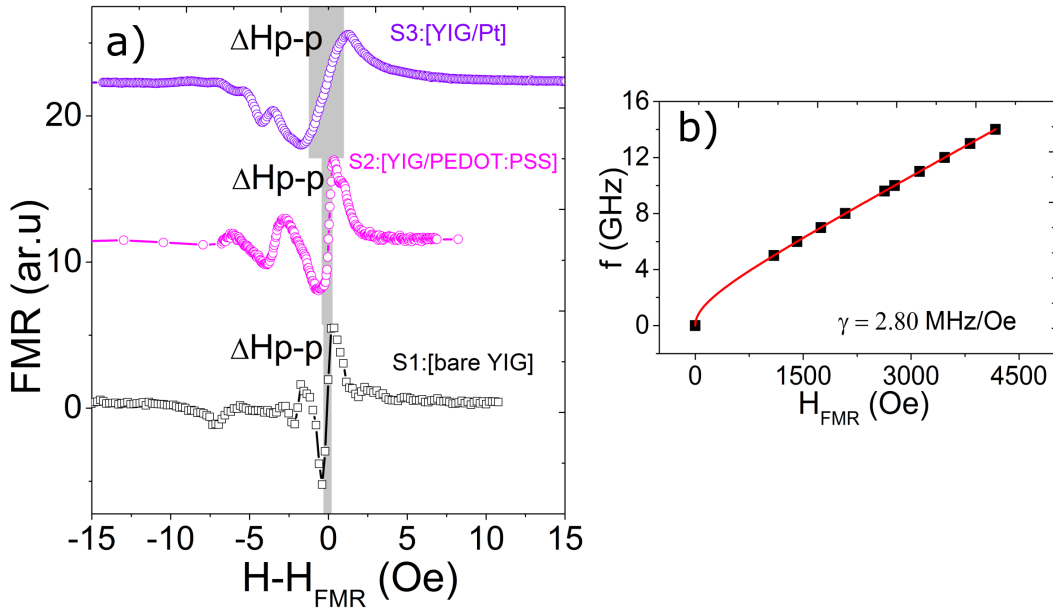
Figure 4.2 – (a) FMR curves and linewidth obtained at 8 GHz for S1, S2, and S3. (b) The H_{FMR} values extracted from FMR spectrum of bare YIG (200nm) at different rf frequencies. The data are fitted with Kittel equation for the in-plane geometry, equation 3.2.

The magnetic field resolution applied here is around 0.05 Oe. H_{ex} is modulated at small amplitude ($\sim$ 0.1 Oe) at a frequency of (184 Hz) allows for FMR measurements using a lock-in amplifier. All information of the RF signal generation and detection are explained in detail in section 3.2.2. As explained there, due to

the lock-in measurement the measured signal represents not the absorption signal but its derivative. The relative excitation power in these experiments is kept in the range between (-1 dBm) and (-10 dBm).

Gilbert damping α is obtained using the FMR linewidth frequency dependence (ΔH - f) of the uniform mode using the linear equation $\Delta H = \alpha \frac{f}{|\gamma|} + \Delta H_0$, where ΔH_0 is the intrinsic linewidth (inhomogenious broadening),[section 2.3].

ΔH which refers to the half width at half maximum (HWHM) is calculated from ΔH_{p-p} using the formula $\Delta H = \frac{\sqrt{3}}{2} \Delta H_{p-p}$.

The gyromagnetic ratio used here for our calculations is obtained by fitting FMR spectrum data at the resonance (H_{FMR}) to Kittel equation for the in-plane geometry [Eq. 3.2]. This is shown in figure 4.2b. The value obtained from the fit is γ = 2.8 MHz/Oe which is equivalent to that reported in literature [150, 151]. The magnitudes of the effective saturation magnetization $4\pi M_{eff}$ and γ extracted from Kittel equation fit for all samples are listed in appendix A.

Inverse Spin Hall Effect Measurements

For ISHE measurements, copper leads are attached as voltage electrodes on both ends of the sample using silver glue. The stripline antenna is isolated from the sample using a thin layer of polyimide. The experimental setup employed for ISHE measurements is illustrated figure 3.11.

4.4. Results and Discussion

4.4.1. Spin Pumping and Magnetic Damping

First the damping and its enhancement by spin pumping are investigated on three samples, one reference sample S1 and two samples covered by a spin sink material namely S2 and S3. Figure 4.2a, shows the FMR signals for YIG, YIG/Pt and YIG/PEDOT:PSS at 8 GHz. The gray area indicates the peak-to-peak linewidth. The increased linewidth for sample S2 and S3 indicates an increased damping. By fitting the multiple lines of the resonance spectra using Lorentzian line shapes, the linewidths and H_{FMR} are obtained, Fig. 4.3a. The resonance peaks are defined according to the uniform mode position which is confirmed by fitting the resonance field H_{FMR} using the Kittel formula for the in-plane geometry, Eq. 3.2. The fitting plots due to Kittel equation of all devices used in this chapter and the extracted parameters are included in appendix A.
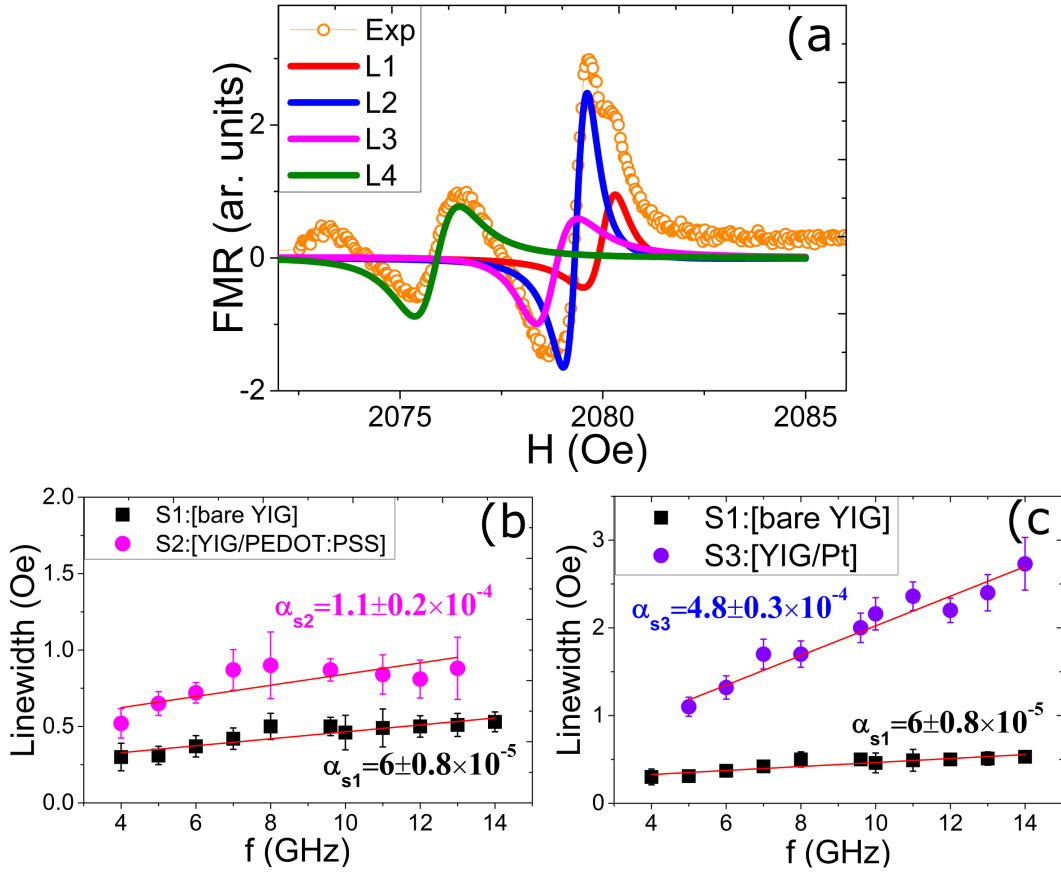
Figure 4.3 – (a) FMR curves showing the multiple lines in the spectrum for S2:[YIG-PEDOT:PSS]. The spectrum is taken with in-plane magnetic field at a frequency of 8 GHz. The solid lines are fitted to Lorentzian line shapes. (b-c) FMR linewidth as a function of the resonance frequency. The damping value for S1, S2, and S3 are determined from the slope of the linear fit. The errors for the damping values are estimated from the standard error resulting from the linear fit. The errors for the linewidth values are estimated considering both the magnetic field modulation 0.1 Oe and also the deviation of the FMR Lorentz fit from the experimental data.

Using the linear fit of the $\Delta H - f$ relation, and the extracted γ value, we obtain $\alpha = 6 \pm 0.8 \times 10^{-5}$ for the bare YIG, $\alpha = 4.8 \pm 0.3 \times 10^{-4}$ for YIG/Pt, and $\alpha = 1.1 \pm 0.2 \times 10^{-4}$ for YIG/PEDOT:PSS [Figs. 4.3b,c]. The damping enhancement is $(\Delta\alpha = 5 \pm 0.8 \times 10^{-5})$ and $(\Delta\alpha = 4.2 \pm 0.8 \times 10^{-4})$ for YIG-PEDOT:PSS and YIG-Pt, respectively. This seems to be a strong indicator for spin pumping.

4.4.2. Magnetic Damping Control Experiments

As mentioned above, enhanced damping can also have other origins. The net damping for FM/conductor includes contribution of all damping parameters

$$\alpha_{net} = \alpha_{in} + \alpha_{sp} + \alpha_{eddy} + \alpha_{rad} + \alpha_{sh} \tag{4.1}$$

This equation shows all damping contributions in a FM/conductor bilayer reported in literature. However, these contributions only occur under certain circumstances related to the properties of magnetic materials, waveguides, spin sink, and experimental conditions. The strategy followed in our control experiments is to study every damping source individually by simultaneously excluding the other sources. For this purpose a series of control experiments are done on additional YIG based multilayers. These include the following samples: S4, S5 and S7. Sample S4 is intended to exclude any additional damping by the Al_2O_3 layer itself. Another group of samples is prepared to study the damping change with Pt thickness (5, 10, 15, 20 nm) when an Al_2O_3 layer blocks the spin pumping. These samples are S6, S7, S8, and S9.

In samples S4, S5, and S7 the non-magnetic and insulating Al_2O_3 layer prevents any spin injection from the YIG into the non-magnetic film. By blocking the spin current at the YIG/(NM,πCP) interface we eliminate α_{sp}. So, the only damping enhancement in our YIG/Al_2O_3/(Pt,πCP) will be due to the other damping effects which will be discussed later.

Before studying the enhanced damping in the YIG/Al_2O_3/(NM,πCP) trilayers, we first test in sample S4 whether the YIG/Al_2O_3 interface alone causes any additional damping. Figure 4.4a shows damping curves for sample S1 and S4. Obviously the Al_2O_3 has no detectable influence on the damping. Although there is a nominal increase in damping it is only by approx. 10% and may well be related to small differences in the fit of the resonance lines and error bars. In a next control experiment we check whether the Al_2O_3 layer indeed blocks the spin pumping by investigating the ISHE in sample S7. Figure 4.4b shows the inverse spin Hall effect (ISHE) for S7 in comparison to sample S3. On the scale of the ISHE signal of sample S3 the plot clearly shows zero ISHE voltage and even for higher measurement sensitivity no ISHE signal can be detected for sample S7. The Al_2O_3 layer thus efficiently suppresses any spin pumping. As a consequence any enhanced damping in samples S5 and S7 must have a different origin. Figure 4.4c shows the dependence of linewidth on frequency for samples S1, S2, and S5, respectively. Both samples with PEDOT:PSS show an identical increase in damping within the error bars. The inserted Al_2O_3 layer does not seem to have any influence. Nevertheless, the increase in damping is significant, approx. ($\Delta\alpha = 5 \pm 0.8 \times 10^{-5}$).

Figure 4.4d shows the linewidth/frequency dependence for samples S1, S3, and S7. Here we find that for the YIG/ Al_2O_3/Pt sample the damping is also increased by ($\Delta\alpha = 8 \pm 0.8 \times 10^{-5}$) with respect to bare YIG, a value comparable to S5. In contrast to the samples with PEDOT:PSS, however, the damping increase is much lower than for the direct YIG/Pt interface of sample S3. So, as a first result even without spin pumping we find a considerable increase in damping as soon as a

conducting layer is placed on the sample.

As shown in Eq.4.1 there are five possible contributions to the damping in FMR, α_{in} (intrinsic), α_{sp} (spin pumping), α_{eddy} (eddy currents), α_{rad} (radiative), and α_{sh} (shielding). The Gilbert damping constants considered here are α_{in} , α_{sp} , α_{rad}, and α_{sh}, while α_{eddy} is neglected. Eddy current damping α_{eddy} results from the eddy current I_{eddy} generated in a conducting ferromagnetic material which is induced as a result of the magnetization precession. It depends on the conductivity of the FM, so it is negligible in magnetic insulators [47–50].
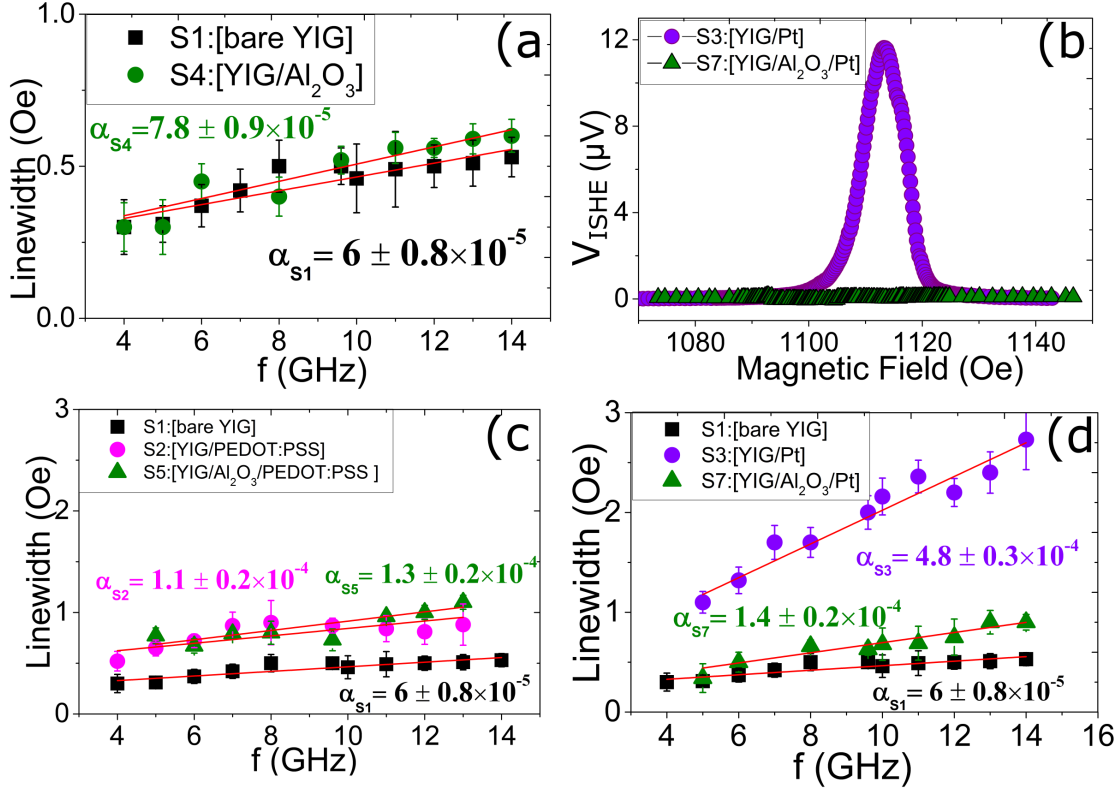
Figure 4.4 – Test of the suppression of the spin pumping by an Al_2O_3 interlayer. (a) An Al_2O_3 layer alone does not modify the damping of a single YIG film beyond the error bars. (b) In a YIG/Al_2O_3/Pt trilayer the ISHE is completely suppressed compared to a YIG/Pt bilayer. (c) Linewidth vs. frequency plotted for pure YIG, YIG/PEDOT:PSS, and YIG/Al_2O_3/PEDOT:PSS. The damping enhancement due to the PEDOT:PSS is significant, however, it is identical within the error bars with and without the insulating interlayer, respectively. (d) For the YIG/Al_2O_3/Pt also an additional damping is observed. Nevertheless, it is significantly smaller than without the Al_2O_3 interlayer.

4.4.3. Radiation Damping α_{rad} and Electromagnetic Shielding α_{sh}

Radiation damping α_{sh} is caused by the eddy currents induced in the waveguide or in the metallic film [144–146]. As stated in [146] waveguide and sample are designed for efficient excitation which in turn also means that the magnetization precession induces currents in the waveguide which lead to the increased damping. Unlike α_{eddy}, radiative damping depends on the properties and dimensions of the waveguide and the sample, so it is relevant for both ferromagnetic insulators and conductors. The damping contribution due to the radiation is given by

$$\alpha_{rad} = \frac{\mu_0^2 M_s \gamma \eta t \ell}{2 Z_0 W} \tag{4.2}$$

Where Z_0 and W are the conductor impedance and width, respectively, ℓ is the sample length, γ is the gyromagnetic ratio, and η is a dimensionless parameter that accounts for the mode profile in the sample [146]. It should be noted that the spacing between the waveguide and the sample also plays an important role. The radiative damping is decreased with increased spacing between waveguide and sample.
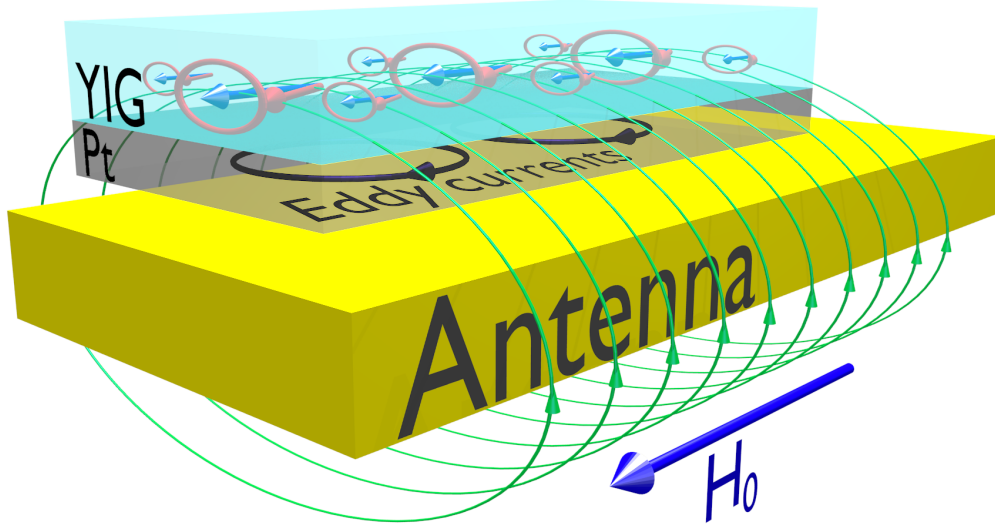
Figure 4.5 – Schematic diagram for measurement geometry during the FMR experiment. The RF field induced by the Antenna causes an inhomogeneous precession in the YIG film. This precession induces Eddy currents in the Pt layer which is located between antenna and YIG. While the Eddy currents induced by the antenna only reduce the amplitude of the signal, the Eddy currents induced by the precession can cause additional damping and an increase in linewidth.

Especially in ferromagnets with very low damping, the contribution of radiation damping can become significant [152]. Because the effect is based on the coupling between waveguide and ferromagnet, it also contributes when we measure the damping of the pure YIG layer. So its magnitude must be smaller than the measured damping of $\alpha = 6 \pm 0.8 \times 10^{-5}$ and it can only be the cause of our findings if this

coupling changes from sample to sample. We thus need to understand the influence of a thin conducting layer between ferromagnet and waveguide on the damping. Some publications also discuss the so called electromagnetic shielding [147–149]. For example Bailleul *et al.* calculate that the presence of a thin conducting layer of sub-skin-depth thickness between waveguide and ferromagnet can effectively shield the magnetic and electric fields and change the impedance of the waveguide [147]. A shielding of the field alone cannot increase the damping but will just decrease the amplitude. Nevertheless, a change of impedance can change the radiation damping as described in Eq.4.2.

Our experimental findings can be explained by taking into account the interplay of radiation damping and the conducting layer which is used as a spin sink and which is in direct contact to the ferromagnet. Schoen *et al.* demonstrate that the spacing between the waveguide and the ferromagnet has a strong influence on the radiation damping [146]. For example from direct contact between waveguide and ferromagnet to a spacing of 200 μm the radiation damping is decreased by two orders of magnitude. In our case the spacing between waveguide and ferromagnet is determined by the polyimide layer on the waveguide which has a thickness of tens of microns. However, when the conducting Pt or PEDOT:PSS spin-sink layer is inserted, it is in direct contact to the ferromagnet and hence reduces the spacing between the FM and the conducting layer to zero. It can thus cause radiation damping by the eddy currents induced in the conducting layer by the inhomogeneous precession in the YIG, Fig.4.5. While for the pure YIG layer and large spacing, the radiation damping must be smaller than 6×10^{-5} an increase of only one order of magnitude in case of the spin pumping samples is enough to explain our findings and is in agreement with the results of Schoen *et al.* Also, our control samples with an Al_2O_3 interlayer fit this picture because the thickness of the Al_2O_3 is only 30 nm.

In this case, a radiation damping almost as large as for zero spacing can be expected. Furthermore, the different results for PEDOT:PSS and Pt are well in line with the theory of radiation damping. The resistance of the PEDOT:PSS layer (120 Ω) is approx. two times higher than the one of the Pt (55 Ω). As a result also the induced eddy currents and the related radiation damping are higher for the Pt covered YIG than for the sample with PEDOT:PSS. From the measurements with the Al_2O_3 interlayer [Figs. 4.4c and 4.4d] we can determine the radiation damping by coupling to the conducting layer as the difference between the net damping and the damping in the bare YIG layer. For the Pt we obtain a value of $\Delta\alpha = 8 \times 10^{-5}$ and for the PEDOT:PSS $\Delta\alpha = 5 \times 10^{-5}$. It is noteworthy that these values are so small that they can barely be determined when using a metallic ferromagnet which often has a damping much higher than this. Only for the YIG layer which exhibits a very low initial damping these values can be measured accurately.

4.4.4. The Net Damping by Spin Pumping

So, in additional to the damping contribution by spin pumping α_{sp}, any further damping enhancement for our ferromagnet/conductor stack can most likely be attributed to radiation damping α_{rad}.

If we want to determine the spin-pumping we thus need to measure the difference in damping between the samples with YIG/Pt or YIG/PEDOT:PSS and the reference samples YIG/Al_2O_3/Pt and YIG/Al_2O_3/PEDOT:PSS respectively [Figs. 4.4c and 4.4d]. For the Pt we find a difference of $\alpha = 3.4 \pm 0.4 \times 10^{-4}$. For the PEDOT:PSS, however, there is no difference within the error bars. As a consequence we can conclude that any damping by spin pumping is extremely small and completely obscured by the radiation damping for PEDOT:PSS. Because the additional damping associated with α_{rad} is caused by the current induced in the conducting layer capping the FM insulator, the damping must also depend on the resistance of the conducting layer. To investigate this issue we have fabricated a sequence of samples (S6 - S9) consisting of YIG/Al_2O_3/Pt(x) trilayers with different Pt thicknesses x (x= 5, 10, 15, 20) nm.

Figures 4.6(a-d) show the frequency-dependent FMR linewidth for the different stacks of the sequence (S6 - S9).

The damping curves of all YIG/Pt sample series including those with Al_2O_3 interlayer and also the bare YIG reference sample are shown in figure 4.6e. From this figure, the effect of the radiation damping and its magnitude between the intrinsic damping region (bare YIG), and the dominant spin pumping region (YIG/Pt) is clearly shown.

Figure 4.6f shows the pure radiation damping α_{rad} for the sample series S6 - S9 obtained by measuring the total damping and subtracting the Gilbert damping of the single YIG layer.

Except for sample S7 which shows an unexpectedly low damping we observe a constant increase of damping with Pt thickness. We have also checked the sample resistances and they scale inversely with Pt layer thickness. Table 4 shows the measured values for the damping and Pt resistance.
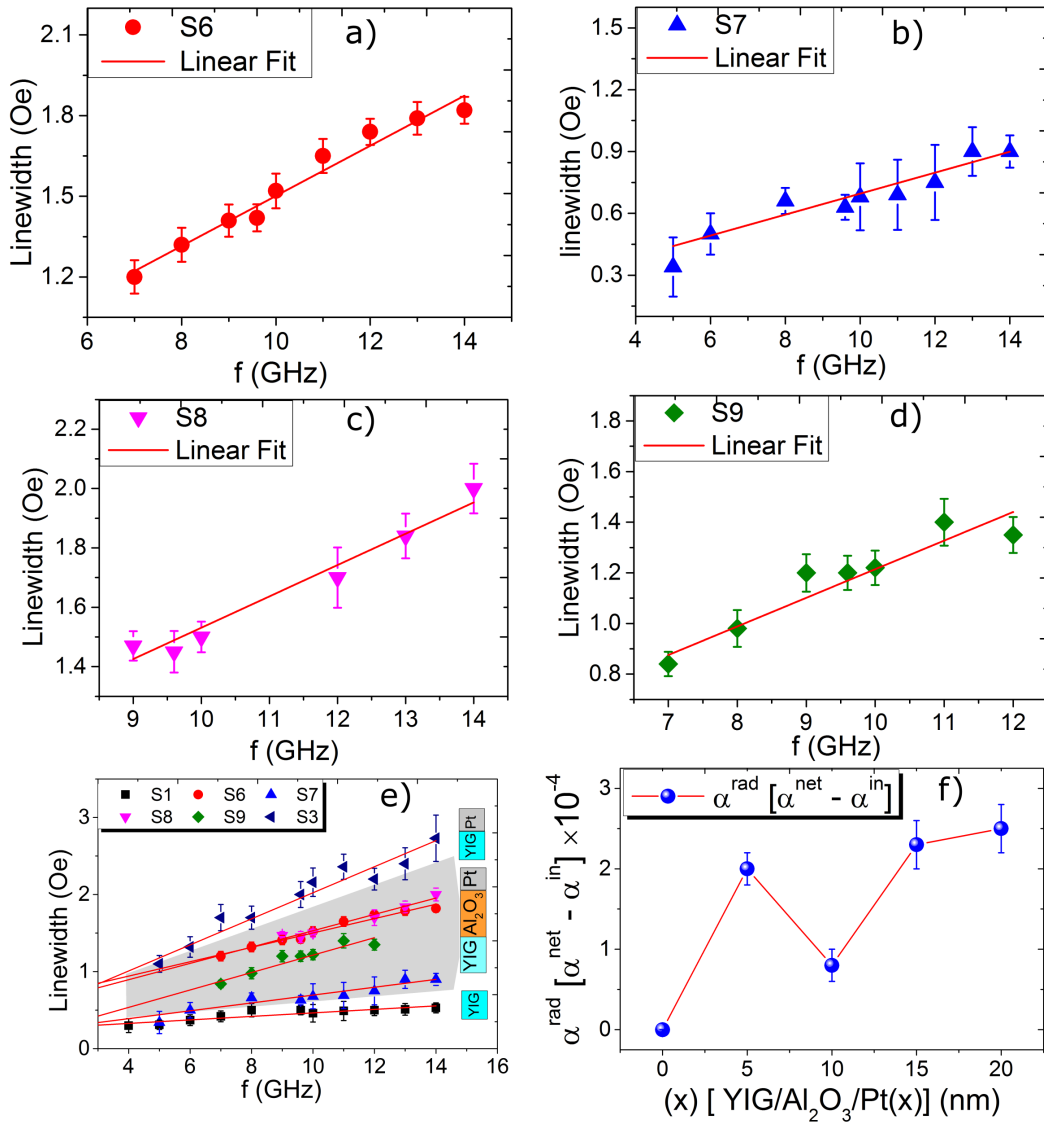
Figure 4.6 – Linewidth versus frequency plotted for the sample sequence (S1, S6, S7, S8, S9, and S3). (a-d) The individual carves illustrating the errors and the linewidth range for samples (S6-S9). (e) The plots of all Pt-based control samples and the bare YIG reference sample. (f) The extracted radiation damping as a function of Pt thickness for the samples with 30 nm of Al_2O_3 between YIG and Pt.

Table 4 – Total damping α obtained experimentally for the YIG/Pt samples with and without Al_2O_3.

Sample	YIG/Al_2O_3(30 nm) /Pt(x),x(nm)	Al_2O_3(nm)- Pt (nm)	Damping α	$R_{Pt}(\Omega)$
S1	YIG	0-0	$6.0 \pm 0.8 \times 10^{-5}$	-
S6	YIG/Al_2O_3/Pt	30 - 5	$2.6 \pm 0.2 \times 10^{-4}$	200
S7	YIG/Al_2O_3/Pt	30 - 10	$1.4 \pm 0.2 \times 10^{-4}$	102
S8	YIG/Al_2O_3/Pt	30 - 15	$2.9 \pm 0.2 \times 10^{-4}$	91
S9	YIG/Al_2O_3/Pt	30 - 20	$3.1 \pm 0.3 \times 10^{-4}$	35
S3	YIG/Pt	0 - 10	$4.8 \pm 0.3 \times 10^{-4}$	55

This contribution to the overall damping must also be considered when the results of spin pumping experiments are used to calculate the spin mixing conductance [9–14, 18, 20, 21]. In the case of YIG/Pt the approximation of a spin diffusion length in the Pt smaller than the Pt thickness can be used and the spin mixing conductance can be calculated as explained in section 2.4.2 as follows:

$$g^{\uparrow\downarrow} = \frac{4\pi M_s d_F}{g\mu_B}\alpha_{sp} \tag{4.3}$$

Using $d_{YIG} = 200$ nm , $4\pi M_s = 1531$ Oe, $g = 2.02$ [153], and $\mu_B = 9.27 \times 10^{-21}erg/G$ [33], the resulting $g^{\uparrow\downarrow}$ is $6.8 \pm 0.8 \times 10^{18}m^{-2}$ if we do not correct for radiation damping. If however, we additionally consider a contribution by the radiation damping as measured with the Al_2O_3 interlayer the calculation yields $5.4 \pm 0.6 \times 10^{18}m^{-2}$ which is a significant correction well beyond the error bars. It should be noted that, both results are in the range of values reported in the literature [9–14, 18, 20, 21, 46]. Our calculations show that, even in systems with significant spin pumping, radiation damping can cause a large error. The influence of radiation damping has been reported in the literature, however, it was only considered as a correction for the intrinsic damping in the ferromagnet [146]. Its importance for spin pumping experiments has not been mentioned in the past. The fact that with and without correction by radiation damping our spin mixing conductance for YIG/Pt lies within the values previously published by others [9–14, 18, 20, 21, 46] might be one additional reason for the deviations between different experiments.

For the polymer the situation is different. There the additional damping as measured ($\Delta\alpha \simeq (0.5 \pm 0.2) \times 10^{-4}$) would result in a spin mixing conductance of $g^{\uparrow\downarrow} = 8.0 \pm 3.2 \times 10^{17}m^{-2}$ if the approximation mentioned above was used. Most likely, however, the spin diffusion length in the PEDOT:PSS is larger than the PEDOT:PSS thickness [27] and a more complex formula needs to be applied [equation 2.50], which would also necessitate measurements for different polymer thicknesses [10, 56]. As we show below, however, the extraction of the spin mixing conductance is pointless. After correction for the radiation damping, no additional damping is left within the error bars. It should, however, be noted that the negligible increase in damping for the YIG/PEDOT:PSS interface does not mean that no spin pump-

ing takes place. Most likely spins are injected into the PEDOT:PSS creating a spin accumulation, however, due to the low spin flip rate/long spin diffusion length [27], the backflow is equally high. This way the steady state spin current out of the ferromagnet which is the cause of the additional damping remains extremely small. In this case no comparison with past experiments is possible because no damping experiments have been reported for YIG/PEDOT:PSS.

From these results we must conclude that the spin mixing conductance has to be calculated as:

$$g^{\uparrow\downarrow} = \frac{4\pi M_s d_F}{g\mu_B}(\alpha_{NM} - \alpha_{FM} - \alpha_{rad}) \qquad (4.4)$$

where, α_{NM}, α_{FM}, and α_{rad} are the damping as measured for the combination of ferromagnet and spin sink, the intrinsic damping for the FM only, and the radiation damping, respectively.

Finally, the fact that for PEDOT:PSS we find mainly dominance of radiation damping and no indication of spin pumping beyond the error margins is in agreement with the low SOC expected from this polymer. This means, if there is spin pumping it will be very small and therefore the resulting ISHE signal will be small as well. Such a small ISHE will need a systematic and precise measuring strategy like this performed here for studying radiation damping in YIG/PEDOT:PSS. For this purpose, an intensive and systematic study is performed which will be included in the next chapter.

4.5. Summary

In this chapter, we investigate the radiation damping in the FMR of YIG caused by spin pumping into Pt and πCP PEDOT:PSS spin sink.

Our results show that when ferromagnetic layers with very low damping are used for spin pumping experiments, radiation damping may be a major part of the total damping. In spin pumping experiments, the conducting spin sink which is deposited on the ferromagnet's surface adds damping just by eddy currents which are induced due to inhomogeneous precession in the ferromagnet. Especially when a spin sink with low spin scattering (like organic materials) and thus low damping enhancement is investigated the radiation damping can yield results which are bigger than any damping stemming from the spin pumping itself. Because the radiation damping is difficult to estimate, it is necessary to perform experiments on reference samples with non-conducting interlayers which inhibit the spin-pumping. These allow to measure the radiation damping directly which can then be used to correct the values obtained for the spin-pumping samples without interlayer.

Chapter 5

5. Quantifying the ISHE in Highly-doped πCP PEDOT:PSS

5.1. Introduction

In this chapter [13], we present a systematic investigation of the ISHE in πCP PE-DOT:PSS. Using a number of reference experiments, we are able to identify and to isolate side effects which obscure the small but finite inverse spin-Hall effect in the polymer. Using a sample geometry in which the contact areas and the area of spin current injection are laterally separated we are able to distinguish the ISHE from thermovoltages induced by non-reciprocal MSSW and from the ISHE induced by spin pumping through the polymer into the contacts. With an additional control experiment, we can even quantify the Nernst effect which also needs to be taken into account. With these results, we can unambiguously show that the ISHE is present in this material, however, at a level which requires a dedicated sample design and careful consideration of various artifacts.

The presence or absence of the ISHE generated in YIG/PEDOT:PSS bilayer systems has been investigated in the past with contradicting results. In Ref. [27] Ando *et al.* claimed an effect similar in magnitude to that of YIG/Pt. In Ref. [91] our group already indicated that the so-called spin wave heat conveyor effect which can create a temperature gradient in a typical measurement geometry for the inverse spin Hall effect may result in thermovoltages indistinguishable in signature from the ISH voltage, even when thin film YIG is used. In 2018 finally, Wang *et al.* [28] showed that indeed the thermovoltages which appear in a sample geometry similar to that in Ref. [27] are dominating and as a result claimed that there either is no ISHE in YIG/PEDOT:PSS or that it is below their detection limit because of the strong effects of asymmetric sample heating. As we will show it is possible to avoid the mentioned effect by using a suitable sample design. Nevertheless, we also find that further side effects need to be investigated and quantify to identify the small but finite ISHE in PEDOT:PSS.

---

[13]The study has been submitted for publication.

5.2. On the Voltage Origins in πCPs Spin Sink

ISHE mechanisms is used to study the spin to charge conversion by detecting the pure spin currents $\vec{J_s}$ injected from an FM into a spin sink which in most cases is non-magnetic NM. As shown in figure 5.1, the ISHE is detected as a dc voltage (or charge current $\vec{J_c}$) in the direction perpendicular to $\vec{J_s}$ and the spin polarization vector $\vec{\sigma}$, respectively, whose direction in the case of saturation is denoted by the external magnetic field $\vec{H}$. The relation between $\vec{J_c}$ and $\vec{J_s}$ is defined by the vector product $\vec{J_c} = \frac{2e}{\hbar}\theta_{SH}[\vec{J_s} \times \vec{\sigma}]$. According to the $\vec{J_s}$-$\vec{J_c}$ conversion (section 2.5.3), V_{ISHE} in the spin sink in contact to the FM is calculated using the equation 2.61.
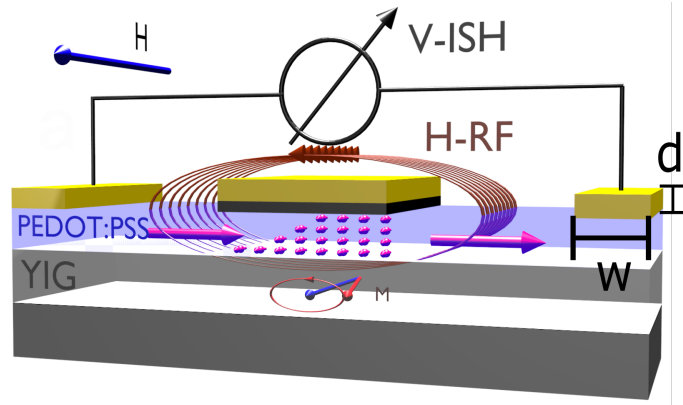
Figure 5.1 – The typical ISHE measurement configuration illustrating the rf current applied using MSWG, and the direction of the applied H with respect to the measured ISHE voltage.

In contrast to the ISHE in metals with large SOC (e.g., Pt, Ta), ISHE in πCPs with large spin diffusion length (SDL) [27, 105] and high Seebeck coefficient [28, 93] requires special attention to side effects. From [Ref. [8]], and the study in the previous chapter, it is clear that any ISHE in this material system, if existent, must be small compared to the signals measured by [Ref. [27]]. So any attempt to measure the ISHE must take into account all physics which may cause a signal with a signature similar to that of the ISHE.

Indeed there are a number of artifacts which can appear in the typical detection geometry for the ISHE. Only one example are non-reciprocal magnetostatic surface spin waves (MSSW) or Damon-Eshbach modes (DEM) (see section 2.6). Following the ferromagnetic resonance intensity, these spin waves generate a lateral temperature gradient resulting in a thermovoltage in the polymer-metal contacts which are at different respective temperatures. This case is shown in figure 5.2a. Because of the properties of DEM, this gradient is reversed for the opposite direction of the external magnetic field, and the resulting thermovoltage is virtually indistinguishable from the ISHE. Especially for PEDOT:PSS the effect can be quite severe because of the large Seebeck coefficient [93]. In this case, the ISHE can only be determined by either measuring and subtracting the thermovoltage in a reference experiment or by using a special geometry which we describe later. Also in many samples, the spin source under the organic film overlaps with the metal contacts on top of the

film. In this case, it is possible that a spin current flows through the polymer into the metal contacts and causes an additional ISHE there (Fig. 5.2a). This effect is normally discarded by using a contact material with negligible ISHE. It should be noted, however, that an ISHE negligible in one experiment may become sizeable when the detection sensitivity is increased by several orders of magnitude as is typically necessary for polymers. This effect can also be avoided in the optimized geometry presented later in this study.
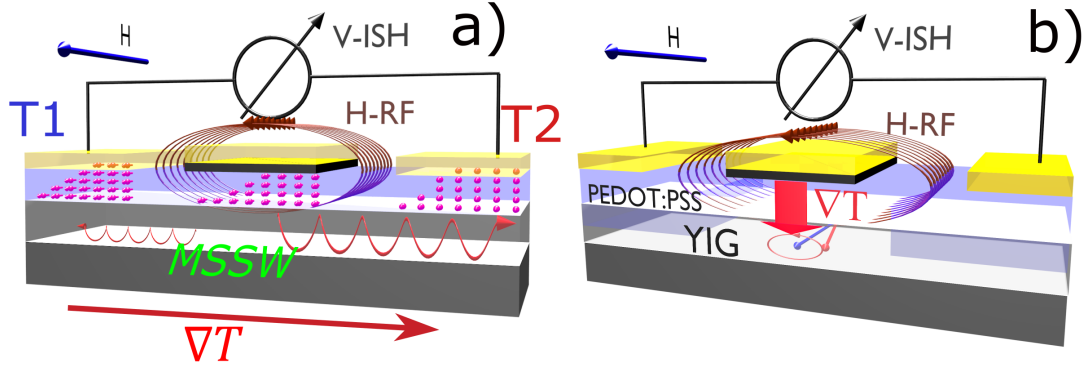
Figure 5.2 – Schematic illustrations of the possible voltages induced with FMR excitation in YIG/PEDOT:PSS bilayer. (a) The voltages result from MSSWs V_{MSSW} and spin pumping into the contacts $V_{Contact}$. (b) The voltage V_{Nernst} due to the Nernst effect induced by FMR power absorption.

A third artifact can be caused by the Nernst effect in the spin sink, [section 2.8.2]. At resonance condition, the absorbed power in the ferromagnet leads to a local heating which causes a perpendicular temperature gradient in the non-magnet (Fig. 5.2b). Together with the external magnetic field, the resulting Nernst effect can cause a voltage which similarly to the ISHE appears only at resonance and is reversed with reversing magnetic field. Because the Nernst effect appears in the same spot as the ISHE it can only be quantified in a suitable reference experiment which allows the Nernst effect but completely excludes the ISHE. While all these effects are mostly negligible when a metallic spin sink with large SOC and short SDL (like Pt) is used, they can be sizeable or even dominant for low SOC polymers. In that case, the measured voltage V_M is composed of four components

$$V_M = V_{ISHE} + V_{MSSW} + V_{Nernst} + V_{Contact} \tag{5.1}$$

where V_{ISHE} is the pure ISH-voltage, V_{MSSW} is the thermovoltage caused by the DEM, V_{Nernst} the voltage caused by the Nernst effect and $V_{Contact}$ the voltage caused by spin pumping into the contacts.

5.3. Experimental Details

5.3.1. Sample Information

The samples in this chapter are based on 100-nm-thick films of single-crystal YIG with a size of 2×5 mm^2 grown on GGG by LPE. For a number of samples, the YIG layer is patterned to form a 2 mm wide stripe, (Fig. 5.9) using Ar-ion milling with Al foil as a shadow mask which provides a stripe with smooth edges which are required for depositing a continuous polymer layer. More details are found in appendix C. All YIG samples used here are subjected to cleaning procedures with organic solvents followed by piranha following the steps explained in appendix B. The PEDOT:PSS is prepared and doped in the same way as in the previous chapter except using the PEDOT:PSS commercial formulation (Clevios PH1000, Heraeus) which yields higher conductivity with DMSO doping. The polymer is deposited by spin coating in an ambient atmosphere at 4500 rpm for 45 s, and then the films are annealed on a hot plate at $140°C$ for 10 min. The resulting PEDOT:PSS has a thickness of approx. 70 nm and $\sigma_{IP} = 800$ $S.cm^{-1}$. Rectangular contact electrodes of either Pt or Ru are defined at the edges of each sample. By the width of the electrodes which is given in table 5 and the sample size, the electrode spacing is defined which is an important parameter for the analysis of the results discussed through this chapter. The electrodes are deposited by magnetron sputtering using a shadow mask to guarantee well defined dimensions. For control experiments an interfacial layer of ca. 30 nm Al_2O_3 is deposited on the YIG by electron beam evaporation.

The layer sequence and the relevant parameters for all investigated samples are listed in table 5.

Table 5 – Samples parameters and layers dimensions for the full YIG and YIG stripe structure. The parameters d and w (shown in Fig. 5.1) denote the thickness and the width of the metal electrode used for ISHE measurements, respectively.

Sample	YIG	Al_2O_3 [nm]	Pt [d-w] [nm-mm]	Ru [d-w] [nm-mm]
S1[YIG-PEDOT:PSS-Pt]	Full	-	(10 - 2)	
S2[YIG-Al_2O_3-PEDOT:PSS-Pt]	Full	30	(10 - 2)	-
S3[YIG-PEDOT:PSS-Pt]	Full	-	(10 - 1)	-
S4[YIG-PEDOT:PSS-Pt]	Full	-	(10 - 2)	-
S5[YIG-PEDOT:PSS-Ru]	Full	-	-	(10 - 1)
S6[YIG-PEDOT:PSS-Ru]	Full	-	-	(10 - 2)
S7[YIG-PEDOT:PSS-Pt]	Stripe	-	(10 - 0.5)	-
S8[YIG-Al_2O_3-PEDOT:PSS-Pt]	Stripe	30	(10 - 0.5)	-

5.3.2. ISHE Characterization and Setup Configuration

The information of the ISHE setup and measurements configuration are explained in section 3.2.3. The stripline of the waveguide used for these measurements is isolated with a thin layer of PMMA to avoid any shorting between the antenna and the polymer.

To avoid any effects by ageing of the polymer, all ISHE measurements are done shortly after finishing the respective sample fabrication. The voltage values are extracted as the maximum of the curves fitted by a symmetric Lorentzian function [7]

$$V(H) = V_{ISHE} \frac{\Gamma^2}{(H - H_{fmr})^2 + \Gamma^2} \tag{5.2}$$

Where Γ denotes the spectral linewidth at half maximum. All ISHE measurements are carried out at the FMR position where both ISHE and FMR curves for each sample are measured simultaneously, Fig.5.3.
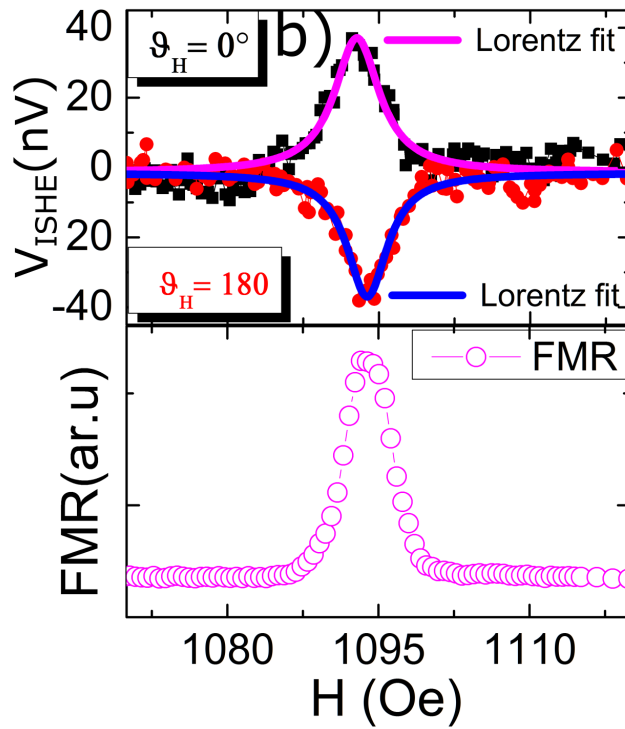
Figure 5.3 – Magnetic field dependence of the FMR (down) and ISHE (top) for the YIG-PEDOT:PSS bilayer illustrating the voltage measured at the same resonance position where the ISHE value is in its maximum.

5.4. Results and Discussion

The ISHE-voltage is given by equation 2.62. For all our samples we can assume the same spin mixing conductance at the interface between YIG and PEDOT:PSS. In order to allow for a quantitative comparison, we need to normalize by the cone angle $\Theta = \frac{\gamma h_{rf}}{2\alpha\omega}$, which can vary due to different damping or small variations in the coupling between the stripline antenna and the sample [8]. The necessary linewidth and rf-field h_{rf} can be extracted from the respective FMR absorption measurements.

Furthermore, comparing different samples is only possible if the sample resistance is taken into account because the ISH-voltage is caused by the ISH-current which flows in the sample and the voltage drop is proportional to the resistance of the sample in the area where spin currents are injected. So all voltages measured are divided by the respective resistance value and only the resulting currents are plotted and compared. This normalization by the sample resistance transforms Eq. 2.62 to

$$I_{ISHE} = -e \ \theta_{SH} \ \lambda_s(w/L) \ tanh(d_s/2\lambda_s) \ g^{\uparrow\downarrow} \ f \ lP \ \Theta^2 \qquad (5.3)$$

which is plotted for all the samples in the following, where L, w and d_s are the length, width and thickness of the spin-sink, respectively.

The first measurement is done on a sample with continuous YIG and PEDOT:PSS films, respectively and 2 mm wide Pt contacts (S1). This geometry is typical for ISHE measurements as in [27, 28] (Fig. 5.4(a)).

The ISHE is measured at the uniform mode of the FMR where maximum rf-absorption takes place as previously shown in Fig.5.3. ISHE measurements for sample S1 are shown in figure 5.4c. In this structure the YIG film extends over the whole sample and thus also underneath all PEDOT:PSS and the Pt contacts. This geometry is typically used to measure the ISHE in polymers. In Ref. [27] Au contacts were used which are replaced here by Pt in order to allow for better identification of artifacts due to spin pumping into the contacts.
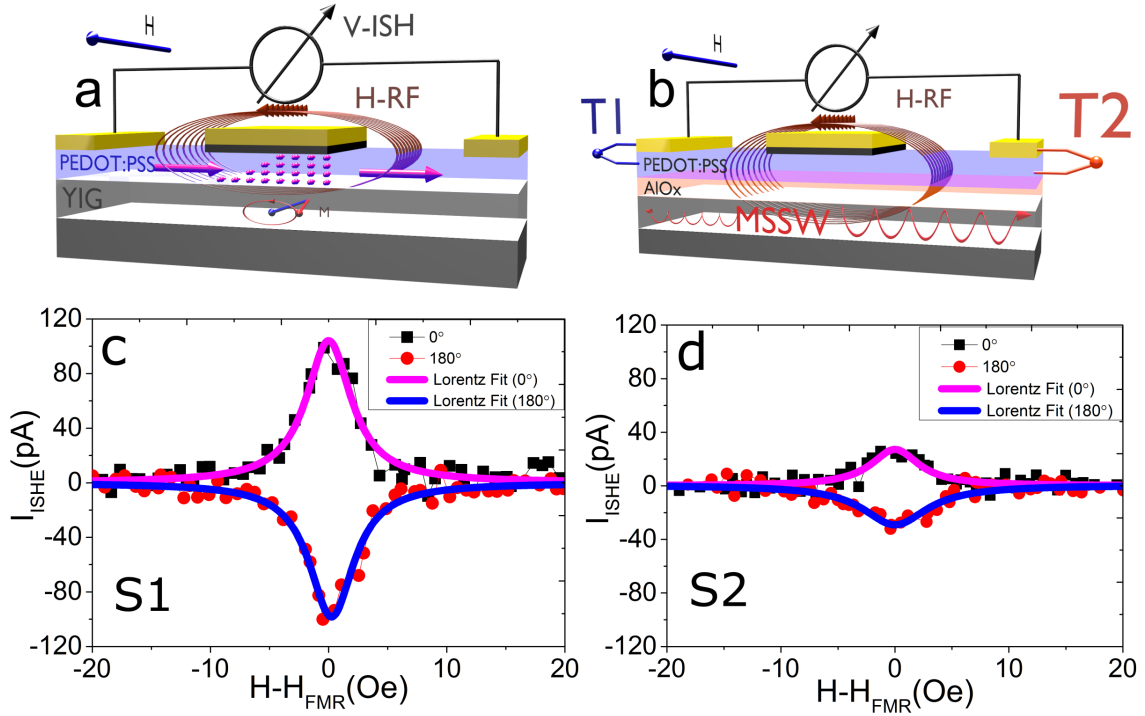
Figure 5.4 – ISHE current for two different YIG/PEDOT:PSS samples. Sample S1 has the geometry shown in (a) which is typically used in those experiments. As shown the expectation is that the spin pumping into the PEDOT:PSS is the origin of the measured voltage. The respective signal is shown in (c). For sample S2 which has the geometry shown in (b) an Al_2O_3 layer prevents any spin pumping and as in Ref. [8] we expect the MSSW to create a temperature difference between the two contacts which results in a thermo voltage. The resulting signal (d) is smaller than for the sample without insulating interlayer.

As expected the ISHE signal shows opposite sign for opposite magnetic field. These results are qualitatively consistent with the previous results reported for this polymer with this geometry [27, 28]. In Ref. [27] Ando *et al.* attributed this voltage to the spin-charge conversion in the polymer while Wang *et al.* [28] identified the thermal gradient resulting from MSSW as its origin. As we will see, both effects are present but there are even more effects to be taken into account.

As demonstrated in [8], we investigate a similar sample, however with an insulating interlayer between YIG and PEDOT:PSS which prevents any spin pumping (Fig. 5.4b). Structures S2 and S1 are completely identical except for a 30nm layer of Al_2O_3 between YIG and polymer. In this case, any voltage signal must result from thermally induced effects and either be induced by the MSSW or by the Nernst effect.

The signals measured for S2 are shown in figure 5.4d. It is worth noting that, both samples S1 and S2 also show that typical V-θ_H relation which results from the vector product feature of the resulting voltage with respect to the spin current and also the spin polarization, equation 2.59. In this case the magnet field is applied in-plane in an angle between $\theta = 0^o$ and $\theta = 180^o$ with respect to the MSWG. This

is shown in figures 5.5 (a,b) which show voltage curves for both samples S1 and S2 respectively in the angle range ($\theta_H = 0°$ to $\theta_H = 180°$). The voltages extracted from the curves' amplitude and also the difference V(S1)-V(S2) are also plotted and fitted with $cos(\theta)$, [Fig. 5.5c]. As shown here, not only V(S1) and V(S2) are fitted well with $cos(\theta)$, but also the difference V(S1)-V(S2) which may contain the pure ISHE, also is fitted well.
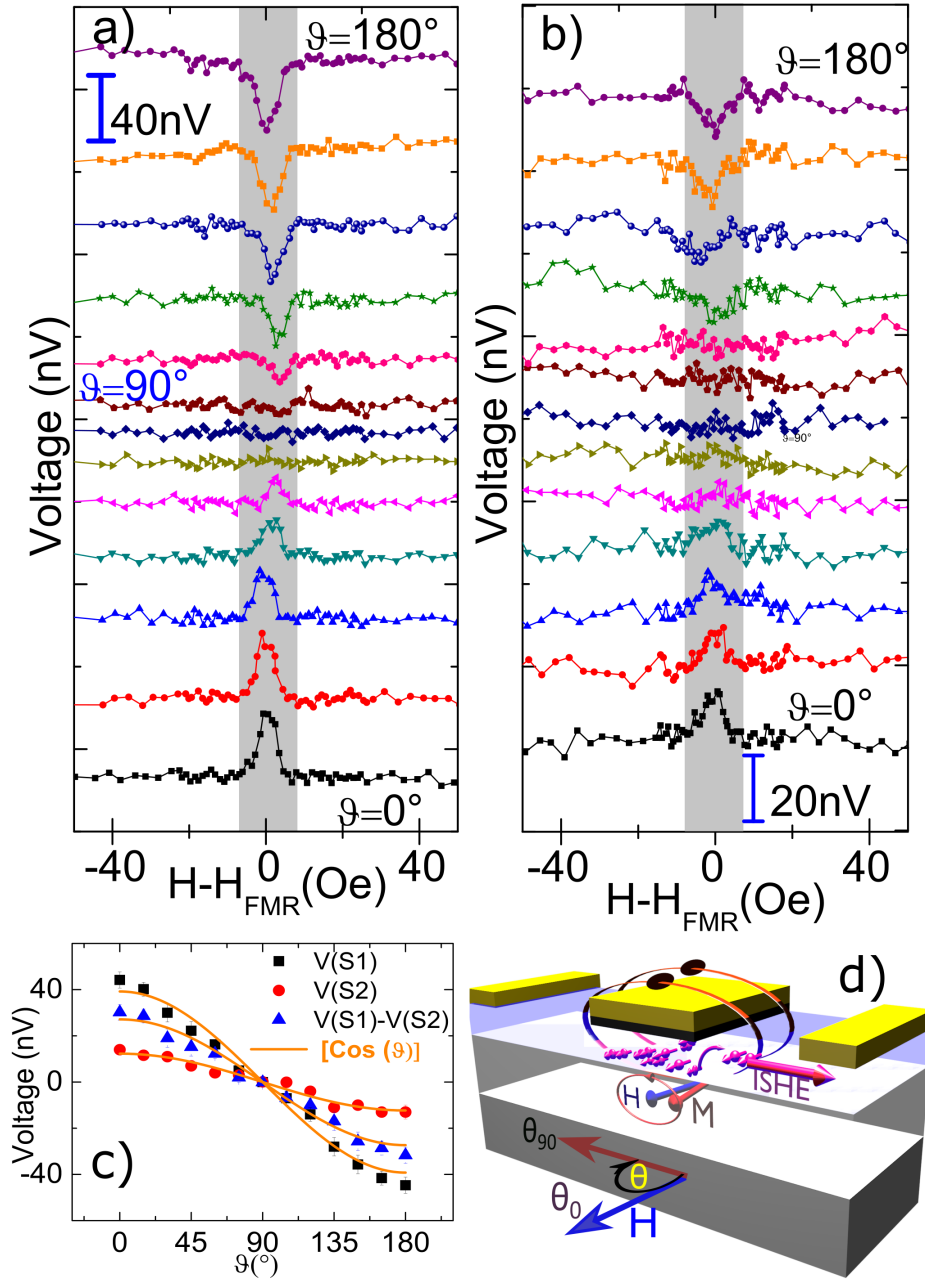
Figure 5.5 – (a,b) ISHE-angle dependence for sample S1 a, and sample S2 b, measured in the range ($\theta_H = 0°$ to $\theta_H = 180°$) of the in-plane geometry. (c) Cos (θ) fit of the V-θ_H dependence for V(S1) and V(S2) and also the subtracted voltage values V(S1)-V(S2) which are fitted also on the same way. (d) Schematic illustration of the $V - \theta_H$ in-plane configuration.

Unlike the results obtained by P. Want, *et al.* [28], the ISHE signals observed here for both structures S1 and S2, respectively (Fig. 5.4) are not equal but differ by a factor of 2. This is in contrast to the assumption in Ref. [28] that the observed voltage is only a thermovoltage induced by MSSW. Because simulations show that the temperature profile in the PEDOT:PSS is not modified by the Al_2O_3 insertion, the result strongly suggests that there is at least one other effect related to spin pumping. It would, however, be premature to take this as a proof for ISHE as we will see later. In order to elucidate the lateral temperature profile, YIG film is investigated under similar excitation conditions using Lock-In thermography which was done in our group by Olga Wid. Similar measurements can be found in [91]. As a result, we find that at the end of the structures the temperature difference is very small if present at all and close to our detection limit of approx. 0.1 mK, [Fig.5.6].
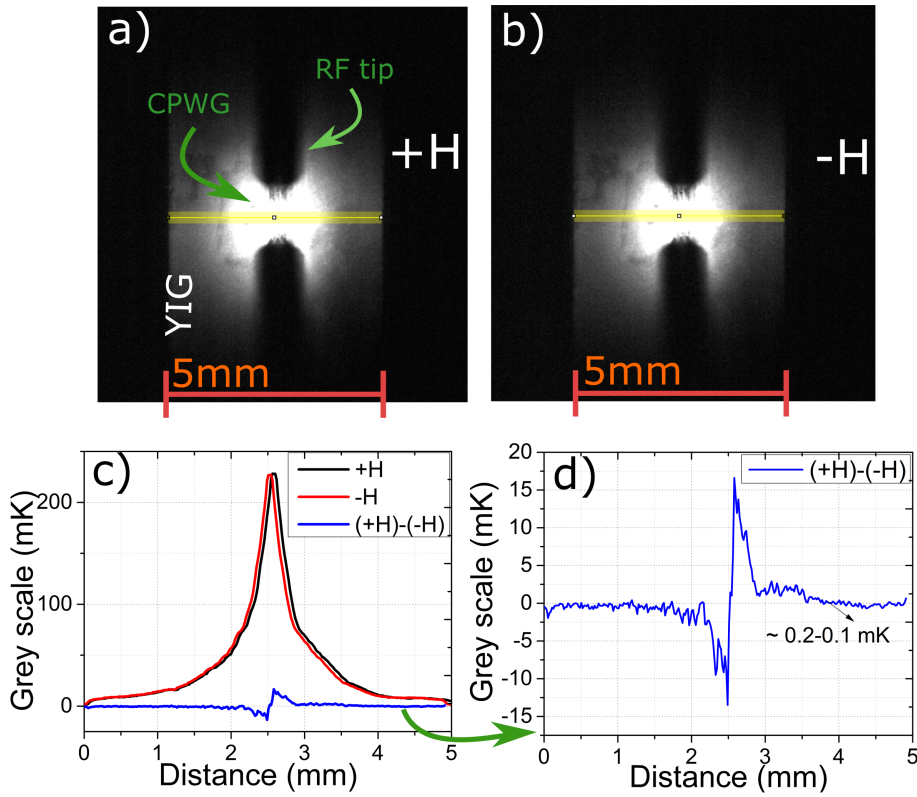
Figure 5.6 – LIT measurements for 100nm YIG sample using coplanar waveguide (CPWG). (a,b) LIT amplitude images taken close to the resonance at $+H$ and $-H$. The amplitude is measured at the region between two RF tips and underneath CPWG fabricated by electron beam lithography, metal (Ti/Ag/Au) deposition. The CPWG has a width of $80\mu m$. The RF power here is 19 dBm. (c) Temperature profile plotted for the highly Rf excited region along 5 mm length (the yellow stripe in a and b). The plots show the curves for both H polarities and also the difference between both cases. (d) A single plot with small T-scale for the temperature profile extracted from the difference between the curves of $+H$ and $-H$. A value between ∼0.2-0.1 mK is obtained at a distance $> 4mm$ close to the end of the sample. We should state that, only for better visibility the gray scale of the two images has been changed her.

These figures show the lock-in thermograpy (LIT) amplitude images for the rf excitation in 100nm YIG film using coplanar waveguide (CPW) in both in-plane magnetic field polarities ($+H$ and $-H$), Figs.5.6 a,b respectively. Figure 5.6c shows the temperature profile for both H polarities and also the difference between both cases which also is shown in a small T-scale in figure 5.6d. The investigation of the temperature gradient in YIG thinfilm during the rf excitation using LIT technique is studied in detail here [91, 92]. It should, however, be noted that the Seebeck coefficient of PEDT:PSS is sizeable and even 0.1 mK of temperature difference can lead to tens of nV of thermovoltage between the two contacts.

In order to investigate further side effects, we prepare a set of samples with different respective contact width (2 mm in sample S4 vs. 1 mm in sample S3). A smaller contact width simultaneously increases the spacing between the contacts from 1 mm to 3 mm modifying several aspects of the experiment. For smaller contacts, spin pumping into the contacts is reduced as are any temperature differences between the contacts and related thermovoltages. The ISHE, however increases because the relevant length in which the ISHE is induced is increased and shunting by the contact metal is reduced.

In our samples, smaller contacts cause a strong decrease of the signal indicating that at least in this configuration the ISHE does not dominate (Figs. 5.7c and 5.7d). To narrow down the origin of the signal we investigate two more samples with 1 and 2 mm contacts, respectively, but with Ru as a contact material instead of Pt (Figs. 5.7e and 5.7f). Ru has a smaller ISHE than Pt but a comparable Seebeck coefficient [154]. This allows us to distinguish between MSSW and ISHE in the contacts. Especially for the sample with 2 mm contacts the signal is reduced by more than 25 % from Pt to Ru showing that the ISHE in the contacts is not negligible although not fully responsible for the measured signal. Nevertheless, a significant contribution by the MSSW is still undisputed in these samples as is also expected because of the high Seebeck coefficient of PEDOT:PSS [27, 28, 90, 93, 105].
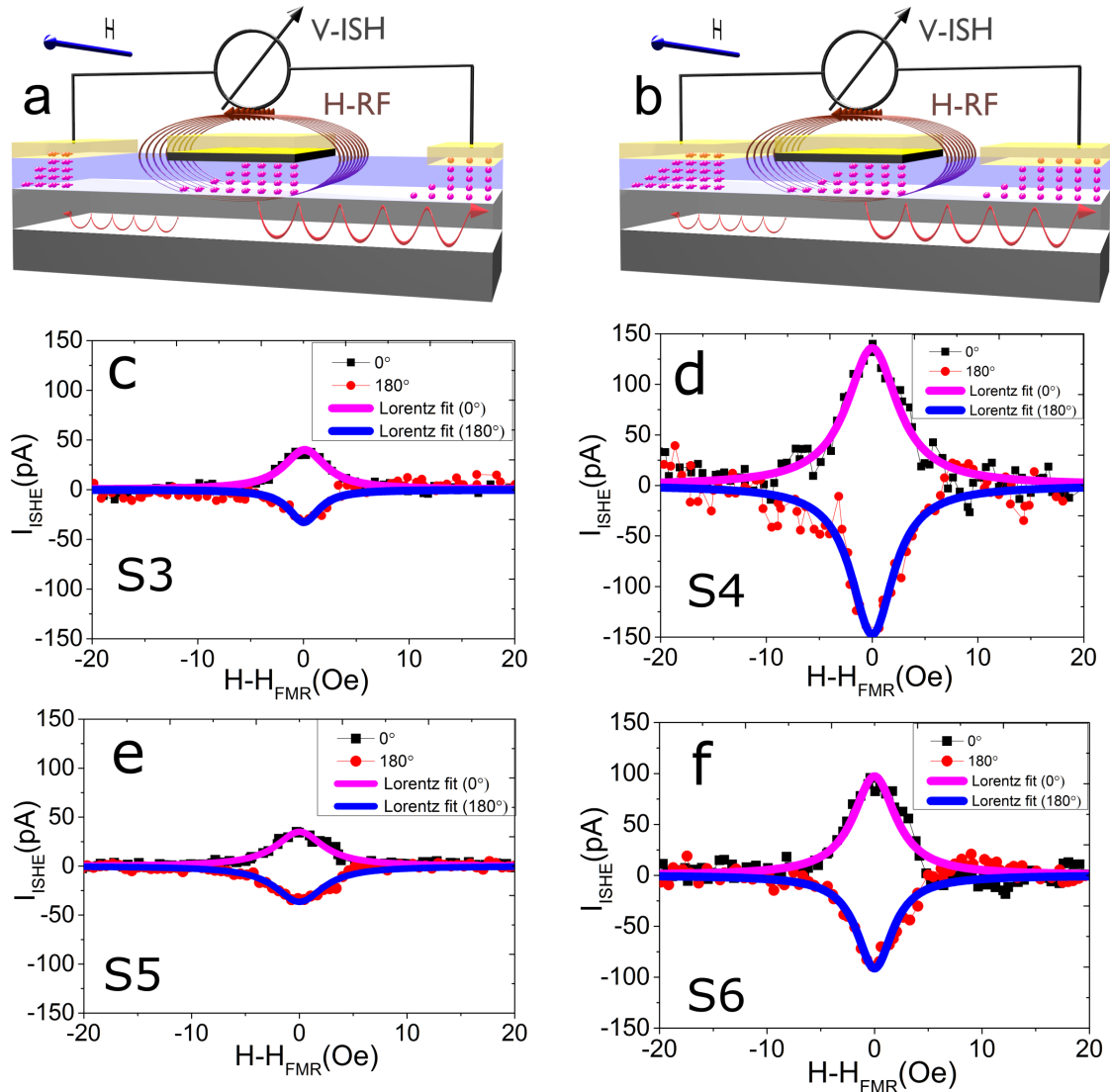
Figure 5.7 – ISHE results for combinations of two different respective contact widths and two different respective contact materials. As shown in (a) and (b) we expect the spin pumping into the contact and the related ISHE voltage to cause a larger effect for wider contacts. The respective results are shown in (c) and (e) for 1mm contacts and in (d) and (f) for 2 mm contacts. Although a thermovoltage caused by the MSSW cannot be excluded, the different results for Pt (c,d) and Ru (e,f) indicate that the main contribution stems from the spin puming into the contacts.

Based on these results, we have designed a sample geometry which eliminates at least the MSSW and the contact ISHE. Instead of a full YIG layer underneath the polymer, we use a YIG stripe which is smaller than and centered in the gap between the metal contacts (Fig. 5.9a). This way no spin pumping into the contacts can take place and also the asymmetric heating of the contacts by the MSSW is dramatically reduced. It should be noted that the lateral spacing between the YIG and the contacts is of the order of mm. Comsol simulations were performed to show that there is indeed a sizeable reduction of the temperature difference at the contacts due to the new geometry. As shown in figure 5.8c, 7 μK is the temperature difference

between the two ends which is very small compared to the original temperature gradient (100 μK) applied on YIG stripe edge.
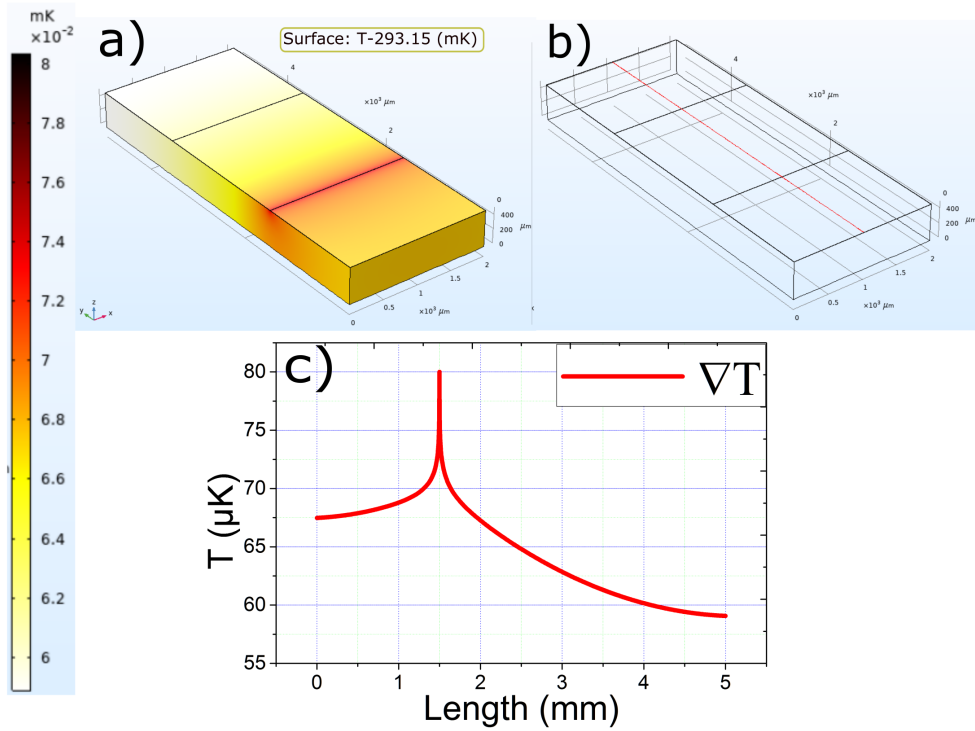
Figure 5.8 – Comsol simulation for the temperature reduction along the surface of the YIG-PEDOT:PSS sample where the width of YIG stripe is 2 mm YIG. (a) A temperature gradient of 0.1 mK is applied between the two edges of YIG stripe. (b) A schematic of the sample indicating the line where T values are extracted along the surface which are plotted in c. (c) A plot for the observed temperature gradient (T-293.15 K) along the sample surface. The plot shows a temperature reduction from the edge of the stripe until the ends of the sample which results in significant temperature difference between the two sample ends.

Again we prepare one sample for the ISHE measurement (S7) and a reference sample with Al_2O_3 (S8, sample structure in Fig. 5.9b) to prevent spin pumping. As shown in Fig. 5.9, both samples show a finite signal, however, the signal for the sample with no spin pumping is reduced by approx. 50%. These results finally prove that there is indeed an ISHE in PEDOT:PSS. Nevertheless, there is a further contribution that does neither originate from the MSSW nor from the contacts and that we can now attribute to the Nernst effect.

The Nernst effect is caused by the vertical temperature gradient induced by the heating of the YIG which occurs at ferromagnetic resonance. It is the only thermally generated artifact that is not avoided in our measurement geometry. To finally quantify the ISHE the Nernst voltage needs to be subtracted from the ISH-voltage and then the ISHE must be normalized by the sample resistance which finally yields an ISHE-current of approx. 25 pA.
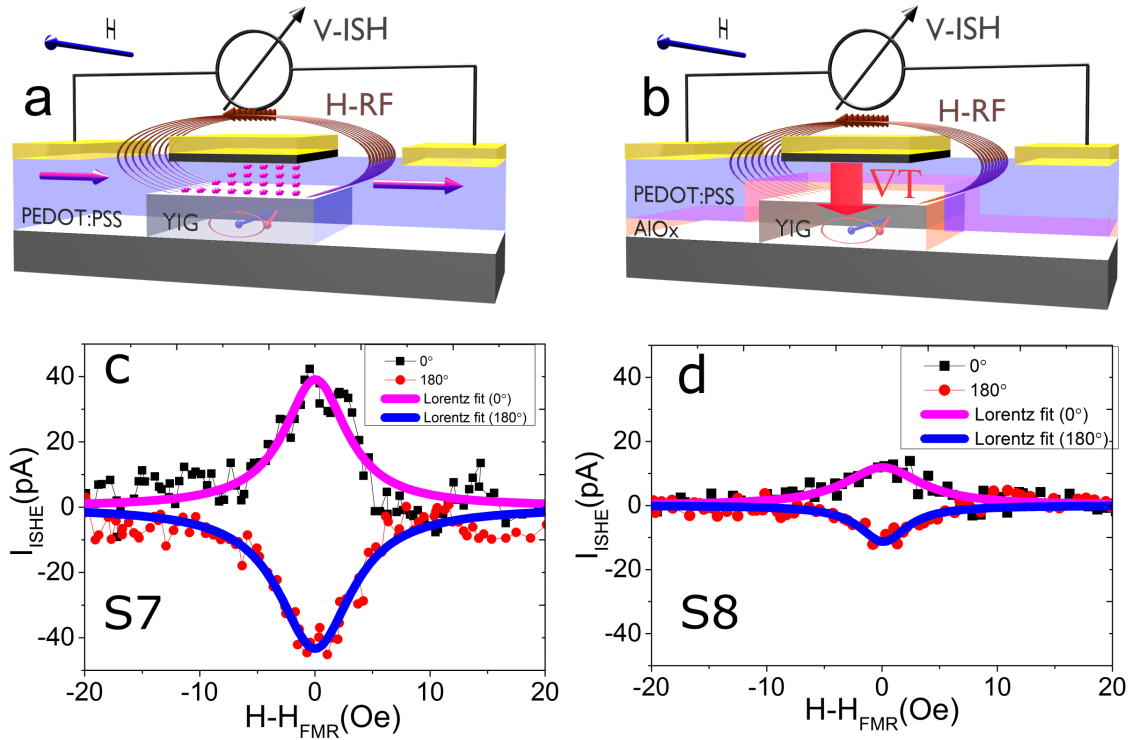
Figure 5.9 – Measurements of the ISHE in the optimized geometry. The sample (a) has a centered YIG stripe which does not extend underneath the contacts. The resulting ISHE current is shown in (c). When an Al_2O_3 layer is introduced between YIG and PEDOT:PSS in this geometry as small effect remains (d) which can be attributed to the Nernst effect caused by a vertical temperature gradient in the sample (b).

It should be noted that a comparison between different samples based on PEDOT:PSS is not straight-forward. Ageing of the polymer and of the samples can change the size of the effect and it is of utmost importance to compare only samples which are based on the exact same formulations of PEDOT:PSS and solvent, ideally prepared at the same time under the same conditions and characterized immediately afterwards. For our experiments we have made sure that all samples which were compared directly, were fabricated under conditions which allowed reproducibility better than the effects investigated. Sets of samples which were fabricated and measured for direct comparison comprise samples S1;S2, S3;S4,S5;S6, and S7;S8, respectively.

Because of these constraints we have not fabricated large series of samples to get a precise number for the spin mixing conductance or the spin Hall angle. Nevertheless, theoretical calculations were performed to predict the relevant parameters for PEDOT:PSS. These parameters were used to check whether our results fit at least the order of magnitude of the expectations.

5.5. Numerical Calculations of the ISHE

The numerical calculations are carried out by the INSPIRE Group in the institute of physics in Mainz. These calculations for the spin Hall angle are based on a recent theoretical work on the spin Hall effect in organics [155], where the spin Hall effect arises at the first order of spin-orbit coupling and it originates from the misalignment of $\pi-$orbitals in triads. In the hopping regime, the spin Hall effect, similar to the ordinary or the anomalous Hall effects, arises when in addition to hopping between pairs of sites (site i and j), the hopping in triads (hopping via an intermediate site k) is also considered. The hopping integrals over a triad loop for the spin Hall effect, give rise to a non-zero phase shift, if the molecular orientations of organic material are not aligned [155]. The importance of hopping in triads was first recognized by Holstein [156] and subsequently by others [157–164] in the study of the ordinary Hall effect and later for the anomalous Hall effect [165, 166]. Detailed derivation and results of the model used for the numerical calculations are given in appendix D. The spin Hall conductivity is obtained via $\sigma_{sh} = J_s^y/E^x$ with J_s^y the spin current along y direction when the electric field E^x is applied along the x direction. The spin Hall angle is determined as $\Theta_{sh} = \sigma_{sh}/(\sigma_{xx}\sigma_{yy})^{1/2}$ with σ_{xx} and σ_{yy} as the electrical conductivity along the x and y directions, respectively. The results for the spin Hall conductivity and the spin Hall angle are plotted in figure 5.10. The transport results are consistent with variable range hopping behavior, over a temperature range (40, 320) K, as expected. At room temperature, we get $\sigma_{sh} = 8 \times 10^{-7}$ and $\Theta_{sh} = 6 \times 10^{-7}$, consistent with our experimental results.
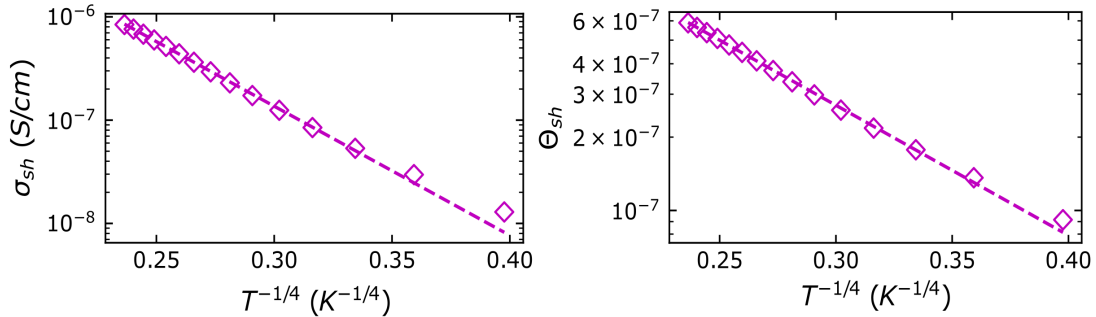
Figure 5.10 – Spin Hall conductivity σ_{SH} and spin Hall angle θ_{SH} of PEDOT:PSS as a function of temperature.

The magnitudes of the spin diffusion length λ_s and spin life time τ_s are calculated based on the characteristic parameters of the π-conjugated polymer PEDOT:PSS which has the same doping as our polymer. These parameters include: the electrical mobility μ_{IP} and μ_{OOP}, σ_{IP} and σ_{IP}, carrier concentration n, work function WF and the intermolecular distance δ. The magnitudes of these parameters are: $\mu_{IP} = 0.01-0.1 cm^2/V.S$, $\mu_{OOP} = 3 \times 10^{-5} cm^2/V.S$ [108], $\sigma_{IP} = 800$ S.cm^{-1}, $\sigma_{OOP} = 2.4 \times 10^{-3}$ S.cm^{-1}, $n = 3 \times 10^{20}$ cm^{-3} [27], and WF=5.1 eV [167]. For the polaron size calculations, we use the intermolecular distance between $\pi-\pi$ stacking layers in the backbone structure of the polymer δ (illustrated in figure 5.11). For the calculations, the value $\delta = 0.34$ nm is used based on the experimental observations reported for PEDOT:PSS prepared at the same doping conditions [125].

Figures 5.11, shows the numerically calculated values of λ_s and τ_s in a wide range of electrical mobility μ_{IP} and intermolecular distance δ of PEDOT:PSS.
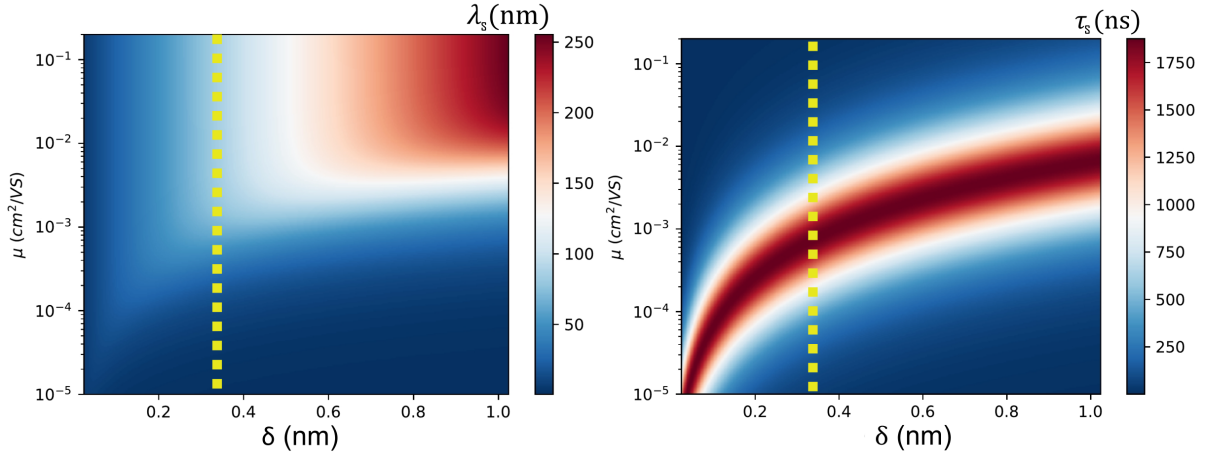
Figure 5.11 – 3D plots for the spin diffusion length λ_s and the spin lifetime τ_s change with the intermolecular distance δ in a wide range of the electrical mobility μ_{IP} of PEDOT:PSS (shown in colors). The dotted line corresponds to $\delta = 0.34$ nm.

Based on Eq. 5.3 we calculate the expected ISHE for our experiment using $\gamma = 2.8$ MH/Oe [8], d = 70 nm, $f = 5$ GHz , $l = 2$ mm, P= 1.21 [18] for YIG, w = 2 mm, L = 3 mm, $h_{rf} = 0.16$ Oe (corresponding to P = 80 mW for the given dimensions of our antenna), $\alpha = 1.5 \times 10^{-4}$, and $\sigma_{PEDOT:PSS} = 800$ S.cm^{-1}.

An approximate value for the spin mixing conductance of $g^{\uparrow\downarrow} = 8 \times 10^{17}$ m^{-2} for YIG/PEDOT:PSS was estimated in a former experiment [8].

Based on the mobility range reported in literature for PEDOT:PSS, the value estimated for λ_s which corresponds to $\delta = 0.34$ nm from figure 5.11 is 120 nm. Using these values obtained here, the calculation yields an ISHE current of 40 pA which is twice as much as we actually measure. Because of the large uncertainty of the input parameters this is still a surprisingly good agreement with our experimental results. Nevertheless, the fact that the orders of magnitude fit confirms at least that the claim of an ISHE of this order of magnitude is credible.

5.6. Summary

Summing up, the results presented within this chapter have shown that despite any previous claims [28], PEDOT:PSS exhibits a small but measurable ISHE which is in coarse agreement with theory. In typical sample geometries, this ISHE is easily concealed by thermovoltages induced by MSSW or by spin pumping into the contacts. By carefully optimizing the sample geometry it is possible to eliminate these two artifacts. The remaining small signal can be partially attributed to the ISHE and to the Nernst effect. These results show that extreme care is necessary to identify or even quantify ISHE in organic materials or other materials with low spin-orbit coupling. The sample geometry derived for our experiments can at least facilitate this procedure, although the Nernst effect can only be removed by careful extraction and subtraction from the original signal.

Chapter 6

6. Spin-to-Charge Conversion in Semiconducting Polymer PBTTT

6.1. Introduction

In this chapter, we present the first ever intensive study addressing the detection of spin-to-charge conversion in the semiconducting πCP PBTTT. Using the experimental protocols and systematic steps reported in chapter 5 for studying ISHE in πCPs, we investigate the ISHE in PBTTT in different experimental conditions. For each experiment, the polymer thickness, temperature, or doping is varied. This study provides a solid framework to address the major parameters influencing the ISHE in PBTTT. Moreover, it expands our knowledge giving us better insight into the spin relaxation mechanism that results from polarons transporting spin current in PBTTT.

πCP PBTTT has made its first entry in spintronics recently through addressing the polarons spin current transport and their relaxation mechanism [29]. In that work, only, the pure spin current transporting through the polymer was investigated and then detected in a Pt capping layer. However, no ISHE was observed in the polymer itself. Even when using very high rf excitation power utilizing pulsed-FMR (p-FMR) which provides high spin current density, no ISHE was observed, despite the FMR line broadening which is typically an indication of the spin pumping [14] [23]. These difficulties in observing any indication of ISHE in this polymer is substantially expected due to its weak SOC and hence its high SDL λ_s which surprisingly is found to reach 1 μm [30]. What makes PBTTT so interesting is the controllable and highly-ordered lamellar microstructure through the interdigitated side chains. These features provide steady and high charge mobility throughout the polymer which is a great advantage in microelectronic devices [108, 168–171].

---

[14]As discussed in chapter 4, FMR broadening is not necessarily an indication of the spin pumping due to the several magnetic damping sources resulting in FMR broadening. This scenario becomes very likely when using a conducting FM (e.g., Py).

6.2. Experimental Details

6.2.1. Samples Information

All samples studied in this chapter are composed of PBTTT polymer deposited on 100-nm thick films YIG grown on GGG. In all samples, the YIG layer is patterned to form a 2 mm-wide stripe done by Ar-ion milling with Al foil as a shadow mask. The YIG stripe is employed in our geometries to avoid any interaction with the contacts when measuring ISHE as discussed in chapter 5. For all samples, YIG surface is cleaned by organic solvents and piranha solution. The samples here have a size of ∼ 3.5 ×5 mm². The PBTTT films are spin-coated on the cleaned YIG surface. To vary the thickness of each PBTTT film on the YIG samples, spin-coating parameters such as speed were varied. The resulting films measured 25, 50, 100, and 200 nm thick. To optimize the structure of doped PBTTT and increase its conductivity, F4TCNQ was evaporated directly on the polymer [108]. PBTTT fabrication and doping information are explained in section 3.1.3. The fabrication steps and layer sequence of the devices prepared in this chapter are shown in figure 6.1. In addition to the YIG-PBTTT samples used for ISHE investigations, another sample was prepared to investigate the Nernst effect by adding an Al_2O_3 interfacial layer between YIG and PBTTT.
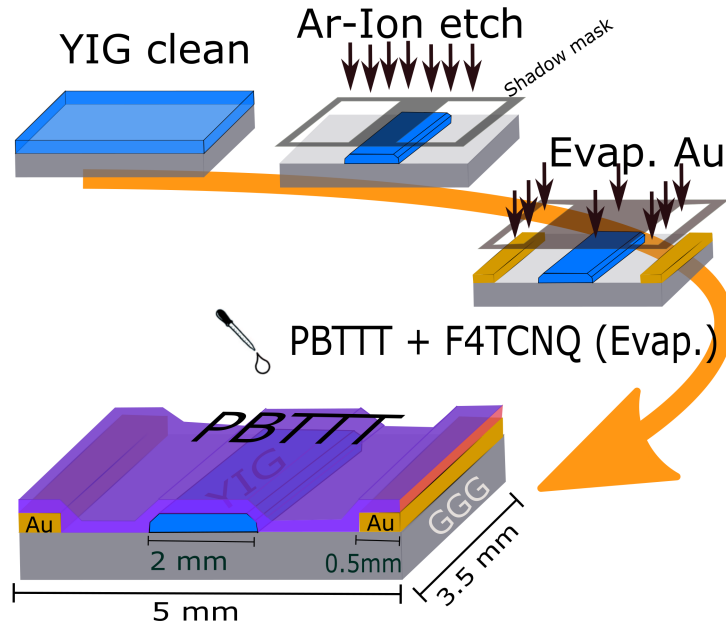
Figure 6.1 – Schematic illustration of the YIG-PBTTT samples indicating the fabrication steps and also the sequence and the dimensions of the different layers.

Several samples are fabricated for the study presented in this chapter. The main parameters and the layer sequence of these samples are listed in table 6. For ISHE measurements, Au electrodes are deposited directly on top of GGG substrate using electron beam evaporation and defined by a shadow mask, figure 6.1. In the resulting geometry, the electrodes are located far from YIG stripe and underneath the polymer.

Table 6 – PBTTT samples information

Sample	YIG [nm]	PBTTT [nm]	F4TCNQ [nm]	Al_2O_3 [nm]
S1[YIG-PBTTT]	100	25	20	-
S2[YIG-PBTTT]	100	50	20	-
S3[YIG-PBTTT]	100	100	20	-
S4[YIG-PBTTT]	100	200	20	-
S5[YIG-Al_2O_3-PBTTT]	100	100	20	30
S6[YIG-PBTTT]	100	200	20	-

6.2.2. ISHE Measurements

ISHE measurements are carried out using the sample geometry and measurement configuration explained in section 3.2.3. Cu leads are attached to the Au contacts at the end of the sample using silver glue. The polymer is removed from a small area of the Au top surface to ensure good contact with the Cu leads. An illustration of the sample geometry and measurement configuration is shown in figure 6.2. The ISHE measurements are performed at rf power of 40 mW. All information regarding the ISHE signal-to-noise optimization and amplitude modulation are explained in detail in section 3.2.3. Regarding the low-temperature measurements, the cryostat is liquid Helium cooled allowing for ISHE temperature-dependent measurements in the range between 300 K and 5 K.
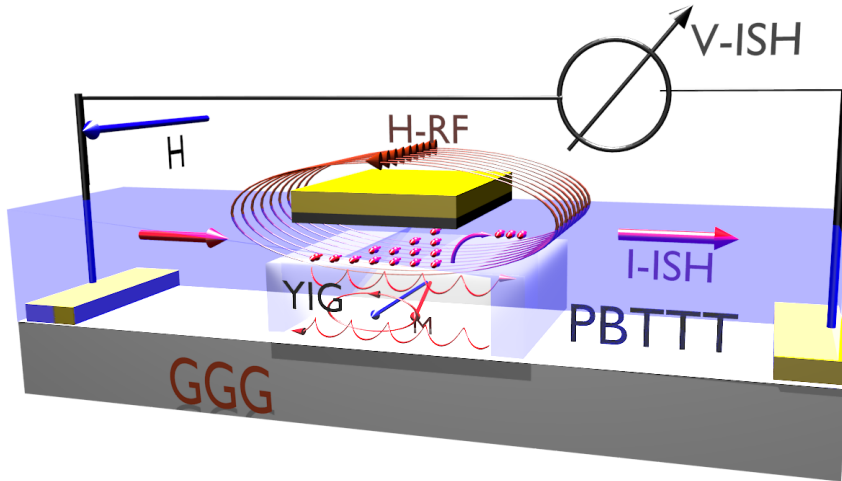
Figure 6.2 – A Schematic illustration of the sample structure and ISHE measurements configuration used in this study. YIG stripe is located underneath the PBTTT polymer. H is applied in-plane with respect to the microstrip waveguide and ISHE is measured at both ends of the sample using Cu leads attached to the Au electrodes.

6.3. Results and Discussion

6.3.1. ISHE Detection at FMR

ISHE is measured at the FMR in both magnetic field directions (0° and 180°) with respect to the MSWG which is done by changing magnetic field polarity, +H and -H. As shown in figures 6.3(a) and (b), the ISHE maxima is observed at the resonance in opposite directions correspond to the dc field polarities associated to the magnetic field polarity change. These resulting dc voltage profiles are in agreement with the ISHE characteristic discussed previously throughout this thesis.
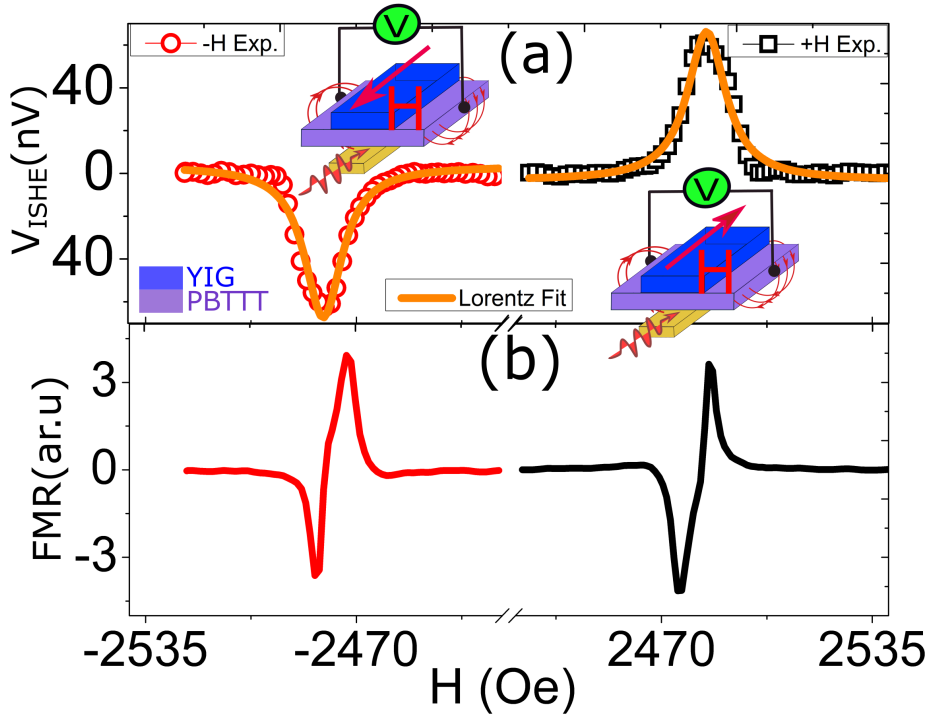
Figure 6.3 – Measuring ISHE in PBTTT at FMR. (a) ISHE measurements for YIG-PBTTT sample in both H field polarities, +H and –H (inset) as a function of the sweeping field. The ISHE measurements here are performed using an rf power of 40 mW. ISHE amplitude is observed and measured at the same position of the resonance as indicated in b.

6.3.2. Nernst Effect Induced by FMR Absorption

As concluded from ISHE investigations in chapter 5, measuring the pure ISHE in πCP can only be achieved by considering all voltage sources and artifacts associated with rf excitation. The most significant artifact here is likely to be the Nernst Effect, because of the polymer's unique thermoelectric characteristics, as described in sections 2.9.2 and 2.8.

In this study, the Nernst effect is investigated using sample S4:[YIG-Al_2O_3-PBTTT]. This structure with Al_2O_3 interfacial layer is efficient for studying the artifacts induced by FMR absorption. In order to detect a measurable voltage due to Nernst effect, we use relatively high rf excitation power ($\sim$ 100 mW). Figure 6.4a (up)

shows the curves of the voltage measured at FMR and induced by the Nernst effect V_{Nernst} which is measured for sample S5 at 100 mW rf power. A quite small but measurable voltage signal is observed when the field polarity changes, which is similar behavior to that shown during ISHE. This small V_{Nernst} ($\sim 5nV$) confirms the existence of the Nernst effect in PBTTT polymer. Despite its low magnitude, these findings are important especially when we go to high power because this effect increases with power. This is due to the higher power absorbed by the FM at FMR at high power which is shown by the large FMR amplitude. As a result, a high V_{Nernst} magnitude is expected at high power regime. Nevertheless, V_{Nernst} is still very small compared to the ISHE signal measured at the same rf power on an other sample with the same polymer thickness (sample S3 with $d_{PBTTT} = 100nm$) with no oxide interfacial layer, figure 6.4b. Furthermore, since the rf power used for the ISHE control experiments in this chapter is less than 100 mW (mostly 40 mW), any voltage originating from the Nernst effect will be very small and most probably in the noise level.
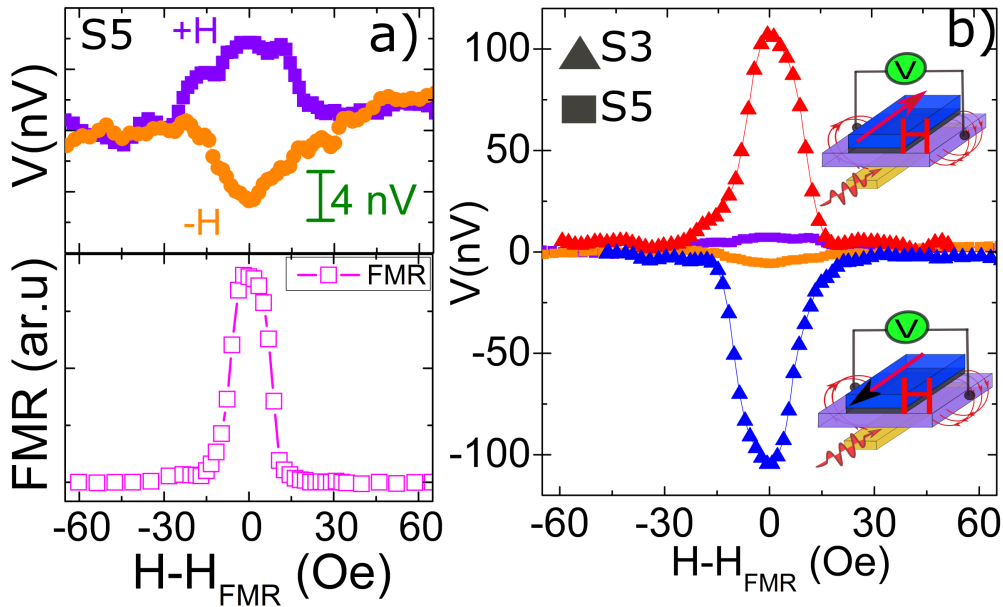
Figure 6.4 – Nernst effect investigations in PBTTT. (a) (Upper) Voltage measurements for sample S5 carried out at both magnetic field polarities +H and -H. (Lower) FMR absorption curve measured simultaneously with the ISHE. (b) A comparison between the voltage curves of samples S3 and S5 measured at both magnetic field directions. All dc voltage curves here are normalized by the associated FMR absorption. The measurements here are done at 100 mW rf power.

6.3.3. ISHE-Power Dependence

In this section, we study the dependence of the ISHE-voltage (ISHV) on the microwave power P_{MW}.

As discussed in section 2.2.2, the maximum power absorption - where the resonance takes place - is proportional to the amplitude squared of the driving field $|h|^2_{rf}$, $P_{ab} \propto h^2_{rf}$. From equation 2.62 and the cone angle definition in section 2.5.3 where $V_{ISHE} \propto \Theta^2$ and since ΔH is independent of P_{MW}, so at the same MW frequency f, $\Theta \propto h_{rf}$. From that, one can deduce the linear relation of V_{ISHE} to h^2_{rf}. This yields a linear relation with the power as,

$$V_{ISHE} \propto h^2_{rf} \propto P_{MW} \qquad (6.1)$$

This explanation can also be understood based on the proportionality between spin-pumping driven spin-current and the rf field square as $J_s \propto h^2_{rf}$ as discussed in section 2.5.3. The resulting ISHV linear dependence with applied rf power P_{MW} is reasonable because the maximum ISHV is measured at the FMR resonance mode H_{FMR} where the power absorption P_{ab} is maximum and therefore, $P_{ab} \propto P_{MW}$.

Figure 6.5a shows the ISHV curves measured at different MW power and figure 6.1b shows the extracted ISHV amplitudes from the curves which are plotted as a function of the applied MW power. As shown in figure 6.5b, the data show a nice fit in the linear regime as predicted by the V_{ISHE} model.
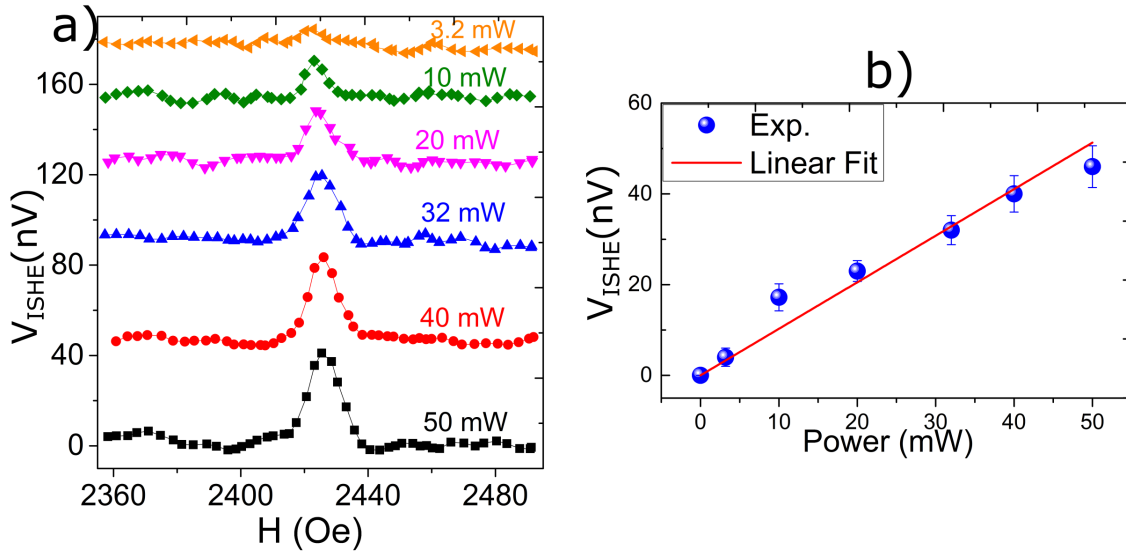
Figure 6.5 – ISHE-P_{MW} dependence. (a) Voltage curves measured for YIG-PBTTT sample at the FMR mode. (b) ISHV vs. MW power plot. The solid spheres represent the experimental ISHV maximum values extracted from ISHV spectra in a. The red line is the linear fit to the data.

6.3.4. ISHE-Angle Dependence

As demonstrated in equation 2.59, ISHE-current is characterized by the cross product with respect to the spin current $\vec{J_s}$ and magnetization vector $\vec{\sigma}$. The magnetization vector also is represented by the angle of the magnetization precession θ_m. In YIG ferrimagnet, with weak crystalline anisotrpy, $\theta_m = \theta_H$, where θ_H represents the angle of the applied magnetic field H. As a consequence, this cross product also describes the relation between V_{ISHE} and θ_H. Figure 6.6a shows the angular dependence of V_{ISHE} which is represented by plotting V_{ISHE} as a function of θ_H.
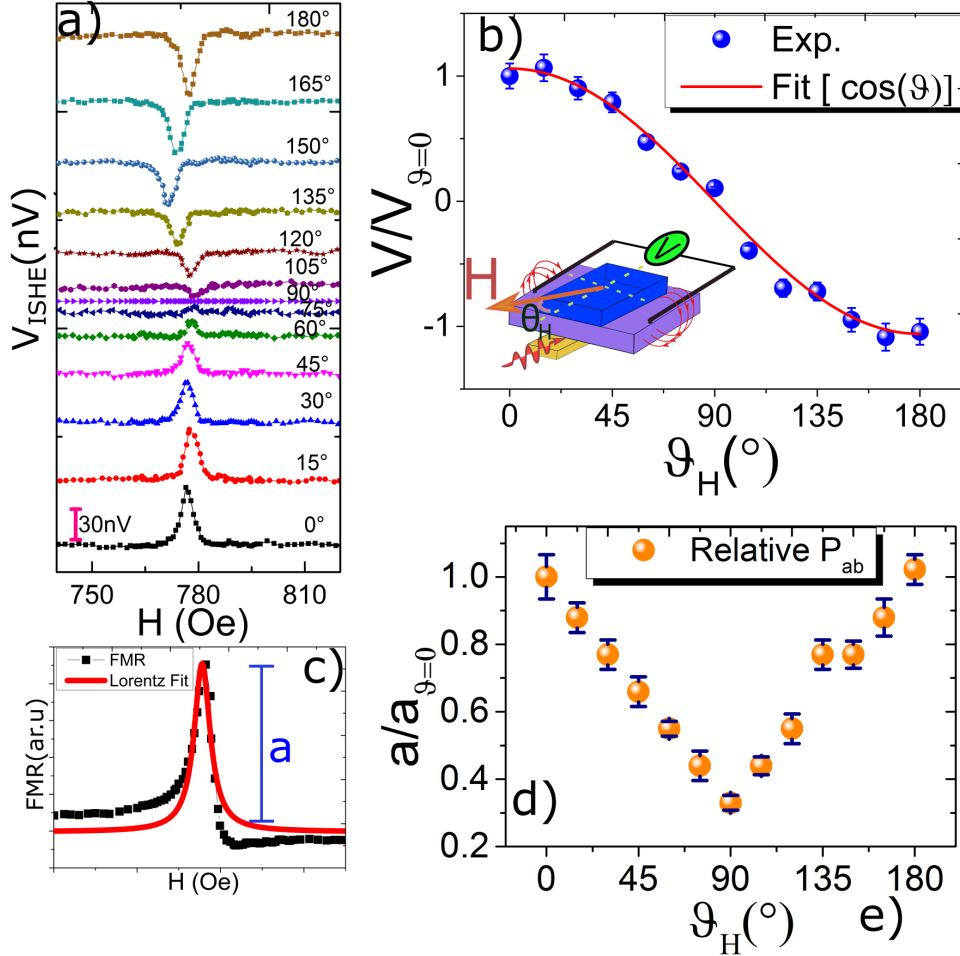
Figure 6.6 – ISHE-angular dependence for YIG-PBTTT sample done at rf field of $f = 4$ GHz. (a) ISHV spectra measured at different θ_H. (b) V_{ISHE} extracted from the ISHE curves normalized by FMR absorption P_{ab} and fitted to $cos(\theta_H)$. (c) An example of the FMR experimental curve and the Lorentz fit which is used to extract P_{ab} for each θ_H. The parameter "a" represents the FMR curve amplitude which is equivalent to the P_{ab}. (d) The $P_{ab} - \theta_H$ change represented by the relative amplitude, (relative to $a|_{\theta=0}$).

In these curves, the magnetic field H is swept in plane with respect to the MSWG, in the angle range ($\theta_H = 0°$ to $\theta_H = 180°$), Fig. 6.6b (inset). FMR spectra also are measured for this sample simultaneously with ISHV throughout the entire θ_H sweep.

It is worth noting that, as mentioned in the previous section, the V_{ISHE} is linked to the P_{ab} which in turn is linked to the h_{rf}. In microstrip or coplanar waveguides, the ratio of the rf power P_{MW} to the rf field h_{rf} components - acting perpendicular to the magnetization M producing magnetization precession around the applied field H - changes during the field sweep. This change yields variations in P_{ab} represented by FMR amplitude. This is clearly shown in figure 6.6d which represents the plot of the FMR absorption amplitudes as a function of θ_H. It is clear from this curve that, P_{ab} drops to 30% of its maximum value at the middle of the magnetic field sweeping, i.e., $\theta_H = 90^o$. As a consequence, this influence of θ_H sweep on P_{ab}, has a big impact on the ISHV-angular dependence, which results in a significant deviation from the perfect ISHV-angular behavior [172]. This deviation can be treated by considering the correlation of $[P_{ab}\ ,\ h_{rf}]$ and this is achieved via normalizing the ISHV curves by the P_{ab} extracted from the FMR curves. In our results, $V_{ISHE} - \theta_H$ angular dependence is obtained, figure 6.6b, by normalizing V_{ISHE} extracted from the ISHE curves by P_{ab} values extracted from the FMR curves. As shown in figure 6.6b, the experimental data can be fitted very well to $cos(\theta_H)$ which is in consistence with the ISHE-angular dependence for the in-plane configuration.

6.3.5. The Effect of Temperature and Doping on ISHE in PBTTT

The full picture of spin-charge conversion in PBTTT can be revealed by studying the spin transport and relaxation in different temperature and doping conditions. In PBTTT, spins are carried by localized charge carriers (or so-called spin-1/2 polarons) which move by hopping [29, 30]. The change of the carrier concentration n and their mobility μ with varying temperature and doping ratio and their relation to the ISHE may enable us to understand the ISHE mechanism in highly-doped PBTTT.

In this section we discuss in detail how do two processes affect ISHE in highly-doped PBTTT based on their impact on the ISHE characteristic parameters. It is important to mention that the ISH-voltage (ISHV) in temperature and doping studies represents the measured magnitude while the ISH-current (ISHI) represents the voltage normalized by the sample resistance.

Temperature Effect on ISHE

The effect of temperature on ISHE-voltage (ISHV) in PBTTT can be clarified by studying the influence of T on all parameters characterizing the ISHE mechanism. Referring to section 2.5.3, ISHV depends on the spin pumping and is quantified by spin current J_s , θ_{SH}, spin diffusion length λ_s and the spin-sink conductivity σ. As illustrated in equations 2.44 and 2.62, J_s is proportional to $g_{eff}^{\uparrow\downarrow}$ and cone angle square Θ^2. So, the change of J_s with T can by understood by studying $g_{eff}^{\uparrow\downarrow}$ vs. T and also Θ vs. T. Like many πCPs with low SOC and low spin relaxation rate, $g_{eff}^{\uparrow\downarrow}$ in PBTTT significantly depends on the intrinsic spin mixing conductance $g^{\uparrow\downarrow}$ and Sharvin resistance (spin resistance) R_s [equations 2.52 and 2.53].

To study the influence of temperature on these parameters and how this affects ISHV, we start with the $\sigma - T$ change. Adopting the VRH model which describes the charge transport in πCPs [section 2.7.3], $\sigma - T$ change follows the exponential relation illustrated in equation 2.64, which shows increasing σ with increasing T. This $\sigma - T$ behavior is expressed as a positive T-coefficient of conductivity which is the opposite of conductivity behavior in metals, which have a negative T-coefficient [29, 30, 108, 117, 173, 174]. Based on this difference in T-coefficients, ISHV is expected to scale with σ in πCPs differently from metals. In the FM/PBTTT bilayer, the high conductivity and gradient of the spin accumulation in the spin current direction give rise to the spin current $J_s(x)$, where $J_s(x) = -(\sigma_x/e) \bigtriangledown \delta\mu(x)$. Therefore, the charge current $J_c(y)$ measured along y-direction increases because $J_c(y) \propto J_s(x)$ [20, 27, 57]. At high conductivity, the polymer has high carrier mobility, high carrier concentration, or both. In this case, the spin carriers are scattered into a direction perpendicular to the spin current and this produces a large flux of the charge current transverse to the spin current. In this picture where both σ_x and $\delta\mu(x)$ increase, the spin current and hence the charge current increase. This may explain the enhancement of the spin-charge conversion efficiency at high conductivity observed in these π CPs despite the weak SOC [23, 27]. The effect of σ on ISHV can also be explained by the influence of n and μ on J_s, where increasing J_s results in ISHV increase, as illustrated in equation 2.62. It was found that the spin current induced

by FMR can only be transmitted through π CPs when a sufficient concentration of spin-carrying polarons is present [29, 30, 57]. For PBTTT, reducing T results in decreasing n and μ [29, 30, 108]. This was also confirmed by the Hall mobility measurements performed on similar samples while varying the temperature [108]. In this publication, they show that the ratio of conductivity at room temperature to 20 K is about 7, while the corresponding Hall mobility ratio is smaller than 3. Considering these findings, it is appropriate to conclude that, during the cool-down process, the polymer conductivity is not only affected by the Hall mobility but also by a lack of spin carrier concentration n. At high T the spins density n increases which leads to increasing J_s. This link between J_s and n can be understood in terms of the coupling between localized spins in the FM and the spin carriers - polarons - in the polymer [57]. This spin-polaron coupling is enhanced by increasing carrier density which in turn raises the spin current. The large increase in the conductivity with temperature leads to an increase in the diffusion coefficient D. The latter increases with increasing σ due to the Einstein relationships addressed in section 2.7.3 for highly-doped semiconductors (degenerate SCs) as $D = \left(\frac{\sigma}{g(E_f)e^2}\right)$. Even for the low-doping regime, D is expected to increase with T due to the Einstein relation for nondegenerate case where $D = \left(\frac{\mu k_B}{e}\right)T$. This increase in D results in increasing J_s, which follows its definition $J_s(x) = -(e/\mu_B)D \bigtriangledown \delta\mu(x)$ [20, 27, 57], where both the diffusion coefficient and spin accumulation gradient are proportionally related to J_s. As a result, increasing conductivity enhances the spin-polaron coupling and stimulates the flow of spin current into the polymer which in turn produces a measurable ISHE in the polymer regardless of its weak SOC. The ISHV is expected to depend largely on T, because ISHV depends on the conductivity. Conductivity, in turn, depends on μ and n, whose relationships with temperature we have already shown. The strong link between ISHV and J_s calls for further clarification for the influence of T on J_s in order to understand the ISHV change with T. To do this, the two main characteristic parameters related to J_s, $g_{eff}^{\uparrow\downarrow}$ and Θ, and their influence by T will be addressed here. As explained in section 2.4.2, the effective spin-mixing conductance is defined as $g_{eff}^{\uparrow\downarrow} = f(g^{\uparrow\downarrow}, R_s)$. The intrinsic spin mixing conductance $g^{\uparrow\downarrow}$ is found to be T-independent [175, 176]. However, the situation may become different with the $g_{eff}^{\uparrow\downarrow}$ due to the influence of R_s and how this additional factor changes with T. Since $R_s \propto (\lambda_s/\sigma)$, $g_{eff}^{\uparrow\downarrow}$ will have the same relationship with T as (λ_s/σ). For $g_{eff}^{\uparrow\downarrow}$ to remain constant with temperature, both λ_s and σ need to follow the same function of T such that the effect of T is canceled out. This means, while σ is increasing with T, λ_s should also increase in the same way. The most recent study of the spin current transport in highly-doped PBTTT shows σ and λ_s are proportional to each other [30]. Within a wide conductivity range (22 - 100) $S.cm^{-1}$ controlled by thermal annealing, the (λ_s/σ) ratio remains nearly constant. However, the ratio's relationship with T may be different from that in dedoping regime because the behavior of σ depends on which doping regime it's in. More specifically, one cannot assume σ behaves the same when both temperature and dopant ratio are changed, because n and μ depend differently on T and dopant ratio. So in πCPs, one may expect the ratio (λ_s/σ) and hence $g_{eff}^{\uparrow\downarrow}$ to change with T. Only if both σ and λ_s increase with increasing T, we may expect a slight change in $g_{eff}^{\uparrow\downarrow}$ with T. It is worth

mentioning that, in normal metals like Pt and Pd, different $\lambda_s - T$ behaviors were reported [117, 174]. In one study λ_s is found to be a T-independent, and in another study λ_s decreases with increasing T [117, 174]. This contradiction was attributed to the difference in how the diffusion coefficient D changes with T and also due to the dominating relaxation mechanisms in the spin-sink material. The change in λ_s with T in metals might be different from πCPs due to many reasons. These include, the different T-coefficient, the dominant spin relaxation mechanism in both kinds of materials, and the difference that n and μ change with T. As we knew in metals the spin concentration remains nearly unchanged with T while in πCPs both n and μ change significantly [29, 30, 108]. So far, no study has been done on the change of λ_s vs. T in highly-doped PBTTT as well other similar πCPs like PEDOT:PSS and P3HT. The way λ_s changes with T in highly-doped PBTTT is still unclear. However, if you consider the EY mechanism as the main source of spin relaxation in PBTTT [29, 30], we can then expect λ_s to increase with increasing T. As a result, if both λ_s and σ increase with T, $g_{eff}^{\uparrow\downarrow}$ will be roughly temperature independent.

The other parameter related to J_s is the cone angle Θ. As shown in section 2.5.3, $J_s \propto \Theta^2 \propto (P_{ab}/[\Delta H]^2)$. A significant change in FMR linewidth ΔH and the rf absorbed power P_{ab} is expected with varying T. This change when measuring YIG/PBTTT samples can be attributed to many reasons. The coupling between the waveguide and sample changes because the waveguide impedance changes at low temperature. This directly affects the P_{ab}.

Additionally, the saturation magnetization has a significant change at low temperatures, as predicted by Bloch law $M_s(T) = M_s(0)[1 - (\frac{T}{T_c})^{3/2}]$, where $M_s(0)$ is a parameter related to the net spin density in the FM system [136, 177]. In addition, because the saturation magnetization is linked to the cone angle [20, 80], and thus the linewidth; therefore, the saturation magnetization change will be reflected in the linewidth magnitude. As a result, the change of cone angle with T should be noted when analyzing the ISHV-T data.

Another major parameter related to the ISHV is the spin Hall angle θ_{SH} which describes the spin-charge conversion efficiency. θ_{SH} is determined as $\theta_{SH} = \sigma_{SH}/(\sigma_{xx}\sigma_{yy})^{1/2}$, with σ_{xx} and σ_{yy} being electrical conductivity along the x and y directions, respectively. Here the spin Hall conductivity is $\sigma_{SH} = J_s^y/E^x$, so that $\theta_{SH} \propto (J_s/J_c)$. From these relations, the reduction in J_s with decreasing T causes a decrease in θ_{SH}; however, the spin hall angle also depends on how much conductivity changes with T. Because σ depends on T, θ_{SH} may depend on temperature as well. However, due to the conductivity anisotropiy of PBTTT, it is difficult to determine how precisely $\sigma_{xx}\sigma_{yy}$ and θ_{SH} change at low T. So far, no studies have reported θ_{SH} for PBTTT. PEDOT:PSS πCPs, which also has a large conductivity anisotropy shows a clear θ_{SH} - T dependence over a wide temperature range as discussed in section 5.5. Therefore, the situation in PBTTT could be roughly similar to that of PEDOT:PSS. In metallic spin-sinks like Pt and Pd, $\theta_{SH} - T$ shows nonmonotonic variation through a wide T range due to the dominance of EY or DP [117, 178].

In conclusion, we see with decreasing T, the parameters D, n, μ and then J_s decrease. As a consequence, ISHV significantly decreases. The network connecting all ISHE-characteristic parameters based on their correlated change caused by temperature is illustrated in the diagram in figure 6.7. This diagram clearly shows how are

all parameters connected to each other and temperature.
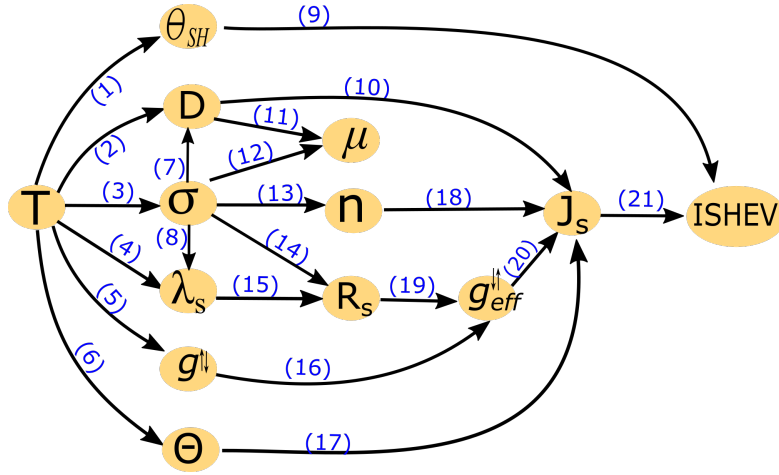
Figure 6.7 – The network of all ISHE characteristic parameters based on their correlated change caused by temperature. The mutual relations for all correlated parameters are listed in the tables below, alongside some references addressing these relationships.

Parameters relation No.	Reference
(1)	[29, 30, 108, 117, 174]
(2)	[29, 30, 108]
(3)	[29, 30, 108]
(4)	[29, 30, 117, 174]
(5)	[175, 176]
(6)	[20, 80, 136, 177]
(7)	[105, 109]
(8)	[30]
(9)	[20, 24, 57, 58]
(10)	[20, 27, 57]

Parameters relation No.	Reference
(11)	[29, 30, 109, 179]
(12)	[29, 30, 108]
(13)	[29, 30, 108]
(14)	[10, 56, 180]
(15)	[10, 56, 180]
(16)	[10, 56, 180]
(17)	[20, 58, 175]
(18)	[29, 30, 57]
(19)	[10, 56, 180]
(20)	[10, 56, 180]
(21)	[20, 27, 57, 58]

Doping Effect on ISHE

In πCPs, σ is tuned not only by temperature cooling-down but also by the dedoping process performed by thermal annealing (section 3.1.3). This process is found to be efficient for tuning polymer conductivity due to the significant reduction of the carrier concentration n which results in a large reduction of σ. Herein, decreasing σ is mainly because of the reduction of n which is related to the dopant ratio. This ratio is significantly reduced in dedoping as shown in figure 3.6. Consequently, we can assume the change in n during dedoping is dominant. For a specific polymer structure, when mobility is constant, σ is expected to scale linearly with n. As shown in figure 3.6b, the conductivity shows nonlinear behavior with the dopant ratio. This nonlinearity may be an indication mobility in fact changes with n. To test this hypothesis, a wide range of dedoping experiments were performed on a doped PBTTT sample, where n was measured at each doping step using ESR at the Cavendish Laboratory in Cambridge. These results are shown in figure 6.8a.

Here the conductivity data show a significant deviation from linear behavior, confirming the mobility changes during dedoping. In addition to these experimental findings, the influence of dedoping on μ can also be explained by its influence on the VRH mechanism as reported in some studies [30, 125]. This influence comes from the doping effect on the $\pi - \pi$ stacking distance and hence the localization length along the polymer backbone. Accordingly, increasing doping reduces the $\pi - \pi$ stacking distance and thus reduces the hopping length L_{hop} which eases hopping of the charge-carriers between the different sites through the polymer [105, 181].

Due to the big reduction of n and μ in dedoping, and because J_s is strongly linked to n as discussed previously, J_s is expected to decrease significantly along with σ. According to the strong ISHV-J_s dependence, reducing J_s will reduce ISHV.

Considering the strong link of these parameters: σ, n and μ to J_s , R_s, and $g_{eff}^{\uparrow\downarrow}$, the dedoping process is expected to affect these parameters as significantly as the temperature.

The network connecting all ISHE-characteristic parameters based on their correlated change caused by dedoping is shown in the diagram in figure 6.8c. This diagram shows how all parameters are connected to each other and the dedoping process. As we notice from the discussion above and also from the two diagrams in figure 6.8c and figure 6.7, the cornerstone parameter for tuning ISHV, either by changing temperature or the dopant ratio, is the material's conductivity σ. As a consequence, we expect decrease of normalized ISHV, or ISHI, to be identical in both processes.
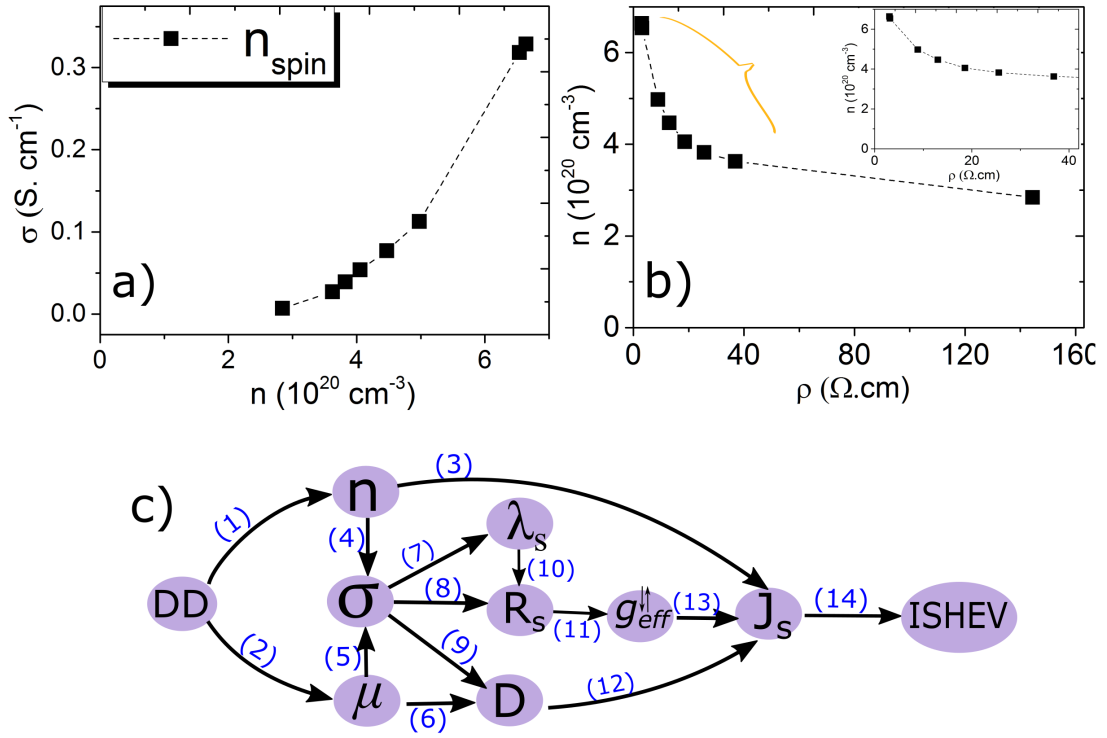
Figure 6.8 – (a) Conductivity vs. n_{spin} during dedoping process. (b) The trend of n_{spin} change with resistivity. (c) The network of all ISHE characteristic parameters based on their correlated change caused by dedoping (DD). The mutual relations for all correlated parameters are listed in the tables below, alongside some references addressing these relationships.

Parameters relation No.	Reference	Parameters relation No.	Reference
(1)	[30, 108]	(8)	[10, 56, 180]
(2)	[30, 108]	(9)	[105, 109]
(3)	[29, 30, 57]	(10)	[10, 56, 180]
(4)	[29, 30, 108]	(11)	[10, 56, 180]
(5)	[29, 30, 108]	(12)	[20, 27, 57]
(6)	[29, 30, 109, 179]	(13)	[10, 56, 180]
(7)	[30]	(14)	[20, 27, 57, 58]

ISHV-Temperature dependence in PBTTT

As previously stated, conductivity is the cornerstone of the ISHV-T behavior. The decay of σ with decreasing T in PBTTT is shown in figure 6.9 which includes the conductivity calculated from the resistance values measured for sample S4. The large decrease of σ with T is mainly attributed to the decrease of the carrier mobility and also the carrier concentration as discussed previously.

$$\sigma(T) = \sigma(0)exp\Big[-\Big(\frac{T_0}{T}\Big)^{1/d}\Big]$$

d= 2.2± 0.4

T_0 (K) = 1360
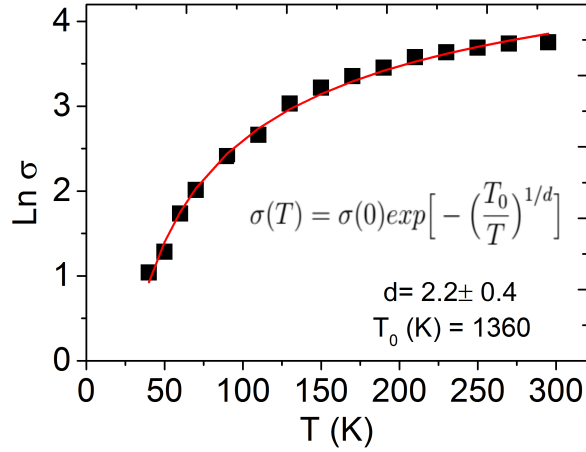
Figure 6.9 – Temperature dependence of the longitudinal conductivity σ measured for sample S4. The plot shows the best fit to the VRH model.

The line is a fit using the VRH model, equation 2.64. According to that, $\sigma - T$ behavior follows the formula $\sigma(T) = \sigma(0)exp\Big[-\Big(\frac{T_0}{T}\Big)^{1/d}\Big]$ where $d = D+1$. From this figure, the best fit yields $d = 2.2 \pm 0.4$ which is the closest to the fit predicted by Efros-Shklovskii variable-range-hopping (ES-VRH) model [104]. The characteristic temperature T_0 obtained from the fit is around 1360 K. These findings are in good agreement with the previous work done on the same structure [108].

The ISHV-T dependence is studied over a wide temperature range (5-295 K). Four samples are employed for this study, S1, S2, S3, and S4 which have PBTTT thickness of 25 nm, 50 nm, 100 nm, and 200 nm, respectively. All measurements here were performed at 9 GHz and used rf power of 40 mW. For each temperature, ISHV is measured at both magnetic field polarities, $+H$ and $-H$. To avoid any irreversible conductivity change due to the conductivity degradation of the polymer during cool down, all ISHV-T, FMR-T, and R-T measurements were performed by cooling the samples from 295 K and down to 5 K. The figures 6.10 (a-d) show the ISHV curves for the four samples at both magnetic field polarities over the temperature range (70-295 K). As clearly indicated here, no ISHV signal is observed below 70 K for most samples.
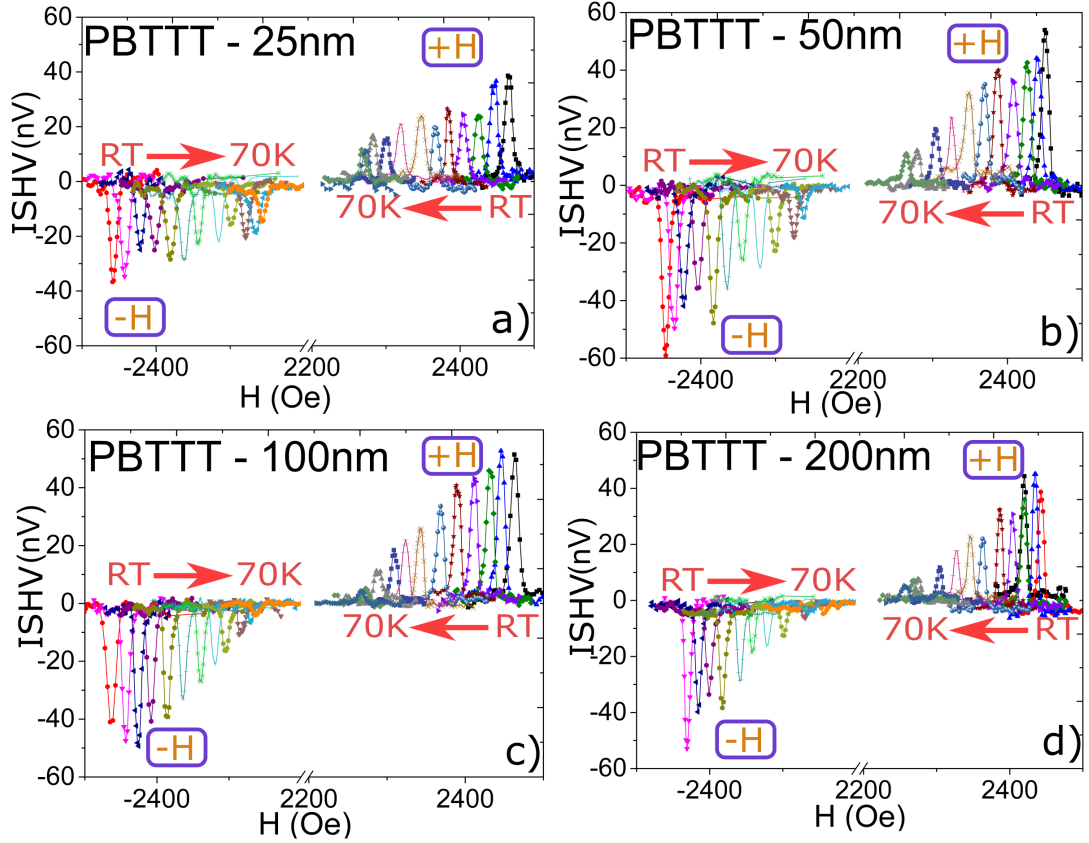
Figure 6.10 – ISHV curves for the YIG-PBTTT samples S1-S4 at a temperature range between room temperature (RT = 295 K) and 70 K. The plotted curves here are the measured ISHV curves normalized by the cone angle.

It is worth mentioning that, a big change of the FMR linewidth (ΔH) and P_{ab} is observed in cooled-down samples. This change becomes clear at low T which can be attributed to many reasons. The coupling between the waveguide and sample changes, because impedance at low temperature changes. This impedance change affects the rf absorbed power P_{ab} [147–149]. Additionally, the saturation magnetization has a large T-dependence as predicted by Bloch law mentioned previously. In addition, because the saturation magnetization is linked to cone angle [20, 80], and this is linked to the linewidth, the saturation magnetization change will be reflected in the linewidth magnitude. In the samples, these changes are identified by measuring ΔH and P_{ab} of the FMR curves simultaneously during ISHE measurements at each temperature. The observed values of ΔH and P_{ab} are plotted in the figures 6.11(a-d). These plots also include ($P_{ab}/[\Delta H]^2$) data because $J_s \propto \Theta^2 \propto (P_{ab}/[\Delta H]^2$. Because of the cone angle changes with T, and because $ISHV \propto J_s \propto \Theta^2 \propto (P_{ab}/[\Delta H]^2)$, to compare the ISHV measurements and account for the effect of temperature, the ISHV measurements must be normalized by ($P_{ab}/[\Delta H]^2$).
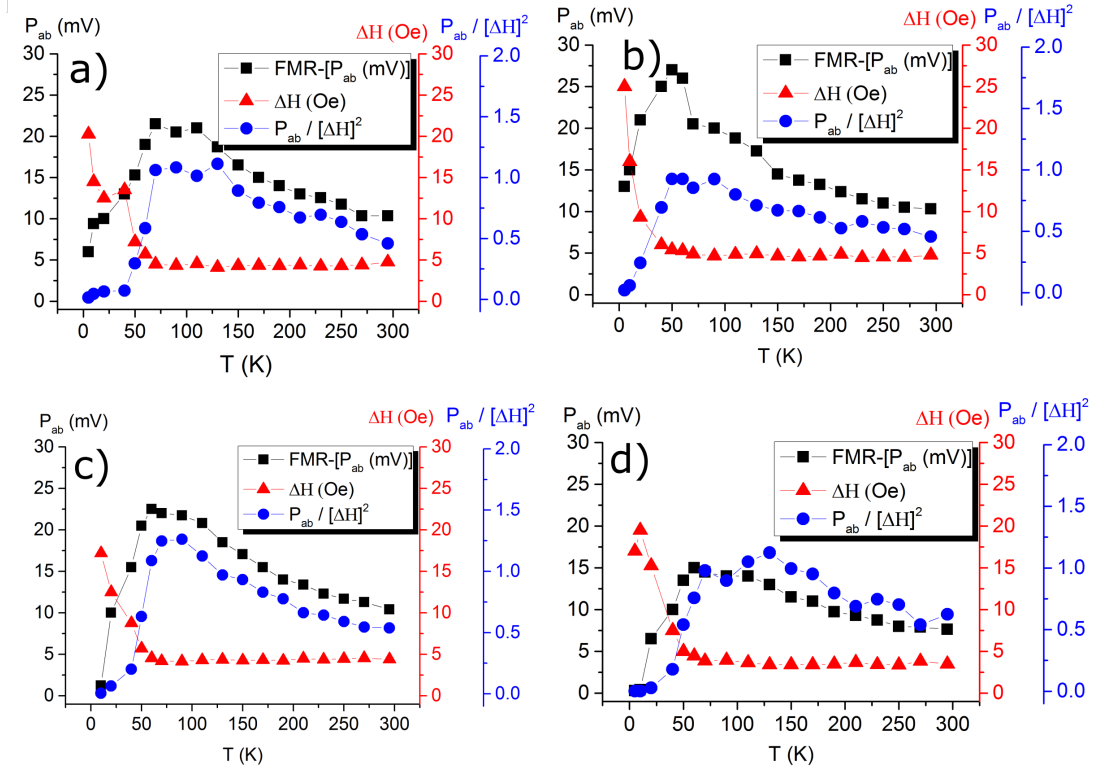
Figure 6.11 – (a-d) FMR linewidth and power absorption amplitude for the samples S1-S4 respectively, over the temperature range (70-295 K). Both ΔH and P_{ab} are extracted from the Lorentz fit of FMR curves. The ratio $P_{ab}/[\Delta H]^2$ is related to the cone angle square.

The decay of the ISHE in PBTTT over this temperature range is studied using the ISHV amplitudes extracted from the curves in figure 6.10 and then plotted versus temperature. This decay is demonstrated by the ISHE-T behavior for both ISHE-voltage and ISHE-current as plotted in figure 6.12a and 6.12b, respectively. A gradual ISHE decay is observed here and the signal nearly disappears below 70 K. As we see here, the ISHV and ISHI change with T is consistent with the conductivity decay with reducing T as shown in figure 6.9. This decay of the voltage unveils a suppression of the spin-charge conversion in PBTTT at low temperature which is a reasonable considering the significant decrease that the mobility and carrier concentration experience at low-T regime as confirmed by the experiments reported here [108]. Furthermore, this reduction at low T is in agreement with the J_s-related parameters change with T which is discussed in detail at the beginning of this section and also illustrated in figure 6.7.
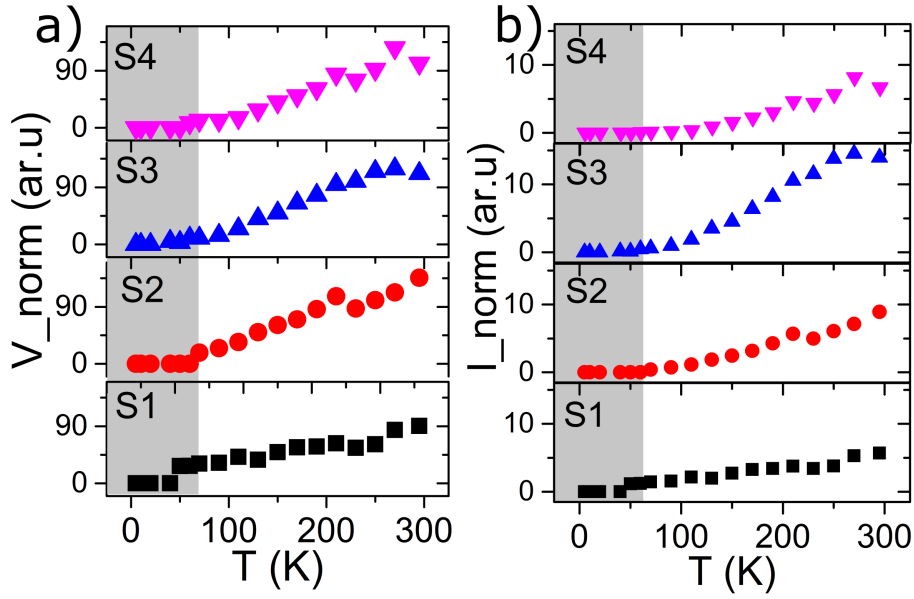
Figure 6.12 – ISHE voltage and current decay with temperature for the four samples S1-S4. The grey area indicates the region where the ISHE starts to vanish. V_{norm} and I_{norm} represent the ISHV and ISHI normalized by the cone angle.

ISHV-Doping dependence in PBTTT

In our highly-doped PBTTT, we study the doping effect on the spin-charge conversion efficiency by measuring the ISHV in samples with varying conductivity tuned by dedoping. The dedoping is performed on sample S6 by applying a sequence of post-annealing steps at $100\,°C$ in N_2 atmosphere for each step. The dedoping steps and the resulting conductivity of each step are listed in table 7.

Table 7 – Conductivity and resistance of PBTTT polymer vs. dedoping. The table shows the post-annealing steps and the resulting resistance and conductivity at each step. Zero step refers to the fully doped polymer

Annealing step	0	1	2	3	4	5	6	7	8	9	10	11
Annealing time(min)	-	15	20	20	20	20	20	30	50	120	100	120
R(kΩ)	1.2	1.5	1.8	2.6	3.3	3.9	4	4.8	5.6	7.3	10	16
σ (S.cm^{-1})	60	48	39	27	22	18	18	15	13	10	7	5

The dedoping process is performed on YIG-PBTTT which has a PBTTT thickness of 200 nm. The thickness was chosen to be significantly larger than the expected spin diffusion length in order to avoid a limiting the spin current by the finite thickness. Figure 6.13 shows the ISHI and ISHV plotted with the associated resistivity at each annealing step. As shown in this figure, the ISHV and ISHI are reduced by around one order of magnitude during dedoping which is close to the associated conductivity reduction indicated in table 7.
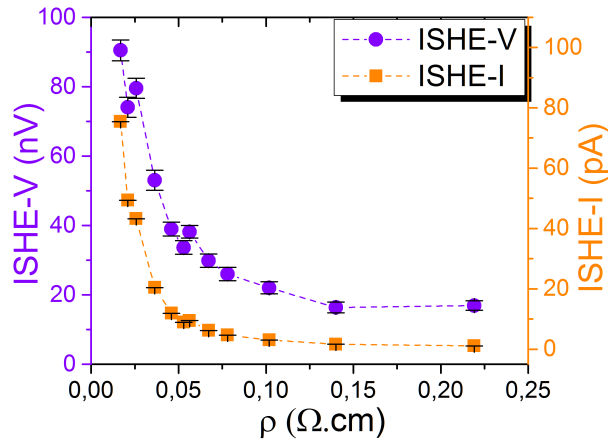
Figure 6.13 – ISHV and ISHI for YIG-PBTTT(200nm) plotted as a function of the sample resistivity ρ. The current plots are obtained by normalizing the voltage with the sample resistance. ρ is calculated from resistance value measured for the sample at each annealing step.

The pronounced drop of the spin-charge conversion efficiency demonstrated by the ISHV in PBTTT is an indication of the diminishing of the spin current transport efficiency into the polymer at low n regime. The big reduction of the carrier concentration during dedoping sheds light on the dominant role of n on ISHV decay in PBTTT. However, the associated reduction of mobility during dedoping also reveals an important contribution of the carrier mobility on the ISHE decay as well. The mobility change during dedoping can also be identified from the difference between the overall trend of the n reduction plotted with ρ (Fig. 6.8b), and the trend observed for the ISHV and ISHI with ρ shown in Fig.6.13. The difference becomes more obvious if we compare both at similar ρ range as shown in the inset of figure 6.8b.

To conclude here, the ISHV decay in highly-doped PBTTT during dedoping process is explained by the enormous reduction of the carrier concentration n and also a considerable reduction in the mobility μ. Considering that the spins are carried by polarons, these results point to the key role that the mobile carrier density and inter-polaron distance play in spin diffusion and spin relaxation in highly-doped PBTTT. Eventually, we conclude that the ISHV and the spin current transport in the PBTTT polymer become less efficient in the low doping regime.

Mobility μ vs. Carriers Concentration n Effect on ISHV in PBTTT: A Comparison Study

As demonstrated before, both n and μ change in both cooling-down and dedoping processes. We also found that n change is dominant in the dedoping process (Figs. 3.6 and 6.8a), and μ change is dominant in cool-down process [108]. The fact that each parameter is dominant in different regimes could imply ISHV is not inherently the same during both dedoping and temperature change.

In this section, we study the ISHV rise and decay while tuning the polymer's conductivity by varying the doping concentration and temperature separately. We

perform a comparison study for ISHI in both cases employing the results obtained in section 6.3.5 for sample S6 for the case of σ tuned by dedoping method. On the other side, for σ tuned by thermal cooling, we use the ISHV-T dependence results obtained for sample S4. The role of spin carrier concentration n and mobility μ in ISHI decay is studied using two YIG-PBTTT samples with the thickest PBTTT (samples S4 and S6, PBTTT 200nm). The reason for using the thick film is to avoid the influence of the active thickness change during the temperature change. However, this influence will not be significant as the film thickness is much bigger than the spin diffusion length. Figure 6.14 compares the ISHI decrease while reducing the conductivity using these two mechanisms. Interestingly, the ISHI change for both cases is almost identical. However, referring to our discussion at the beginning of this section, this consistency can be explained due to many aspects. Although the reduction of n and μ may be different in both controlling regimes, the similar measurements of ISHI reveals that there is compensation in n when μ is reduced and vice versa.

This, in turn, results in nearly similar magnitude of $(n \times \mu)$ which means there is a similar change in the conductivity in both approaches. The ISHI change with σ might mean that the change in ISHE is related to the conductivity itself rather than the mobility or carrier concentration alone. Moreover, these findings highlight the big role of the conductivity in the spin-charge conversion in πCPs which is consistent with our discussion before. Finally, these results confirm the strong correlation between n and μ in the cooling-down and dedoping process clarifying that both are inseparable.
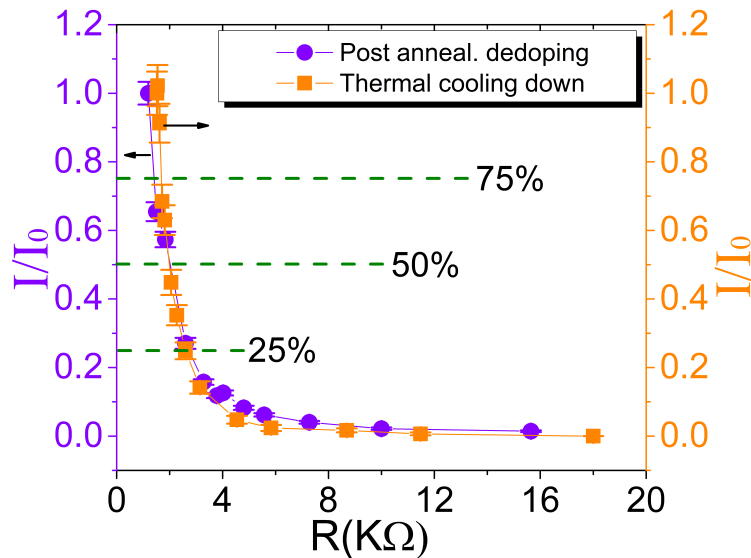
Figure 6.14 – The role of n vs. μ in the rise and decay of ISHE. The plots represent the current values obtained from the normalized ISHV with the sample resistance. I_0 in the cool-down case is the ISHI at the RT. In the dedoping case, I_0 is the value for the fully doped polymer. The ratios indicated by the plotted lines in the figure represent the current ratios at different decay regions. The error bars are estimated from the uncertainty in the fitting of ISHV curves.

6.3.6. Estimation of Spin Diffusion Length λ_s of PBTTT

As explained in section 2.5.3, ISHE voltage created in PBTTT can be estimated from the injected spin current J_s and the spin accumulation $\delta\mu$ induced by spin pumping into the polymer. The latter is obtained from the Bloch equation for the spin carriers in spin sink [20, 27, 57].

In this case the spin current is $J_s(x) = -(\sigma_x/e)\bigtriangledown\delta\mu(x)$ where the spin accumulation at the interface $\delta\mu_0$ is independent of polymer thickness.

In systems like PBTTT πCP with weak SOC and large spin-life time τ_s, one of the leading causes of the inverse spin-Hall effect is building up the spin-dependent chemical potential $\mu(x)$ where its gradient induces a spin current [27, 57]. Considering the spin accumulation induced by spin pumping and the coupling between the spins in the FM and the spin carriers in the polymer, ISHE can be obtained by integrating the spin current over the whole polymer thickness [20, 27, 57]. Adopting these considerations, the ISHE voltage is expressed as [20, 27, 57]

$$V_{ISHE} = \theta_{SHA}(\ell/d)(1/e)tanh(d/2\lambda_s)tanh(d/\lambda_s)\delta\mu_0 \tag{6.2}$$

Where θ_{SHA}, ℓ, and d are the spin Hall angle, FM effective length, and the polymer thickness, respectively.

Estimating spin diffusion length λ_s and spin lifetime τ_s for PBTTT is achieved by studying ISHV for different PBTTT thicknesses adopting the model represented in equation 6.2.

We present here the results of the ISHV-thickness dependence study done on the four YIG-PBTTT samples S1-S4, over temperature. The ISHV value is obtained from the average of the ISHV curves' amplitude magnitudes for both magnetic field polarities at each temperature (Fig. 6.10). It should be noted that for the formula given here no normalization by the resistance is necessary. The V_{norm} at each temperature represents the extracted voltage normalized by the cone angle.

Figures 6.15 show the ISHE voltage change with PBTTT thickness at different temperatures. The spin diffusion length is obtained by fitting the ISHV vs. d curves (Fig. 6.15) according to equation 6.2. As shown here, the ISHE voltage is fitted to the equation 6.2 well at all different temperatures.
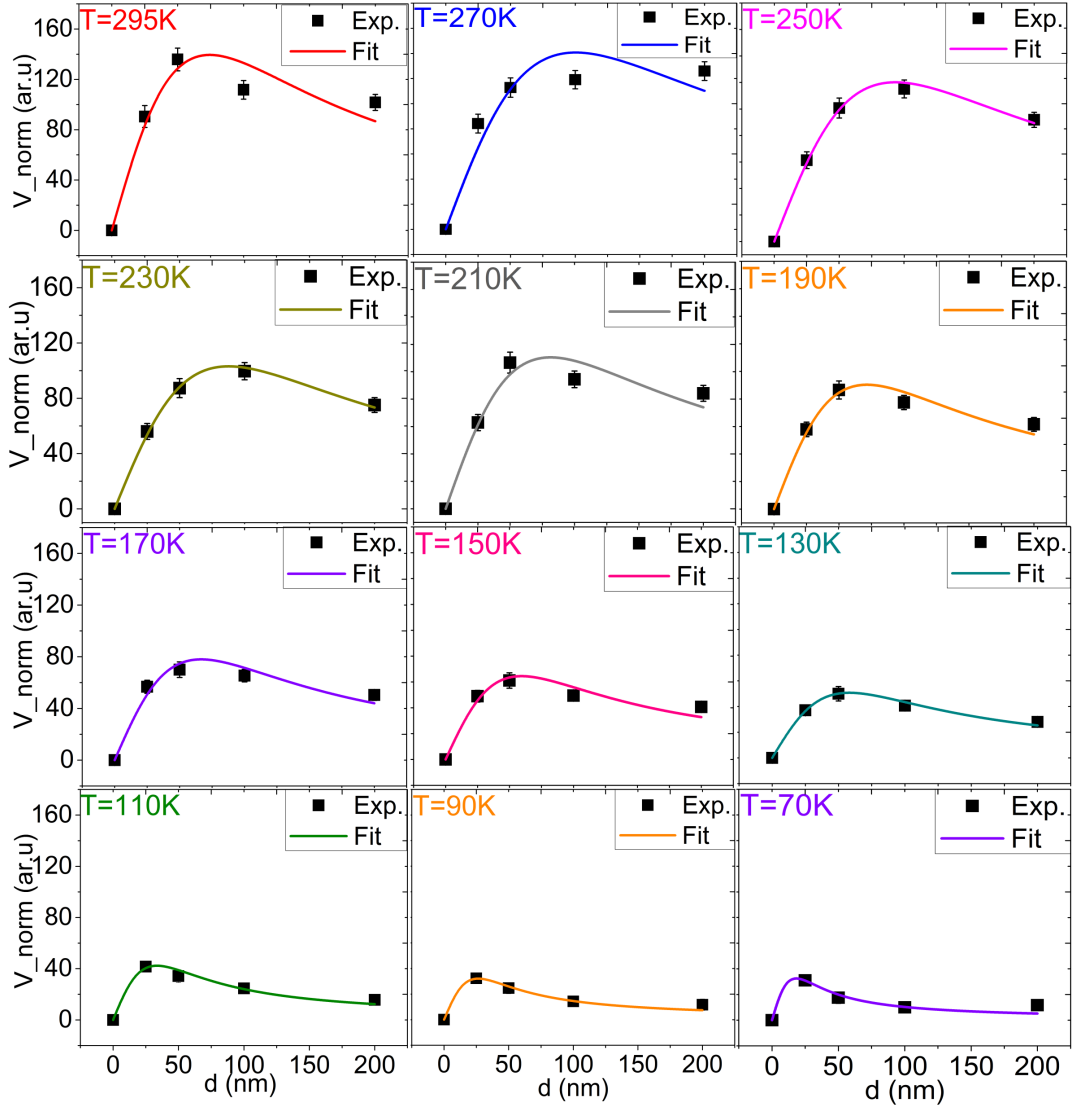
Figure 6.15 – ISHV-thickness dependence at different T values in the range between (295 - 70 K). d represents the PBTTT thickness. The data are fitted due to equation 6.2. The errors of the voltage are extracted from the Lorentz fit of the ISHV curves.

The values of λ_s extracted from the individual curves are plotted as a function of T and shown in figure 6.16. As depicted in this figure, λ_s has a clear temperature dependence with a maximum value of 67 nm. By reducing T, λ_s clearly decreases and reaches 12 nm at 70 K. This reduction in λ_s may be an indication of an increase of the spin-flip rate in the highly-doped PBTTT at low T. A reduction of the spin diffusion length with decreased temperature is consistent with the reported behavior in other studies [117, 174]. This hypothesis is further supported when taking into account the positive T-coefficient of conductivity (Fig. 6.9) which is in contrast to the case of the metals which have negative T-coefficient [117, 173, 174]. The resulting $\lambda_s - T$ behavior can be understood based on the dominant mechanism that governs the spin relaxation in different temperature ranges which will be discussed in detail in the next sections.
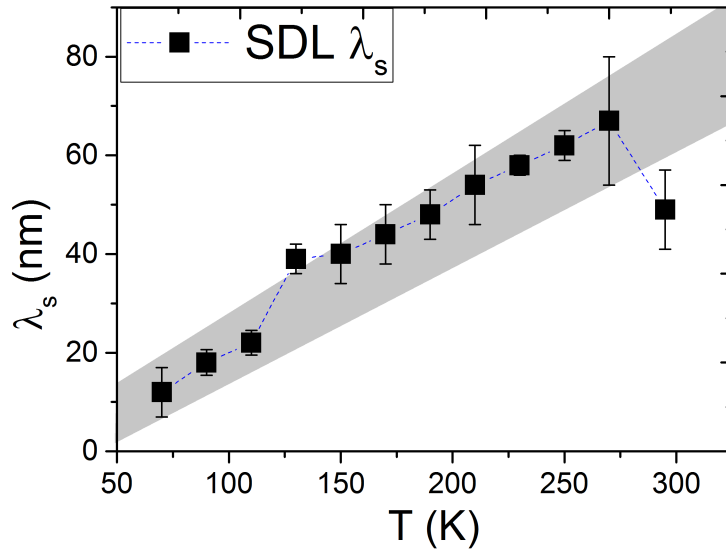
Figure 6.16 – The plots of the experimentally extracted λ_s as a function of T. The grey area represents the overall monotonic behavior of λ_s over T. The errors are estimated from the uncertainty in the measurements and also in the fits. Regarding the calculated parameters, the errors of the multi-variable functions are calculated based on the general rules presented here [182].

6.3.7. Spin Lifetime τ_s of PBTTT

The spin lifetime τ_s is calculated from $\tau_s = \lambda_s^2/D$. The diffusion coefficient D is calculated using Einstein relationships addressed in section 2.7.3. As stated there, two approaches are followed for calculating D. The first approach assumes the Einstein relation for thermally excited transport in nondegenerate semiconductors $D = \left(\frac{\mu k_B}{e}\right)T$. In this case, the diffusion of the spin carriers strongly depends on the temperature and charge carriers' mobility μ. Adopting this equation is valid because the carriers' mobility has a major influence on thermally excited transport [29, 30, 108]. In the second approach, D is calculated using the Einstein relation for hopping transport in highly-doped semiconductors (the degenerate case) which resembles metallic systems. D in this case is expressed as $D = \left(\frac{\sigma}{g(E_f)e^2}\right)$. Adopting this equation for calculating D in highly-doped PBTTT is valid for three reasons. First, PBTTT semiconductor is highly-doped with high conductivity and high carrier concentration. The conductivity in this doping regime is close to that of the conducting polymers' and it is several orders of magnitude higher than the conductivity of pristine PBTTT. Also, the carrier concentration is as high as that for highly-doped conducting polymers (e.g PEDOT:PSS). Second, although PBTTT does not have ideal metallic charge transport like that found in some organics like polyaniline [121], it does show some evidence of coherent charge transport in metallic grains at low temperature. Besides that, a clear Hall voltage signal was observed in a wide temperature range in this highly-doped PBTTT, providing evidence for some metallic behavior using the delocalized charge carriers [108]. Third, in highly-doped polymer with high carrier concentration where the carriers are located closer to each other, the exchange interaction between the neighboring spins becomes a

major factor for spin diffusion [30]. In this situation, the spin diffusion takes place between two adjacent polarons and the distance between the two is defined by the spin localization length ξ.

$g(E_f)$ is expressed as $\beta/[T_0\zeta^3 k_B]$. The characteristic temperature T_0 and the numerical constant β are calculated employing the VRH model described in section 2.7.3. Based on the explanation presented above, the spin lifetime τ_s will be calculated using D for both the degenerate and nondegenerate cases.

It is worth mentioning that the feasibility of using these two approaches will be determined according to the suitability of the calculated D with respect to the PBTTT characteristic parameters, (e.g μ, σ).

In the first approach, D is calculated employing μ data obtained from the Hall effect measurements performed on 40 nm PBTTT doped film which are reported here [108]. The resulting τ_s values calculated from D over temperature are plotted in figure 6.17a. As indicated in this figure, the maximum spin relaxation time τ_s is around ~ 1 ns near room temperature. On the other hand, for the degenerate case, the characteristic temperature of T_0 is calculated from the fit of the data in figure 6.9. The obtained characteristic temperature T_0 is 1360 K. The computed polaron localization length ζ along the $\pi-\pi$ stacking layers in PBTTT is found to be 0.4 nm from first principles [30]. Using these parameters, D values are calculated. Using the calculated D and the measured λ_s, the spin-flip time τ_s is calculated and the values over the whole temperature range are plotted in figure 6.17 b.
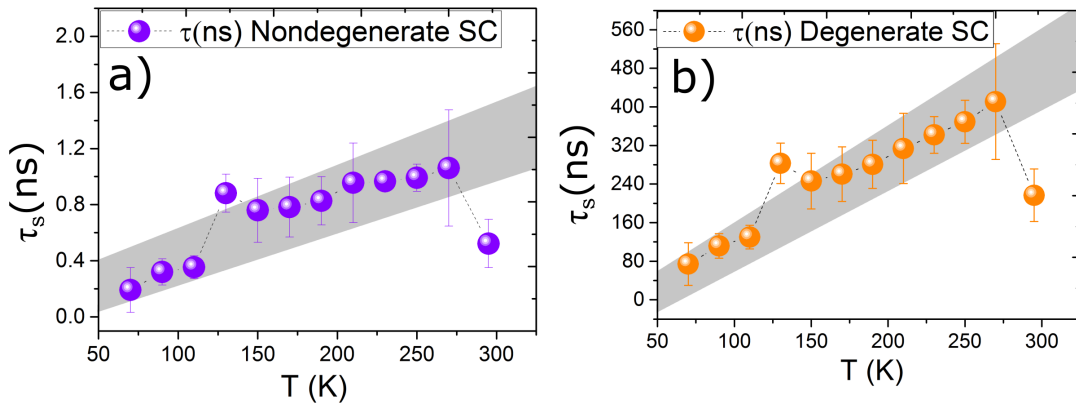
Figure 6.17 – (a-b) The plots of the experimentally calculated τ_s as a function of T in both, degenerate and nondegenerate semiconductors approaches, respectively. The grey area represents the overall monotonic change of τ_s over T. The errors are estimated based on the general roles for calculating the errors of the multi-variable functions presented in [182].

As shown in this figure, a maximum τ_s of around 400 ns is obtained in the range close to the room temperature. This high spin lifetime is an indication of low spin scattering probability which is consistent with many studies done on similar polymers [27, 29, 30, 105, 115]. The weak SOC provides a low spin-flip rate and the spins are conserved for a longer time throughout the polymer. On the other side, in high carrier density regime (10^{20} cm^3), the neighboring spins are located close to each other and their wavefunctions overlap and this creates an efficient pathway for the

transfer of spins between adjacent carriers which provides longer spin conservation time [30]. However, it is important to state that, due to the nature of the calculations involved in this approach which includes several parameters (calculated or measured from experiments), the error gradually increases, and eventually it becomes huge compared to the calculated D. Moreover, using the D obtained from the degenerate case to calculate the mobility will result in a value of less than μ value obtained from the experiments by 2 orders of magnitude. This may hinder using the degenerate approach for calculating D in organic semiconductors. One possible reason for this inconsistency with this approach here is using the in-plane conductivity σ_{IP} which is significantly different from the out-of-plane conductivity σ_{OOP}. Considering σ_{OOP} might be useful in this case because it describes the direction of the hopping spin transport through the polymer which also corresponds to the direction of the pumped spin current [105].

6.3.8. Spin Relaxation Mechanism in PBTTT

The monotonic change of τ_s with T can be understood within the mechanism that governs the spin relaxation. We know that EY and DP have an opposite proportionality with material conductivity σ. In EY mechanism $\tau_s \propto \tau_e \propto \sigma$ while in DP mechanism $\tau_s \propto 1/\sigma$. Based on the dependence of τ_s on T and the polymer conductivity obtained from the experiments, and referring to the discussion in section 2.7.4, the spin relaxation mechanism we expect to account for in our case is the Elliot-Yafet (EY) spin-orbit scattering. The observed dominance of EY is consistent with other studies that explore spin relaxation in similar materials, where spin-flip is caused by momentum relaxation due to phonon scattering [115, 117]. The probability of relaxation by spin precession due to DP is very small due to the weak SOC in this polymer. Also, like many πCPs, the effect of the HF interaction is not important in PBTTT due to the very weak HF coupling where the magnitude of the HF field amounts to 10 Oe [30].

In EY mechanism, the correlation between τ_s and the relaxation time of electron momentum τ_e is expressed as $\frac{1}{\tau_s} \simeq (\frac{L}{\Delta})^2 \frac{1}{\tau_e}$.

The spin relaxation here is caused by the spin-lattice relaxation via the coupling between the polymer backbone and the conduction electrons. So at high-T regime, we expect a high relaxation rate $1/\tau_s$ due to the high phonon-polaron scattering and vice versa. However, in many highly-doped polymers the spin relaxation rate may change differently with T due to the events the spin carrier experiences during the transport are linked to T differently from the case in the other SCs. These events link temperature to polymer-backbone characteristics and they include hopping, trapping and relaxing. As we know, the carrier transport in πCPs is dominated by the VRH process. The hopping rate is a thermally induced process where the number of hops scales with T as $n_{hop} \sim (k_0 t)^{T/T_0}$ [183, 184]. If we assume the spin relaxes mostly in the hopping events, then we expect the spin relaxation rate $1/\tau_s$ to be comparable to the carrier hopping rate $1/\tau_{hop}$. However, in highly-doped polymers it was found that the hopping length L_{hop} of the spin carrier is much shorter than the spin-flip length λ_s [30, 98, 105]. This means the spin-flip probability in the hopping event is very small and that the spin mostly is conserved in the hopping events. This can be explained by the spin-flip taking place in a trapping process

$1/\tau_{trap}$ which occurs after several hopping events. In this case the $1/\tau_{trap}=1/\tau_s$. This picture of the charge hopping and trapping is illustrated in figure 6.18a. More hops result in the reduction of the overall number of traps and thus the spin lifetimes last longer. Consequently, larger τ_s at high temperature is an indication that the spin relaxation takes place primarily during trapping events where in this case $n_{trap} <<$ n_{hop}. This assumption has taken into account the multiple hopping model (MH) which considers hop events to be correlated (Fig.6.18a) to differentiate it from the multiple trapping model (MT) which treats each hop event independently as a trap release event (uncorrelated hopping) [183]. Using the MT model is found to be inappropriate due to the existence of the correlation between the hopping events in highly-doped polymers [183]. One example is the correlation of the hopping to the configuration of cites. More specifically, two sites near each other may experience back and forth hopping before the carrier moves to another hop/trap site (Fig.6.18a). This case is induced in highly-doped polymers where the distance between hopping cites is reduced [99, 125]. This correlated hopping may be one of the reasons for the long spin lifetime in high doping regime where the $\pi - \pi$ intermolecular distance is reduced [99, 125] which induces this back-forth hopping transport involved in MH model. In this back-forth hopping between a small number of sites, the spins are nearly conserved.
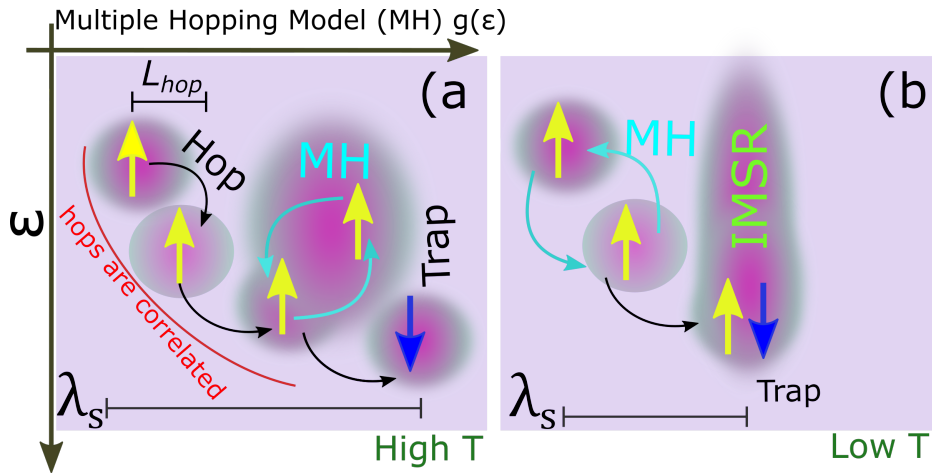
Figure 6.18 – Schematic of the expected spin transport and relaxation between different cites with different energies ε. (a) Spin flip in trapping event after several polaron hops. The multiple hopping model (MH) is illustrated here where the hops are correlated. (b) An illustration of the intramolecular spin relaxation (IMSR) which is dominant at low temperature.

This model addressed here presents a good explanation for the spin relaxation change with temperature in highly-doped PBTTT. In the high-T regime, the hopping rate $1/\tau_{hop}$ increase results in a reduction in the trapping rate $1/\tau_{trap}$ which leads to increasing τ_s. On the other side at low-T regime, the low $1/\tau_{hop}$ will result in increasing $1/\tau_{trap}$ which yields a small τ_s. This scenario explained above is consistent with the experimental result obtained here for λ_s of PBTTT. Considering the hopping length L_{hop} in highly-doped PBTTT is close to the value of the spin

localization length ξ [15], this results in L_{hop} that is two orders of magnitude smaller than the λ_s obtained experimentally. Furthermore, as shown in figure 6.17, τ_s increases monotonically with T which explains the major role of the trapping process in the spin relaxation. Regarding τ_s vs. σ change, as shown in figure 6.19a, τ_s is proportional to σ as expected from EY mechanism which reflects the dominance of this mechanism for the spin relaxation in PBTTT. The situation presented here for the trapping process inducing spin relaxation leads to an expected relation between the spin relaxation rate $1/\tau_s$ and the carriers mobility μ. This relation is attributed to the strong proportionality between carrier mobility and temperature [29, 30, 108]. At high-μ regimes, the spin-flip rate $1/\tau_s$ is expected to decrease. This is because, at high mobility, the spins are expected to conserved longer due to small $1/\tau_{trap}$. As a results, τ_s is expected to increase monotonically with μ. The change of τ_s with μ is shown in figure 6.19b, where μ values are measured at the same temperature values where τ_s is studied. The mobility data are taken from the results reported in [108].
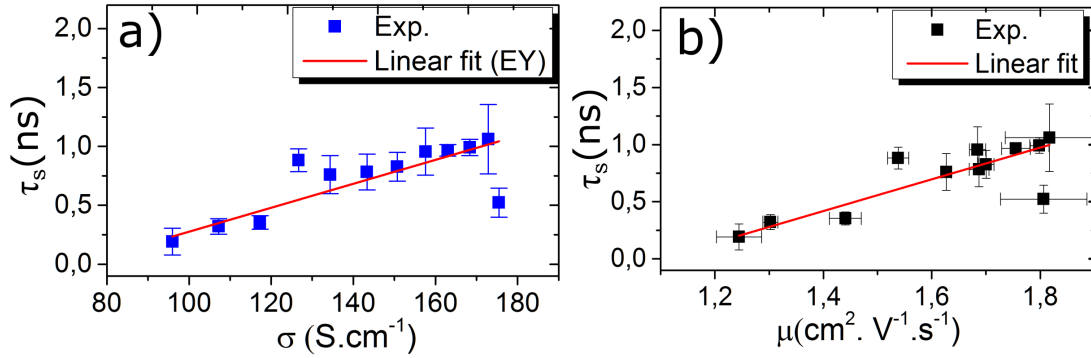
Figure 6.19 – EY spin relaxation mechanism in PBTTT. (a) The experimental results of τ_s plotted as a function of the associated PBTTT conductivity σ. The data are linearly fitted to match the behavior as dictated by the EY spin relaxation mechanism. (b) The change of τ_s vs. μ. The line shows the linear fit of the data as expected from the EY mechanism. τ_s values plotted here are the data of non-degenerate SC case.

As shown in figures 6.19b , τ_s increases with increasing μ which is consistent with the discussion above. Despite the consistency of τ_s change with T, σ, and μ with EY mechanism, there is a deviation from ideal EY behavior at large conductivity/large mobility values. This deviation may be interpreted by an impact of other parameters on the spin relaxation rather than those involved in EY mechanism. A possible explanation is the difference the conductivity changes with T in πCPs from that in metals. As we know in metals by varying σ with T, the carrier concentration does not change. However, in πCPs, both n and μ change with T. In such case, the change of τ_s with T, $[\frac{d\tau_s}{dT}]$ will be influenced by μ, n and T.

Eventually, the overall influence will be manifested in implicit and explicit way and it will be expressed as : $\frac{d\tau_s}{dT} = \frac{\partial \tau_s}{\partial T} + \frac{\partial \tau_s}{\partial \mu}\frac{d\mu}{dT} + \frac{\partial \tau_s}{\partial n}\frac{dn}{dT}$.

---

[15]The localization length ξ is linked to the hopping length L_{hop} by the relation $L_{hop} = [(9/8\pi\beta)(T_0/T)]^{1/4}\xi$ [105, 181]. The average hopping distance L_{hop} between polarons along the $\pi-\pi$ stacking direction in highly-doped PBTTT is around 0.45 nm [30]

Some studies have reported a contribution from the intramolecular spin relaxation (IMSR) in some organic materials, where IMSR is considered as a hopping independent mechanism [184, 185]. This mechanism is illustrated in figure 6.18b. IMSR is predominantly neglected in organics because the spin relaxation due to this mechanism is generally considered to be governed by the intermolecular motion of the charge carrier. This mechanism is not common in πCPs for the charge carrier transport. IMSR is found only to be significant in small-molecule semiconductors which have weak charge-carrier mobility where the relaxation occurs when charge carriers are residing on molecules. This scenario may become suitable for polymers in such circumstances where the charge-carrier mobility is very weak, corresponding to the low-T regimes in πCPs. In this case, the spin carrier resides longer in the localization state into the polymer molecule before escaping to another site. In our case with the highly-doped PBTTT, IMSR may explain the increase in $1/\tau_s$ at low T where μ is small as shown in figure 6.19b. More specifically, at low-T and then low-μ regimes, the long residence of the spin in the molecule at the trap event causes the spin to relax through IMSR mechanism. At last, we can conclude that the spins in highly-doped PBTTT are relaxed due to the EY mechanism via the trap-assisted spin-flip in combination with the IMSR process.

6.4. Summary

In this chapter, the existence of the spin-to-charge conversion in highly-doped πCP PBTTT was confirmed by detecting ISHE in several of YIG/PBTTT bilayer structures. Applying the experimental protocols established in the previous chapter for measuring ISHE in πCPs, we achieved systematic and intensive study for the ISHE in PBTTT. We expanded the scope of our study to include a wide temperature range starting from RT and down to 5 k. At RT, the ISHE was systematically investigated in samples with different polymer thicknesses and different doping ratios varied by our aforementioned dedoping process. The roles of the mobility and charge carrier concentration for the ISHE were also investigated by tuning conductivity which was achieved by varying temperature and doping ratio. We performed an ISHE thickness-dependence study at low temperatures which provided insight into the spin relaxation mechanisms in PBTTT. This study enabled us to extract some of the key parameters of the spin relaxation in highly-doped PBTTT, namely spin diffusion length and spin relaxation time. Our results indicate that the spin relaxation in PBTTT can be explained by EY mechanism. Besides that, the varying of the spin life-time with temperature indicates that the spin is more likely conserved in the hopping events and the spin flip occurs at the thermally reduced trapping events.

Chapter 7

7. Summary and Outlook

7.1. Summary

The main objectives of the present PhD-thesis were to study spin pumping and ISHE in πCPs, namely PEDOT:PSS and PBTTT. In order to give a conclusive overview of the main outlines of the chapters, for each chapter containing results and discussion, a summary is included at its end.

The key points drawn out from this thesis can be summarized as follows:

a)- **Radiation damping induced by a spin sink in FMR is a very sizable and important effect in spin pumping**.

• When ferromagnetic materials with very low damping like YIG are used for spin pumping experiments in FM/spin-sink bilayer, radiation damping α_{rad} becomes a major part of the total damping. Especially when a spin sink with low spin scattering and thus low damping enhancement like πCP is used, the radiation damping can be bigger than any damping stemming from the spin pumping itself.

• Radiation damping investigation in FMR, clearly demonstrated that studying spin pumping into low spin-flip-rate polymers by employing the damping enhancement is not feasible. Consequently, to calculate all spin-pumping related parameters, like spin pumping damping α_{sp}, SHA θ_{SH}, and spin mixing conductance $g^{\uparrow\downarrow}$, the correction introduced by α_{rad} must be considered.

b)- **The real ISHE in PEDOT:PSS exists and can be measured by employing an optimized geometry and eliminating artifacts**.

• The spin-charge conversion in highly doped πCP PEDOT:PSS has been confirmed. The investigation of ISHE in this polymer has shown that despite any previous claims, PEDOT:PSS exhibits a small but measurable ISHE which is in coarse agreement with theory.

• We developed geometry which enables us to eliminate the two artifacts originating from MSSW and spin pumping into the contacts. The remaining small signal can be attributed to the ISHE after subtracting the signal generated by the Nernst effect.

c)- **The spin-to-charge conversion in highly doped PBTTT is confirmed and the measured ISHV unveils some important parameters of the polymer**.

• Applying the experimental protocols established throughout the entire thesis for achieving accurate ISHE measurements in πCPs, we could measure a pure ISHE in PBTTT confirming the existence of the spin-to-charge conversion in this semiconducting polymer.

• When the polymer has a low doping ratio, the ISHV is no longer measurable. This indicates the spin current transport and ISHE in the polymer become less efficient in low doping regime.

• Our investigations for spin relaxation time with temperature reveal the spin relaxation in PBTTT can be explained by EY mechanism. Besides that, the varying of the spin life-time with temperature indicates that the spin is likely conserved in the hopping events and the spin likely flips during thermally-reduced trapping events.

d)- **With careful experiments and optimized sample geometries, very small effects (damping or ISHE) can be detected**.

Finally, the common denominator amongst all materials studied therein is that all measurements could not have been done correctly nor achieved without adopting three main things: systematic experiments with controls, careful measurements, and optimized samples' geometries. These three pillars might be less important in high SOC spin-sinks, but they are very critical in weak-SOC materials like πCPs.

7.2. Outlook

$\diamond$ Performing ISHE measurements to fully understand the effect of temperature and doping on ISHE requires extensive knowledge of their effect on the ISHE-characteristic parameters and also the interplay of these parameters to each other. To achieve that, further studies are still needed. However, performing ISHE is still not enough for obtaining all spin-pumping and ISHE related parameters of the polymer spin-sink.

$\diamond$ The full picture of the spin relaxation mechanism in highly-doped πCPs still requires the studying of the spin carrier diffusion in both directions, in-plane and out-of-plane. This is an important issue especially when it comes to the polymers with highly-anisotropic conductivity between the in-plane and out-of-plane directions, like PEDOT:PSS and PBTTT.

$\diamond$ ISHE is considered to be a practical way to convert magnetic information to electrical information. However, based on the weak spin-charge conversion efficiency observed in πCPs, employing ISHE in the organic spintronic applications is not yet feasible. For this reason, more studies are needed to increase this efficiency. Once this goal is reached this mechanism might find use in future organic electronic and spintronics devices.

Appendices

Appendix A

A. FMR Mode Fit with Kittel Equation

All samples studied in chapter 4 are measured at the FMR mode (uniform mode). This is confirmed by fitting the FMR mode with Kittel equation - in the in-plane configuration - which describes the relation between the resonance field H_{FMR} and the exciting microwave frequency f_{rf}.

The plots of f vs. H_{FMR} of all samples are shown in figure A.1.
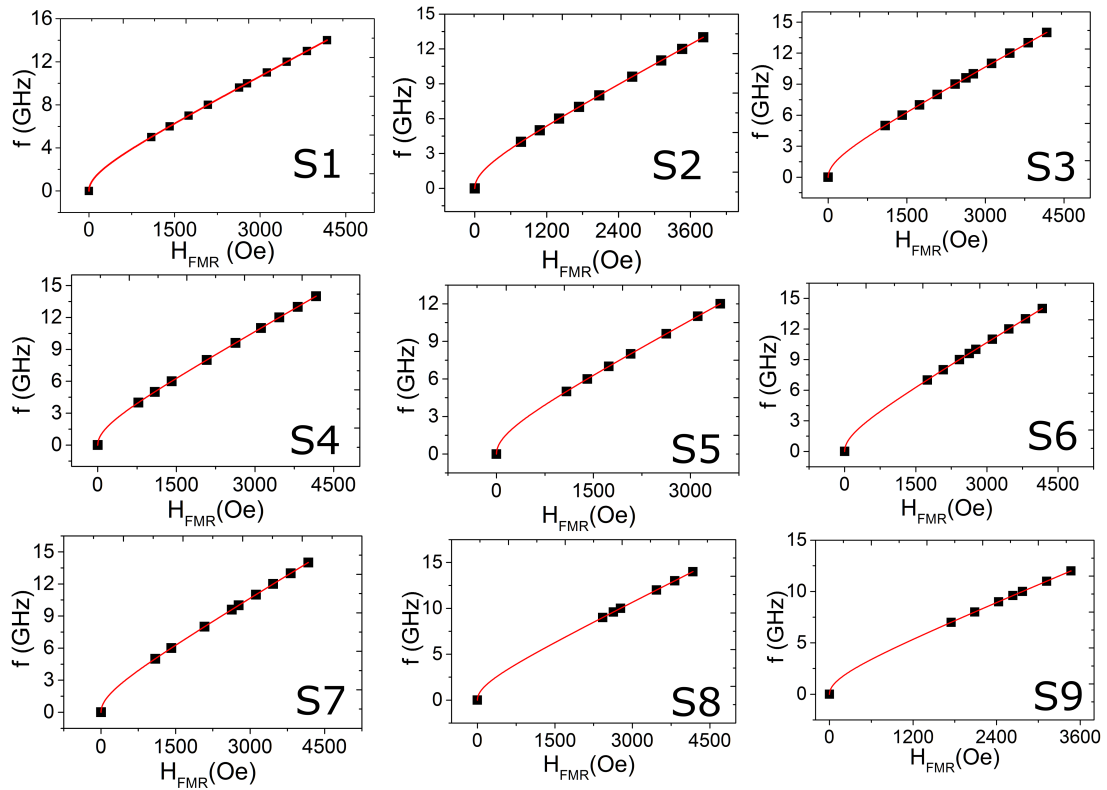
Figure A.1 – Resonance field H_{FMR} as a function of exciting rf frequency fitted due to Kittel equation.

The values of γ and $4\pi M_{eff}$ extracted from the fits are listed in table 8 for all samples S1-S9.

Table 8 – The values of γ and $4\pi M_{eff}$ extracted from the fitted experimental curves plotted in figure A.1.

Sample	Structure	γ (MHz/Oe)	$4\pi M_{eff}$ (Oe)
S1	YIG	2.8	1842±6
S2	YIG/PEDOT:PSS	2.79	1876±5
S3	YIG/Pt	2.79	1858±4
S4	YIG/Al_2O_3	2.79	1859±3
S5	YIG/Al_2O_3/PEDOT:PSS	2.79	1878±3
S6	YIG/Al_2O_3/Pt5	2.79	1858±4
S7	YIG/Al_2O_3/Pt10	2.8	1837±7
S8	YIG/Al_2O_3/Pt15	2.79	1851±7
S9	YIG/Al_2O_3/Pt20	2.8	1822±5

Appendix B

B. Cleaning Procedures of YIG Surface

The cleaning procedures performed on YIG surface are done using organic solvents and piranha. The pre-cleaning steps with organic solvents are done in the following order :-

1- 10 min with acetone in ultrasonic bath.

2- 10 min with IPA in ultrasonic bath.

3- 10 min with MIBK or NEP in ultrasonic bath.

4- 10 min with IPA in ultrasonic bath.

5- Rinsing with IPA followed by quick drying in N_2 flow.

For piranha cleaning procedure we used, a mixture of ($H_2O_2, 98\%$ and $H_2SO_4, 30\%$) in ratio 1:4 in volume for 10 min. This procedure is followed by rinsing in deionized water for 10 min and drying in N_2 flow.

Appendix C

C. Creating YIG Stripe with Smooth Edges

YIG strip is made by Ar-ion etching employing Al foil as a shadow mask, figure C.1a. The reason for choosing this shadow mask instead of using photoresist mask made by optical lithography, is to get a smooth transition between YIG and GGG at the stripe edges and hence to avoid sharp edges. The sharp edges cause discontinuity in the polymer layer during spin coating.

Figure C.1b shows a microscopic image of the resulted YIG stripe from Ar-ion etching process. The smooth edges are demonstrated by the surface profile measured by Dektak for the YIG stripe-edge area, figure C.1c.

The smooth transition from YIG stripe to GGG at the edge area is clear in this figure. From the surface profile, the calculated inclination (tilt) angle of the stripe edge is around 0.27^o.
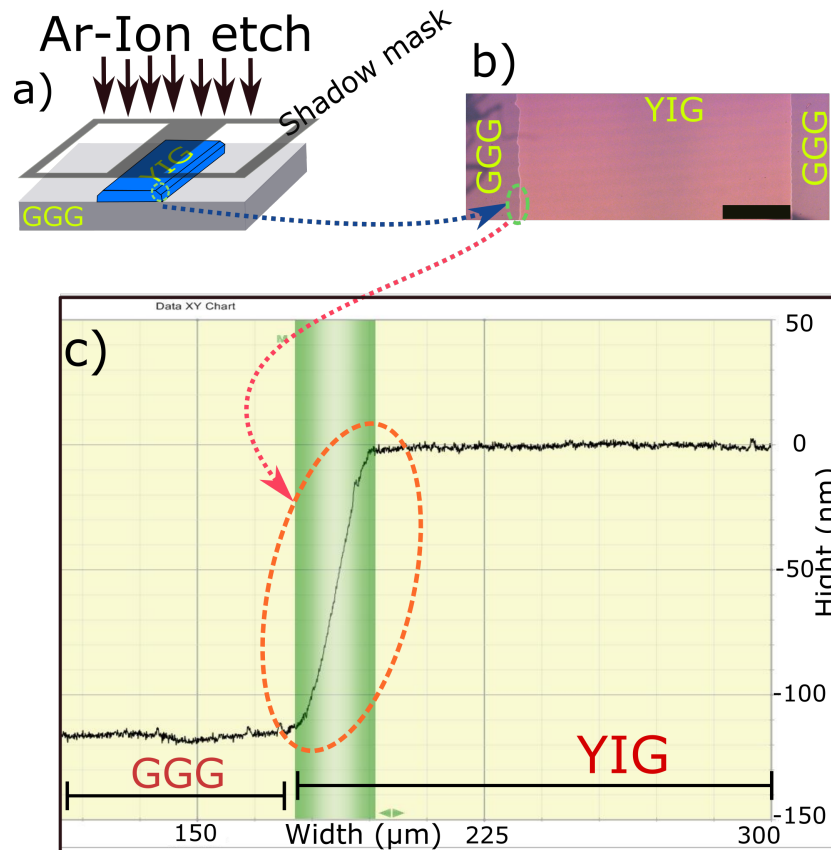
Figure C.1 – Dektak profile of the smooth edges of YIG stripe. (a) Schematic of the Ar-ion etching used to create YIG stripe using a shadow mask. (b) Microscopic image of the resulting YIG stripe. The scale bar is 500 μm. (c) The surface profile measured by Dektak for the YIG stripe indicating the smooth edge of the resulting YIG stripe. The arrows from a to c highlight the position of the strip edge.

Appendix D

D. The Numerical Calculations Model of the ISHE in PEDOT:PSS

For numerical calculations, a system which includes more than 10000 sites arranged on a cubic mesh is considered. Hopping between any pairs and triads of sites within a cutoff distance is taken into account. With parameters taken from literature, the electrical conductivity is obtained by applying a small bias, within the linear response regime, across the x or y direction.

First, the voltage drop along the x or y direction is obtained using

$$\sum_j g_{ij}(V_i^{x/y} - V_j^{x/y})^2 = 0, \tag{D.1}$$

where the conductance between site i and j is defined as

$$g_{ij} = \nu e^{-2\alpha|R_i - R_j|} e^{-(\beta/2)(|\epsilon_i| + |\epsilon_j| + |\epsilon_j - \epsilon_i|)} \tag{D.2}$$

and $V_i^{x/y}$ are the potentials. The parameters ϵ, $|R_i - R_j|$, α and ν are the site energies, the intersite separation, the decay constant of the localized wave functions and the phonon frequency, respectively. The electrical conductivity is calculated by

$$\sigma_{x/y} = \frac{1}{2\Omega E^2} \sum_j g_{ij}(V_i^{x/y} - V_j^{x/y})^2. \tag{D.3}$$

with Ω being the volume of the system. The spin Hall conductivity is obtained via $\sigma_{sh} = J_s^y/E^x$ with J_s^y the spin current along y direction when the electric field E^x is applied along the x direction. The spin Hall conductivity can be written as

$$\sigma_{sh} = -\frac{e^2\beta}{6\Omega E^2} \sum_j W_{ijk}^z(V_{ij}^x V_{jk}^y - V_{ij}^y V_{jk}^x), \tag{D.4}$$

where the hopping probability via an intermediate site is

$$W_{ijk}^z = \frac{\lambda N_{ijk}^z}{V_0} \hbar \nu^2 e^{-\alpha(R_{ij} + R_{jk} + R_{ki})} \left[e^{-(\beta/2)(|\epsilon_j| + |\epsilon_k| + |\epsilon_j - \epsilon_i| + |\epsilon_k - \epsilon_i|)} + i \rightleftharpoons j + i \rightleftharpoons k \right]. \tag{D.5}$$

The spin Hall angle is determined as $\Theta_{sh} = \sigma_{sh}/(\sigma_{xx}\sigma_{yy})^{1/2}$ with σ_{xx} and σ_{yy} as the electrical conductivity along the x and y directions, respectively. In order to ensure that the results are not the artefact of an ordered cubic mesh (not applicable for semi-crystalline or disordered organics), we allow for a spatial disorder by altering the distance between any pair of sites randomly in all directions by up to 15% of its original distance. The results for the spin Hall conductivity and the spin Hall angle are plotted in figure 5.10. The parameters are $\alpha = 2$, $\lambda = 10^{-3}$, $\nu = 10^{11}$ s^{-1} and $V_0 = 0.1$ eV. The transport results are consistent with variable range hopping behavior, over a temperature range [40, 320] K, as expected.

References

[1] M. N. Baibich, J. M. Broto, A. Fert, *et al.*, "Giant magnetoresistance of (001)Fe/(001)Cr magnetic superlattices", *Physical review letters*, vol. 61, no. 21, p. 2472, 1988.

[2] G. Binasch, P. Grünberg, F Saurenbach, and W Zinn, "Enhanced magnetoresistance in layered magnetic structures with antiferromagnetic interlayer exchange", *Physical review B*, vol. 39, no. 7, p. 4828, 1989.

[3] V Dediu, M Murgia, F. Matacotta, C Taliani, and S Barbanera, "Room temperature spin polarized injection in organic semiconductor", *Solid State Communications*, vol. 122, no. 3-4, pp. 181–184, 2002.

[4] Z. Xiong, D. Wu, Z. V. Vardeny, and J. Shi, "Giant magnetoresistance in organic spin-valves", *Nature*, vol. 427, no. 6977, p. 821, 2004.

[5] S Mizukami, Y Ando, and T Miyazaki, "Ferromagnetic resonance linewidth for nm/80nife/nm films (nm= cu, ta, pd and pt)", *Journal of magnetism and magnetic materials*, vol. 226, pp. 1640–1642, 2001.

[6] S. Mizukami, Y. Ando, and T. Miyazaki, "The study on ferromagnetic resonance linewidth for nm/80nife/nm (nm= cu, ta, pd and pt) films", *Japanese journal of applied physics*, vol. 40, no. 2R, p. 580, 2001.

[7] E Saitoh, M Ueda, H Miyajima, and G Tatara, "Conversion of spin current into charge current at room temperature: Inverse spin-Hall effect", *Applied physics letters*, vol. 88, no. 18, p. 182 509, 2006.

[8] M. M. Qaid, T. Richter, A. Müller, C. Hauser, C. Ballani, and G. Schmidt, "Radiation damping in ferromagnetic resonance induced by a conducting spin sink", *Physical Review B*, vol. 96, no. 18, p. 184 405, 2017.

[9] M Haertinger, C. Back, J Lotze, *et al.*, "Spin pumping in YIG/Pt bilayers as a function of layer thickness", *Physical Review B*, vol. 92, no. 5, p. 054 437, 2015.

[10] Y. Tserkovnyak, A. Brataas, G. E. Bauer, and B. I. Halperin, "Nonlocal magnetization dynamics in ferromagnetic heterostructures", *Reviews of Modern Physics*, vol. 77, no. 4, p. 1375, 2005.

[11] Y. Tserkovnyak, A. Brataas, and G. E. W. Bauer, "Enhanced gilbert damping in thin ferromagnetic films", *Phys. Rev. Lett.*, vol. 88, p. 117 601, 11 2002.

[12] C. Du, H. Wang, P. C. Hammel, and F. Yang, "$Y_3Fe_5O_{12}$ spin pumping for quantitative understanding of pure spin transport and spin Hall effect in a broad range of materials", *Journal of Applied Physics*, vol. 117, no. 17, p. 172 603, 2015.

[13] I. Žutić, J. Fabian, and S. D. Sarma, "Spintronics: Fundamentals and applications", *Reviews of modern physics*, vol. 76, no. 2, p. 323, 2004.

[14] R Urban, G. Woltersdorf, and B Heinrich, "Gilbert damping in single and multilayer ultrathin films: Role of interfaces in nonlocal spin dynamics", *Physical review letters*, vol. 87, no. 21, p. 217 204, 2001.

[15] K Uchida, S Takahashi, K Harii, *et al.*, "Observation of the spin Seebeck effect", *Nature*, vol. 455, no. 7214, p. 778, 2008.

[16] J. Xiao, G. E. Bauer, K.-C. Uchida, E. Saitoh, S. Maekawa, *et al.*, "Theory of magnon-driven spin Seebeck effect", *Physical Review B*, vol. 81, no. 21, p. 214 418, 2010.

[17] K.-i. Uchida, H. Adachi, T. Ota, H. Nakayama, S. Maekawa, and E. Saitoh, "Observation of longitudinal spin-Seebeck effect in magnetic insulators", *Applied Physics Letters*, vol. 97, no. 17, p. 172 505, 2010.

[18] H. Wang, C. Du, Y Pu, R Adur, P. C. Hammel, and F. Yang, "Scaling of spin Hall angle in 3d, 4d, and 5d metals from $Y_3Fe_5O_{12}$/metal spin pumping", *Physical review letters*, vol. 112, no. 19, p. 197 201, 2014.

[19] Y. Sun and M. Wu, "Yttrium iron garnet nano films: Epitaxial growth, spin-pumping efficiency, and Pt-capping-caused damping", in *Solid State Physics*, vol. 64, Elsevier, 2013, pp. 157–191.

[20] K. Ando, S. Takahashi, J. Ieda, *et al.*, "Inverse spin-Hall effect induced by spin pumping in metallic system", *Journal of applied physics*, vol. 109, no. 10, p. 103 913, 2011.

[21] M. Obstbaum, "Inverse spin Hall effect in metallic heterostructures", PhD thesis, 2016.

[22] Z Qiu, M Uruichi, D Hou, K Uchida, H. Yamamoto, and E Saitoh, "Spin-current injection and detection in κ-(BEDT-TTF)$_2$Cu[N(CN)$_2$]Br", *AIP Advances*, vol. 5, no. 5, p. 057 167, 2015.

[23] D. Sun, K. J. van Schooten, M. Kavand, *et al.*, "Inverse spin Hall effect from pulsed spin current in organic semiconductors with tunable spin–orbit coupling", *Nature materials*, vol. 15, no. 8, p. 863, 2016.

[24] X. Tao, Q. Liu, B. Miao, *et al.*, "Self-consistent determination of spin Hall angle and spin diffusion length in Pt and Pd: The role of the interface spin loss", *Science Advances*, vol. 4, no. 6, eaat1670, 2018.

[25] K. Ando and E Saitoh, "Inverse spin-Hall effect in palladium at room temperature", *Journal of Applied Physics*, vol. 108, no. 11, p. 113 925, 2010.

[26] O Mosendz, V Vlaminck, J. Pearson, F. Fradin, G. Bauer, S. Bader, and A Hoffmann, "Detection and quantification of inverse spin Hall effect from spin pumping in permalloy/normal metal bilayers", *Physical Review B*, vol. 82, no. 21, p. 214 403, 2010.

[27] K. Ando, S. Watanabe, S. Mooser, E. Saitoh, and H. Sirringhaus, "Solution-processed organic spin–charge converter", *Nature materials*, vol. 12, no. 7, p. 622, 2013.

[28] P Wang, L. Zhou, S. Jiang, Z. Luan, D. Shu, H. Ding, and D Wu, "Unidirectional spin-wave-propagation-induced Seebeck voltage in a PEDO:PSS/YIG bilayer", *Physical review letters*, vol. 120, no. 4, p. 047 201, 2018.

[29] S. Watanabe, K. Ando, K. Kang, *et al.*, "Polaron spin current transport in organic semiconductors", *Nature Physics*, vol. 10, no. 4, p. 308, 2014.

[30] S.-J. Wang, D. Venkateshvaran, M. Mahani, *et al.*, "Long spin diffusion lengths in doped conjugated polymers due to enhanced exchange coupling", *Nature Electronics*, vol. 2, no. 3, p. 98, 2019.

[31] D. Sun, Y. Zhai, K. J. van Schooten, *et al.*, "Sign reversal of magnetoresistance and inverse spin Hall effect in doped conducting polymers", *Journal of Physics: Condensed Matter*, vol. 30, no. 48, p. 484 003, 2018.

[32] J. M. Coey, *Magnetism and magnetic materials*. Cambridge university press, 2010.

[33] B. Heinrich and J. A. C. Bland, *Ultrathin magnetic structures II: Measurement techniques and novel magnetic properties*. Springer Science & Business Media, 2006, vol. 2.

[34] T. Laursen and J. Simo, "A continuum-based finite element formulation for the implicit solution of multibody, large deformation-frictional contact problems", *International Journal for numerical methods in engineering*, vol. 36, no. 20, pp. 3451–3485, 1993.

[35] L. D. Landau and E Lifshitz, "On the theory of the dispersion of magnetic permeability in ferromagnetic bodies", *Phys. Z. Sowjet.*, vol. 8, p. 153, 1935.

[36] T. L. Gilbert, "A lagrangian formulation of the gyromagnetic equation of the magnetization field", *Phys. Rev.*, vol. 100, p. 1243, 1955.

[37] Z Celinski, K. Urquhart, and B Heinrich, "Using ferromagnetic resonance to measure the magnetic moments of ultrathin films", *Journal of Magnetism and Magnetic Materials*, vol. 166, no. 1-2, pp. 6–26, 1997.

[38] E. Montoya, T. McKinnon, A. Zamani, E. Girt, and B. Heinrich, "Broadband ferromagnetic resonance system and methods for ultrathin magnetic films", *Journal of Magnetism and Magnetic Materials*, vol. 356, pp. 12–20, 2014.

[39] B Heinrich and J. Cochran, "Ultrathin metallic magnetic films: Magnetic anisotropies and exchange interactions", *Advances in Physics*, vol. 42, no. 5, pp. 523–639, 1993.

[40] B Heinrich, J. Cochran, A. Arrott, S. Purcell, K. Urquhart, J. Dutcher, and W. Egelhoff, "Development of magnetic anisotropies in ultrathin epitaxial films of Fe (001) and Ni (001)", *Applied Physics A*, vol. 49, no. 5, pp. 473–490, 1989.

[41] J. Griffiths, "Anomalous high-frequency resistance of ferromagnetic metals", *Nature*, vol. 158, no. 4019, p. 670, 1946.

[42] E Zavoisky, "Spin magnetic resonance in the decimetre-wave region", *J. Phys. USSR*, vol. 10, p. 197, 1946.

[43] M. Farle, "Ferromagnetic resonance of ultrathin metallic layers", *Reports on Progress in Physics*, vol. 61, no. 7, p. 755, 1998.

[44] C. Kittel, P. McEuen, and P. McEuen, *Introduction to solid state physics*. Wiley New York, 1976, vol. 8.

[45] S Azzawi, A. Hindmarch, and D Atkinson, "Magnetic damping phenomena in ferromagnetic thin-films and multilayers", *Journal of Physics D: Applied Physics*, vol. 50, no. 47, p. 473 001, 2017.

[46] S. Rezende, R. Rodríguez-Suárez, and A Azevedo, "Magnetic relaxation due to spin pumping in thick ferromagnetic films in contact with normal metals", *Physical Review B*, vol. 88, no. 1, p. 014 404, 2013.

[47] B Heinrich, R Urban, and G. Woltersdorf, "Magnetic relaxation in metallic films: Single and multilayer structures", *Journal of applied physics*, vol. 91, no. 10, pp. 7523–7525, 2002.

[48] J. Lock, "Eddy current damping in thin metallic ferromagnetic films", *British Journal of Applied Physics*, vol. 17, no. 12, p. 1645, 1966.

[49] V. Flovik, F. Macià, A. D. Kent, and E. Wahlström, "Eddy current interactions in a ferromagnet-normal metal bilayer structure, and its impact on ferromagnetic resonance lineshapes", *Journal of Applied Physics*, vol. 117, no. 14, p. 143 902, 2015.

[50] P. Pincus, "Excitation of spin waves in ferromagnets: Eddy current and boundary condition effects", *Phys. Rev.*, vol. 118, pp. 658–664, 3 1960.

[51] A. Prabhakar and D. D. Stancil, *Spin waves: Theory and applications*. Springer, 2009.

[52] G. Woltersdorf, "Spin-pumping and two-magnon scattering in magnetic multilayers", PhD thesis, Sinon Fraser University, 2004.

[53] H. Suhl, "Theory of the magnetic damping constant", *IEEE Transactions on Magnetics*, vol. 34, no. 4, pp. 1834–1838, 1998.

[54] S. Jiang, L. Sun, Y. Yin, Y. Fu, C. Luo, Y. Zhai, and H. Zhai, "Ferromagnetic resonance linewidth and two-magnon scattering in fe1-x gd x thin films", *AIP Advances*, vol. 7, no. 5, p. 056 029, 2017.

[55] I. Žutić, A. Matos-Abiague, B. Scharf, H. Dery, and K. Belashchenko, "Proximitized materials", *Materials Today*, 2018.

[56] Y. Tserkovnyak, A. Brataas, and G. E. Bauer, "Spin pumping and magnetization dynamics in metallic multilayers", *Physical Review B*, vol. 66, no. 22, p. 224 403, 2002.

[57] Y Kajiwara, K Harii, S Takahashi, *et al.*, "Transmission of electrical signals by spin-wave interconversion in a magnetic insulator", *Nature*, vol. 464, no. 7286, p. 262, 2010.

[58] O Mosendz, J. Pearson, F. Fradin, G. Bauer, S. Bader, and A Hoffmann, "Quantifying spin Hall angles from spin pumping: Experiments and theory", *Physical review letters*, vol. 104, no. 4, p. 046 601, 2010.

[59] F. D. Czeschka, "Spin currents in metallic nanostructures", PhD thesis, Technische Universität München, 2011.

[60] P. Brouwer, "Scattering approach to parametric pumping", *Physical Review B*, vol. 58, no. 16, R10135, 1998.

[61]   A. Brataas, Y. V. Nazarov, and G. E. Bauer, "Spin-transport in multi-terminal normal metal-ferromagnet systems with non-collinear magnetizations", *The European Physical Journal B-Condensed Matter and Complex Systems*, vol. 22, no. 1, pp. 99–110, 2001.

[62]   T. Shinjo, *Nanomagnetism and spintronics*. Elsevier, 2013.

[63]   W. Naber, S Faez, and W. G. van der Wiel, "Organic spintronics", *Journal of Physics D: Applied Physics*, vol. 40, no. 12, R205, 2007.

[64]   K. Shanavas, Z. S. Popović, and S Satpathy, "Theoretical model for rashba spin-orbit interaction in d electrons", *Physical Review B*, vol. 90, no. 16, p. 165 108, 2014.

[65]   N. F. Mott, "The scattering of fast electrons by atomic nuclei", *Proceedings of the Royal Society of London. Series A, Containing Papers of a Mathematical and Physical Character*, vol. 124, no. 794, pp. 425–442, 1929.

[66]   J. Smit, "The spontaneous Hall effect in ferromagnetics II", *Physica*, vol. 24, no. 1-5, pp. 39–51, 1958.

[67]   A. Hoffmann, "Spin Hall effects in metals", *IEEE transactions on magnetics*, vol. 49, no. 10, pp. 5172–5193, 2013.

[68]   L Berger, "Side-jump mechanism for the Hall effect of ferromagnets", *Physical Review B*, vol. 2, no. 11, p. 4559, 1970.

[69]   N. Nagaosa, J. Sinova, S. Onoda, A. H. MacDonald, and N. P. Ong, "Anomalous Hall effect", *Reviews of modern physics*, vol. 82, no. 2, p. 1539, 2010.

[70]   P. Noel, "Dynamical spin injection and spin to charge current conversion in oxide-based rashba interfaces and topological insulators", PhD thesis, Université Grenoble Alpes, 2019.

[71]   M. Dyakonov and V. Perel, "Current-induced spin orientation of electrons in semiconductors", *Physics Letters A*, vol. 35, no. 6, pp. 459–460, 1971.

[72]   J. Hirsch, "Spin Hall effect", *Physical Review Letters*, vol. 83, no. 9, p. 1834, 1999.

[73]   S. O. Valenzuela and M Tinkham, "Direct electronic measurement of the spin Hall effect", *Nature*, vol. 442, no. 7099, p. 176, 2006.

[74]   W. Y. Choi, H.-j. Kim, J. Chang, S. H. Han, H. C. Koo, and M. Johnson, "Electrical detection of coherent spin precession using the ballistic intrinsic spin Hall effect", *Nature nanotechnology*, vol. 10, no. 8, p. 666, 2015.

[75]   S. Valenzuela and M Tinkham, "Electrical detection of spin currents: The spin-current induced Hall effect", *Journal of applied physics*, vol. 101, no. 9, 09B103, 2007.

[76]   S Huh, H Koo, J Eom, J Chang, and S Han, "Electrical detection of spin Hall effect in a two-dimensional electron gas", in *2006 IEEE International Magnetics Conference (INTERMAG)*, IEEE, 2006, pp. 125–125.

[77]   M. Ehlert, C. Song, M. Ciorga, *et al.*, "All-electrical detection of spin Hall effect in semiconductors", *physica status solidi (b)*, vol. 251, no. 9, pp. 1725–1735, 2014.

[78] Y. K. Kato, R. C. Myers, A. C. Gossard, and D. D. Awschalom, "Observation of the spin Hall effect in semiconductors", *science*, vol. 306, no. 5703, pp. 1910–1913, 2004.

[79] J. Wunderlich, B. Kaestner, J. Sinova, and T. Jungwirth, "Experimental observation of the spin-Hall effect in a two-dimensional spin-orbit coupled semiconductor system", *Physical review letters*, vol. 94, no. 4, p. 047 204, 2005.

[80] K. Ando, T Yoshino, and E Saitoh, "Optimum condition for spin-current generation from magnetization precession in thin film systems", *Applied Physics Letters*, vol. 94, no. 15, p. 152 509, 2009.

[81] V. Kruglyak, S. Demokritov, and D Grundler, "Magnonics", *Journal of Physics D: Applied Physics*, vol. 43, no. 26, p. 264 001, 2010.

[82] T Holstein and H. Primakoff, "Field dependence of the intrinsic domain magnetization of a ferromagnet", *Physical Review*, vol. 58, no. 12, p. 1098, 1940.

[83] F. J. Dyson, "General theory of spin-wave interactions", *Physical review*, vol. 102, no. 5, p. 1217, 1956.

[84] B. Hillebrands, *Magnetization Dynamics I: Fundamentals of spin dynamics and Brillouin light scattering*. IEEE Magnetics Society Summer School, 2015.

[85] A. Serga, A. Chumak, and B Hillebrands, "YIG magnonics", *Journal of Physics D: Applied Physics*, vol. 43, no. 26, p. 264 002, 2010.

[86] C. Sandweg, Y Kajiwara, K. Ando, E Saitoh, and B Hillebrands, "Enhancement of the spin pumping efficiency by spin wave mode selection", *Applied Physics Letters*, vol. 97, no. 25, p. 252 504, 2010.

[87] R Iguchi, K. Ando, Z Qiu, T An, E Saitoh, and T. Sato, "Spin pumping by nonreciprocal spin waves under local excitation", *Applied Physics Letters*, vol. 102, no. 2, p. 022 406, 2013.

[88] S. Manuilov, C. Du, R Adur, H. Wang, V. Bhallamudi, F. Yang, and P. C. Hammel, "Spin pumping from spinwaves in thin film YIG", *Applied Physics Letters*, vol. 107, no. 4, p. 042 405, 2015.

[89] M. Balinsky, M. Ranjbar, M. Haidar, *et al.*, "Spin pumping and the inverse spin-Hall effect via magnetostatic surface spin-wave modes in Yttrium-iron garnet/platinum bilayers", *IEEE Magnetics Letters*, vol. 6, pp. 1–4, 2015.

[90] T An, V. Vasyuchka, K Uchida, *et al.*, "Unidirectional spin-wave heat conveyer", *Nature materials*, vol. 12, no. 6, p. 549, 2013.

[91] O. Wid, J. Bauer, A. Müller, O. Breitenstein, S. S. Parkin, and G. Schmidt, "Investigation of the unidirectional spin heat conveyer effect in a 200 nm thin Yttrium iron garnet film", *Scientific reports*, vol. 6, p. 28 233, 2016.

[92] O. Wid, J. Bauer, A. Mueller, O. Breitenstein, S. S. Parkin, and G. Schmidt, "Investigation of non-reciprocal magnon propagation using lock-in thermography", *Journal of Physics D: Applied Physics*, vol. 50, no. 13, p. 134 001, 2017.

[93]   G.-H. Kim, L. Shao, K. Zhang, and K. P. Pipe, "Engineered doping of organic semiconductors for enhanced thermoelectric efficiency", *Nature materials*, vol. 12, no. 8, p. 719, 2013.

[94]   K Kang, S Schott, D Venkateshvaran, *et al.*, "Investigation of the thermoelectric response in conducting polymers doped by solid-state diffusion", *Materials Today Physics*, vol. 8, pp. 112–122, 2019.

[95]   M. Teferi, J Ogle, G Joshi, *et al.*, "Tuning effective hyperfine fields in PEDO:PSS thin films by doping", *Physical Review B*, vol. 98, no. 24, p. 241 201, 2018.

[96]   H. M. McConnell, "Indirect hyperfine interactions in the paramagnetic resonance spectra of aromatic free radicals", *The Journal of Chemical Physics*, vol. 24, no. 4, pp. 764–766, 1956.

[97]   W.-P. Su, J. Schrieffer, and A. Heeger, "Soliton excitations in polyacetylene", *Physical Review B*, vol. 22, no. 4, p. 2099, 1980.

[98]   Z. Yu, "Spin-orbit coupling and its effects in organic solids", *Physical Review B*, vol. 85, no. 11, p. 115 201, 2012.

[99]   C. M. Palumbiny, F. Liu, T. P. Russell, A. Hexemer, C. Wang, and P. Müller-Buschbaum, "The crystallization of PEDO:PSS polymeric electrodes probed in situ during printing", *Advanced materials*, vol. 27, no. 22, pp. 3391–3397, 2015.

[100]   L. Landau, "Über die bewegung der elektronen in kristallgitter", *Phys. Z. Sowjetunion*, vol. 3, pp. 644–645, 1933.

[101]   W. H. Sio, C. Verdi, S. Poncé, and F. Giustino, "Polarons from first principles, without supercells", *Physical Review Letters*, vol. 122, no. 24, p. 246 403, 2019.

[102]   W. H. Sio, C. Verdi, S. Poncé, and F. Giustino, "Ab initio theory of polarons: Formalism and applications", *Physical Review B*, vol. 99, no. 23, p. 235 139, 2019.

[103]   N. Mott, "Electrons in glass", *Contemporary Physics*, vol. 18, no. 3, pp. 225–245, 1977.

[104]   A. Efros and B. I. Shklovskii, "Coulomb gap and low temperature conductivity of disordered systems", *Journal of Physics C: Solid State Physics*, vol. 8, no. 4, p. L49, 1975.

[105]   M. Kimata, D. Nozaki, Y. Niimi, H. Tajima, and Y. Otani, "Spin relaxation mechanism in a highly doped organic polymer film", *Physical Review B*, vol. 91, no. 22, p. 224 422, 2015.

[106]   A. M. Nardes, M. Kemerink, R. A. Janssen, *et al.*, "Microscopic understanding of the anisotropic conductivity of PEDO:PSS thin films", *Advanced Materials*, vol. 19, no. 9, pp. 1196–1200, 2007.

[107]   A. Nardes, M Kemerink, and R. Janssen, "Anisotropic hopping conduction in spin-coated PEDO:PSS thin films", *Physical Review B*, vol. 76, no. 8, p. 085 208, 2007.

[108] K. Kang, S. Watanabe, K. Broch, *et al.*, "2d coherent charge transport in highly ordered conducting polymers doped by solid state diffusion", *Nature materials*, vol. 15, no. 8, p. 896, 2016.

[109] T. V. de Oliveira, M. Gobbi, J. M. Porro, L. E. Hueso, and A. M. Bittner, "Charge and spin transport in PEDO:PSS nanoscale lateral devices", *Nanotechnology*, vol. 24, no. 47, p. 475 201, 2013.

[110] R. J Elliott, "Theory of the effect of spin-orbit coupling on magnetic resonance in some semiconductors", *Physical Review*, vol. 96, no. 2, p. 266, 1954.

[111] M. D'yakonov, "Spin orientation of electrons associated with the interband absorption of light in semiconductors", *Sov. Phys. JETP*, vol. 33, no. 5, pp. 1053–1059, 1971.

[112] G. Bir, A. Aronov, and G. Pikus, "Spin relaxation of electrons due to scattering by holes", *Soviet Journal of Experimental and Theoretical Physics*, vol. 42, p. 705, 1976.

[113] A. Abragam and A. Abragam, *The principles of nuclear magnetism*, 32. Oxford university press, 1961.

[114] S. Sanvito, "Molecular spintronics", *Chemical Society Reviews*, vol. 40, no. 6, pp. 3336–3355, 2011.

[115] S Pramanik, C.-G. Stefanita, S Patibandla, S Bandyopadhyay, K Garre, N Harth, and M Cahay, "Observation of extremely long spin relaxation times in an organic nanowire spin valve", *Nature nanotechnology*, vol. 2, no. 4, p. 216, 2007.

[116] P. Boross, B. Dóra, A. Kiss, and F. Simon, "A unified theory of spin-relaxation due to spin-orbit coupling in metals and semiconductors", *Scientific reports*, vol. 3, p. 3233, 2013.

[117] L. Ma, L. Lang, J. Kim, Z. Yuan, R. Wu, S. Zhou, and X. Qiu, "Spin diffusion length and spin Hall angle in $Pd_{1-x} Pt_x$/ YIG heterostructures: Examination of spin relaxation mechanism", *Physical Review B*, vol. 98, no. 22, p. 224 424, 2018.

[118] X. Xie, D. Li, T.-H. Tsai, J. Liu, P. V. Braun, and D. G. Cahill, "Thermal conductivity, heat capacity, and elastic constants of water-soluble polymers and polymer blends", *Macromolecules*, vol. 49, no. 3, pp. 972–978, 2016.

[119] M. M. Steeves, "Electronic transport properties of ruthenium and ruthenium dioxide thin films", PhD thesis, 2011.

[120] K. Behnia and H. Aubin, "Nernst effect in metals and superconductors: A review of concepts and experiments", *Reports on Progress in Physics*, vol. 79, no. 4, p. 046 502, 2016.

[121] K. Lee, S. Cho, S. H. Park, A. Heeger, C.-W. Lee, and S.-H. Lee, "Metallic transport in polyaniline", *Nature*, vol. 441, no. 7089, p. 65, 2006.

[122] O. Bubnova, Z. U. Khan, H. Wang, *et al.*, "Semi-metallic polymers", *Nature materials*, vol. 13, no. 2, p. 190, 2014.

[123] T. V. de Oliveira, "Polythiophene-based nanoscale lateral devices", PhD thesis, Universidad del País Vasco-Euskal Herriko Unibertsitatea, 2014.

[124] I. Lee, G. W. Kim, M. Yang, and T.-S. Kim, "Simultaneously enhancing the cohesion and electrical conductivity of PEDO:PSS conductive polymer films using dmso additives", *ACS applied materials & interfaces*, vol. 8, no. 1, pp. 302–310, 2015.

[125] N. Ikeda, T. Koganezawa, D. Kajiya, and K.-i. Saitow, "Performance of Si/PEDO:PSS hybrid solar cell controlled by PEDO:PSS film nanostructure", *The Journal of Physical Chemistry C*, vol. 120, no. 34, pp. 19 043–19 048, 2016.

[126] N. Massonnet, A. Carella, O. Jaudouin, P. Rannou, G. Laval, C. Celle, and J.-P. Simonato, "Improvement of the Seebeck coefficient of PEDO:PSS by chemical reduction combined with a novel method for its transfer using free-standing thin films", *Journal of Materials Chemistry C*, vol. 2, no. 7, pp. 1278–1283, 2014.

[127] A. M. Nardes, R. A. Janssen, and M. Kemerink, "A morphological model for the solvent-enhanced conductivity of PEDO:PSS thin films", *Advanced Functional Materials*, vol. 18, no. 6, pp. 865–871, 2008.

[128] Y. Kim, S. Chung, K. Cho, *et al.*, "Enhanced charge injection properties of organic field-effect transistor by molecular implantation doping", *Advanced Materials*, vol. 31, no. 10, p. 1 806 697, 2019.

[129] J.-C. Chiang and A. G. MacDiarmid, "Polyaniline: Protonic acid doping of the emeraldine form to the metallic regime", *Synthetic Metals*, vol. 13, no. 1-3, pp. 193–205, 1986.

[130] J. E. Cochran, M. J. Junk, A. M. Glaudell, *et al.*, "Molecular interactions and ordering in electrically doped polymers: Blends of PBTTT and F4TCNQ", *Macromolecules*, vol. 47, no. 19, pp. 6836–6846, 2014.

[131] S. Klingler, H. Maier-Flaig, C. Dubs, *et al.*, "Gilbert damping of magnetostatic modes in a Yttrium iron garnet sphere", *Applied Physics Letters*, vol. 110, no. 9, p. 092 409, 2017.

[132] C. Hauser, T. Richter, N. Homonnay, *et al.*, "Yttrium iron garnet thin films with very low damping obtained by recrystallization of amorphous material", *Scientific reports*, vol. 6, p. 20 827, 2016.

[133] H. Wang, C. Du, P. C. Hammel, and F. Yang, "Strain-tunable magnetocrystalline anisotropy in epitaxial $Y_3Fe_5O_{12}$ thin films", *Physical Review B*, vol. 89, no. 13, p. 134 404, 2014.

[134] H. B. Vasili, B. Casals, R. Cichelero, *et al.*, "Direct observation of multivalent states and 4 f-3 d charge transfer in Ce-doped Yttrium iron garnet thin films", *Physical Review B*, vol. 96, no. 1, p. 014 433, 2017.

[135] P Hansen, P Röschmann, and W Tolksdorf, "Saturation magnetization of gallium-substituted Yttrium iron garnet", *Journal of Applied Physics*, vol. 45, no. 6, pp. 2728–2732, 1974.

[136] H. Maier-Flaig, S. Klingler, C. Dubs, *et al.*, "Temperature-dependent magnetic damping of Yttrium iron garnet spheres", *Physical Review B*, vol. 95, no. 21, p. 214 423, 2017.

[137] B. Lax and K. J. Button, "Microwave ferrites and ferrimagnetics", 1962.

[138] A. Chumak, A. Serga, and B Hillebrands, "Magnonic crystals for data processing", *Journal of Physics D: Applied Physics*, vol. 50, no. 24, p. 244 001, 2017.

[139] S. D. Hoath, W.-K. Hsiao, G. D. Martin, *et al.*, "Oscillations of aqueous PEDO:PSS fluid droplets and the properties of complex fluids in drop-on-demand inkjet printing", *Journal of Non-Newtonian Fluid Mechanics*, vol. 223, pp. 28–36, 2015.

[140] D. M. Pozar, "Microwave engineering", *Wiley*, 2005.

[141] T. Richter, "Spinpumpen und inverser spin-Hall-effekt in granularen systemen", PhD thesis, 2018.

[142] I. S. Maksymov and M. Kostylev, "Broadband stripline ferromagnetic resonance spectroscopy of ferromagnetic films, multilayers and nanostructures", *Physica E: Low-dimensional Systems and Nanostructures*, vol. 69, pp. 253–293, 2015.

[143] P. Dutta and P. Horn, "Low-frequency fluctuations in solids: 1/f noise", *Reviews of Modern physics*, vol. 53, no. 3, p. 497, 1981.

[144] R. Sanders, D Paquette, V Jaccarino, and S. Rezende, "Radiation damping in magnetic resonance. ii. continuous-wave antiferromagnetic-resonance experiments", *Physical Review B*, vol. 10, no. 1, p. 132, 1974.

[145] G Wende, "Radiation damping in fmr measurements in a nonresonant rectangular waveguide", *physica status solidi (a)*, vol. 36, no. 2, pp. 557–567, 1976.

[146] M. A. Schoen, J. M. Shaw, H. T. Nembach, M. Weiler, and T. J. Silva, "Radiative damping in waveguide-based ferromagnetic resonance measured via analysis of perpendicular standing spin waves in sputtered permalloy films", *Physical Review B*, vol. 92, no. 18, p. 184 417, 2015.

[147] M. Bailleul, "Shielding of the electromagnetic field of a coplanar waveguide by a metal film: Implications for broadband ferromagnetic resonance measurements", *Applied Physics Letters*, vol. 103, no. 19, p. 192 405, 2013.

[148] M Kostylev, "Strong asymmetry of microwave absorption by bilayer conducting ferromagnetic films in the microstrip-line based broadband ferromagnetic resonance", *Journal of Applied Physics*, vol. 106, no. 4, p. 043 903, 2009.

[149] I. S. Maksymov and M. Kostylev, "Impact of conducting nonmagnetic layers on the magnetization dynamics in thin-film magnetic nanostructures", *Journal of Applied Physics*, vol. 113, no. 4, p. 043 927, 2013.

[150] H. Chang, P. Li, W. Zhang, T. Liu, A. Hoffmann, L. Deng, and M. Wu, "Nanometer-thick Yttrium iron garnet films with extremely low damping", *IEEE Magnetics Letters*, vol. 5, pp. 1–4, 2014.

[151] H. Chang, P. P. Janantha, J. Ding, *et al.*, "Role of damping in spin Seebeck effect in Yttrium iron garnet thin films", *Science advances*, vol. 3, no. 4, e1601614, 2017.

[152] M. A. Schoen, D. Thonig, M. L. Schneider, *et al.*, "Ultra-low magnetic damping of a metallic ferromagnet", *Nature Physics*, vol. 12, no. 9, p. 839, 2016.

[153] B Heinrich, C Burrowes, E Montoya, *et al.*, "Spin pumping at the magnetic insulator (YIG)/normal metal (Au) interfaces", *Physical review letters*, vol. 107, no. 6, p. 066 604, 2011.

[154] M. M. Steeves, "Electronic transport properties of ruthenium and ruthenium dioxide thin films", *PhD thesis*, 2011.

[155] Z.-G. Yu, "Spin Hall effect in disordered organic solids", *Physical review letters*, vol. 115, no. 2, p. 026 601, 2015.

[156] T Holstein, "Hall effect in impurity conduction", *Physical Review*, vol. 124, no. 5, p. 1329, 1961.

[157] H Böttger and V. Bryksin, "Hopping conductivity in ordered and disordered solids (I)", *physica status solidi (b)*, vol. 78, no. 1, pp. 9–56, 1976.

[158] H Böttger and V Bryksin, "Hopping conductivity in ordered and disordered solids (II)", *physica status solidi (b)*, vol. 78, no. 2, pp. 415–451, 1976.

[159] L Friedman, "I. the Hall effect in ordered and disordered systems", *Philosophical Magazine B*, vol. 38, no. 5, pp. 467–476, 1978.

[160] P. Butcher and A. Kumar, "The Hall mobility of carriers hopping in an impurity band", *Philosophical Magazine B*, vol. 42, no. 2, pp. 201–212, 1980.

[161] L Friedman and M Pollak, "The Hall effect in the variable-range-hopping regime", *Philosophical Magazine B*, vol. 44, no. 4, pp. 487–507, 1981.

[162] P. Butcher and J. Mcinnes, "The Hall mobility of carriers hopping in an impurity band: II. numerical results and analysis for the r-percolation model", *Philosophical Magazine B*, vol. 44, no. 5, pp. 595–601, 1981.

[163] H Böttger and V. Bryksin, "Hopping conductivity in ordered and disordered systems (III)", *physica status solidi (b)*, vol. 113, no. 1, pp. 9–49, 1982.

[164] P. Butcher, J. Mcinnes, and S Summerfield, "The Hall mobility of carriers hopping in an impurity band", *Philosophical Magazine B*, vol. 48, no. 6, pp. 551–560, 1983.

[165] X.-J. Liu, X. Liu, and J. Sinova, "Scaling of the anomalous Hall effect in the insulating regime", *Physical Review B*, vol. 84, no. 16, p. 165 304, 2011.

[166] J. Sinova, S. O. Valenzuela, J Wunderlich, C. Back, and T Jungwirth, "Spin Hall effects", *Reviews of Modern Physics*, vol. 87, no. 4, p. 1213, 2015.

[167] R. Po, C. Carbonera, A. Bernardi, F. Tinti, and N. Camaioni, "Polymer-and carbon-based electrodes for polymer solar cells: Toward low-cost, continuous fabrication over large area", *Solar Energy Materials and Solar Cells*, vol. 100, pp. 97–114, 2012.

[168]   I. McCulloch, M. Heeney, C. Bailey, *et al.*, "Liquid-crystalline semiconducting polymers with high charge-carrier mobility", *Nature materials*, vol. 5, no. 4, p. 328, 2006.

[169]   T. Schuettfort, B. Watts, L. Thomsen, M. Lee, H. Sirringhaus, and C. R. McNeill, "Microstructure of polycrystalline PBTTT films: Domain mapping and structure formation", *ACS nano*, vol. 6, no. 2, pp. 1849–1864, 2012.

[170]   R. Fujimoto, Y. Yamashita, S. Kumagai, *et al.*, "Molecular doping in organic semiconductors: Fully solution-processed, vacuum-free doping with metal–organic complexes in an orthogonal solvent", *Journal of Materials Chemistry C*, vol. 5, no. 46, pp. 12 023–12 030, 2017.

[171]   H.-Y. Chen, G. Schweicher, M. Planells, *et al.*, "Crystal engineering of dibenzothiophenothieno [3, 2-b] thiophene (DBTTT) isomers for organic field-effect transistors", *Chemistry of Materials*, vol. 30, no. 21, pp. 7587–7592, 2018.

[172]   S. Jiang, S Liu, P Wang, Z. Luan, X. Tao, H. Ding, and D Wu, "Exchange-dominated pure spin current transport in Alq3 molecules", *Physical review letters*, vol. 115, no. 8, p. 086 601, 2015.

[173]   Y.-T. Chen, S. Takahashi, H. Nakayama, M. Althammer, S. T. Goennenwein, E. Saitoh, and G. E. Bauer, "Theory of spin Hall magnetoresistance", *Physical Review B*, vol. 87, no. 14, p. 144 411, 2013.

[174]   S. Marmion, M Ali, M McLaren, D. Williams, and B. Hickey, "Temperature dependence of spin Hall magnetoresistance in thin YIG/Pt films", *Physical Review B*, vol. 89, no. 22, p. 220 404, 2014.

[175]   F. Czeschka, L Dreher, M. Brandt, *et al.*, "Scaling behavior of the spin pumping effect in ferromagnet-platinum bilayers", *Physical review letters*, vol. 107, no. 4, p. 046 601, 2011.

[176]   S. Meyer, M. Althammer, S. Geprägs, M. Opel, R. Gross, and S. T. Goennenwein, "Temperature dependent spin transport properties of platinum inferred from spin Hall magnetoresistance measurements", *Applied Physics Letters*, vol. 104, no. 24, p. 242 411, 2014.

[177]   I. Boventer, M. Pfirrmann, J. Krause, Y. Schön, M. Kläui, and M. Weides, "Complex temperature dependence of coupling and dissipation of cavity magnon polaritons from millikelvin to room temperature", *Physical Review B*, vol. 97, no. 18, p. 184 420, 2018.

[178]   S. R. Marmion, "Comparison of spin Hall magnetoresistance temperature dependence in YIG/metal systems", PhD thesis, University of Leeds, 2016.

[179]   P. Bobbert, W Wagemans, F. Van Oost, B Koopmans, and M Wohlgenannt, "Theory for spin diffusion in disordered organic semiconductors", *Physical review letters*, vol. 102, no. 15, p. 156 604, 2009.

[180]   C. Du, H. Wang, F. Yang, and P. C. Hammel, "Enhancement of pure spin currents in spin pumping $Y_3Fe_5O_{12}$/Cu/metal trilayers through spin conductance matching", *Physical Review Applied*, vol. 1, no. 4, p. 044 004, 2014.

[181]   B. I. Shklovskii and A. L. Efros, *Electronic properties of doped semiconductors*. Springer Science & Business Media, 2013, vol. 45.

[182]   I. Hughes and T. Hase, *Measurements and their uncertainties: a practical guide to modern error analysis*. Oxford University Press, 2010.

[183]   N. J. Harmon and M. E. Flatté, "Spin relaxation in materials lacking coherent charge transport", *Physical Review B*, vol. 90, no. 11, p. 115 203, 2014.

[184]   N. Harmon and M. Flatté, "Distinguishing spin relaxation mechanisms in organic semiconductors", *Physical review letters*, vol. 110, no. 17, p. 176 602, 2013.

[185]   L. Schulz, M Willis, L Nuccio, *et al.*, "Importance of intramolecular electron spin relaxation in small molecule semiconductors", *Physical Review B*, vol. 84, no. 8, p. 085 209, 2011.

Acknowledgement

After years of working in a wonderful scientific atmosphere with an amazing group, it is time to express my gratitude to every one I owe for accomplishing this work.

First of all, I would like to express my deepest appreciation and sincere thanks to Prof. Dr. Georg Schmidt for giving me the opportunity to conduct my research in the "Nanostructured Materials" group as a Ph.D. student. I am really grateful for many things he gave, great guidance, fruitful discussions I always enjoyed, and also teaching us the way of scientific and creative thinking. I am also grateful to him for continuous support and encouragement during the past years of working in this group.

I would like to thank the entire team of Interdisciplinary Center for Materials Science, for their extensive help and cooperation during the preparation, deposition, and characterization of samples in the clean room:-

Dr. Bodo Fuhrmann for giving the introduction of clean room and many devices inside the clean room. Dr. Frank Heyroth and Mr. Sven Schlenker for continuous help and support.

I would like to express my sincere thanks to Prof. Dr. Henning Sirringhaus and Olga Zadvorna from Cavendish Laboratory in Cambridge for the great cooperation and fruitful meetings and discussions regarding the part of PBTTT which has yielded a nice work made a great addition to the thesis. Special thanks to Olga Zadvorna for doing the fabrication and characterization steps of the PBTTT samples. And also many thanks to here for giving me an introduction to some experiments and devices during my visit to Cambridge.

Many thanks to Prof. Dr. Jiro Sinova and Dr. Reza Mahani from Johannes Gutenberg- Universität in Mainz for the cooperation and fruitful discussions regarding the numerical calculations of ISHE in PEDOT:PSS. I am very grateful to the help and support I have got from everyone in the "Nanostructured Materials" group especially, Alexander Müller, Martin Wahler, Tim Richter, Christoph Hauser and Dr. Philipp Dürrenfeld. Many thanks to Dr. Christian Eisenschmidt for providing me with the Squid measurements, to Camillo Ballani for doing the AFM, to Olga Wid for providing the LI-thermography measurements, and to Stephanie Lake for reading this thesis. Many thanks to Dr. Makarem Hussein for his unlimited and priceless support which helped me to overcome many difficulties and obstacles I faced on my way, thanks a lot. I would like to express my deepest gratitude and thanks to my parents for their support and unlimited love in my entire life. Many thanks to my brother Abdulfattah for his continuous support and being always there in hard times.

I would like to express my love and thanks to my wife and my kids for their support, and also their patience on my absence from home most of the time because of the work. Many thanks to many friends who have been always like a family and with them I never felt far from home. I am also grateful for the continuous support I always got from Taiz University in Yemen.

And finally, for the doctoral scholarship, I would like to express my sincere thanks to the "Deutscher Akademischer Austauschdienst" - (DAAD).

Publications

Publications relevant to this work

Journals (peer-reviewed)

1. **Mohammad M. Qaid**, O. Zadvorna, H. Sirringhaus, and G. Schmidt, "ISHE detection and spin relaxation mechanism in highly doped semiconducting polymer PBTTT", *Under preparation.*

2. **Mohammad M. Qaid**, R. Mahani, J. Sinova, and G. Schmidt, "Quantifying the Inverse spin-Hall effect in highly doped PEDOT:PSS", Phys. Rev. Research 2, 013207 (2020).

3. **Mohammad M. Qaid**, Tim Richter, Alexander Müller, Christoph Hauser, Camillo Ballani, and Georg Schmidt, "Radiation damping in ferromagnetic resonance induced by a conducting spin sink", Phys. Rev. B 96, 184405 (2017).

4. Christoph Hauser, Tim Richter, Nico Homonnay, Christian Eisenschmidt, **Mohammad Qaid**, Hakan Deniz, Dietrich Hesse, Maciej Sawicki, Stefan G. Ebbinghaus, and Georg Schmidt, "Yttrium iron garnet thin films with very low damping obtained by recrystallization of amorphous material." , Scientific reports 6, 20827 (2016).

Conference Talks

1. **Mohammad M. Qaid**, Georg Schmidt, "What is true and what is false: The magnitude of the inverse spin-Hall effect in PEDOT:PSS", 9th Joint European Magnetic Symposia Conference (JEMS), Mainz, Germany, (2018).

2. **Mohammad M. Qaid**, Olga Zadvorna, Henning Sirringhaus, Georg Schmidt, "Spin-charge conversion in π-conjugated polymer PBTTT", Sixth International Meeting on Spins in Semiconductors (SPINOS VII), Halle (Saale), Germany (2018).

3. **Mohammad Qaid**, Tim Richter, Alexander Müller, and Georg Schmidt,"Spin Pumping and Inverse Spin-Hall Effect in PEDOT:PSS", DPG, Dresden, Germany (2017).

4. **Mohammad Qaid**, Tim Richter, Christoph Hauser, Georg Schmidt, "Spin pumping into high conductivity polymers", DPG, Regensburg, Germany (2016).

Curriculum vitae

First Name	Mohammad M. Qaid
Family Name	Mohammad
Date of Birth	30.05.1982
Place of Birth	Taiz - Yemen
Nationality	Yemeni
E-mail	abuaymenmh@gmail.com
Marital status	Married

Education

2008 - 2012	Master of Science in Physics
	King Saud University - Saudi Arabia
Thesis topic	Fabrication and Characterization of Supercapacitors with
	Carbon Nanostructured Films as a Bottom Electrode
2011 - 2013	International scholar
	Interuniversity of microelectronic center (IMEC), Leuven - Belgium
	Group: Nano Confined Applics Interfaces and Surfaces group- Energy storage.
2013- 2014	Assistant Lecturer
	Taiz University - Yemen
2015 - to date	PhD in Institut für Physik
	Nanostrukturierte Materialien
	Martin-Luther-Universität Halle-Wittenberg
	(Supervised by Prof. Dr. G. Schmidt)

Eidesstattliche Erklärung

Hiermit erkläre ich an Eides statt, dass ich die Arbeit selbständig und ohne fremde Hilfe verfasst, keine anderen als die von mir angegebenen Quellen und Hilfsmittel benutzt und die den benutzten Werken wörtlich oder inhaltlich entnommenen Stellen als solche kenntlich gemacht habe.

Weiterhin erkläre ich, dass ich bisher keine vergeblichen Promotionsversuche unternommen habe. Diese Dissertation hat in ihrer gegenwärtigen bzw. in einer anderen Fassung bisher keiner anderen Fakultät vorgelegen.

Halle (Saale), November 2019

_____

Mohammad M. Qaid Mohammad